

ADVANCED PHOTORESIST TECHNOLOGIES BY INTRICATE MOLECULAR  
BRUSH ARCHITECTURES

A Dissertation

by

SANGHO CHO

Submitted to the Office of Graduate and Professional Studies of  
Texas A&M University  
in partial fulfillment of the requirements for the degree of

DOCTOR OF PHILOSOPHY

Chair of Committee,	Karen L. Wooley
Committee Members,	Donald J. Darensbourg
	James D. Batteas
	Perla B. Balbuena
Head of Department,	François P. Gabbaï

August 2015

Major Subject: Chemistry

Copyright 2015 Sangho Cho

## ABSTRACT

With recent technological improvements, fabrication of integrated circuit elements on shrinking scales is required to meet the demand for massive storage and fast data processing. As the fabrication of high resolution patterns requires short wavelength radiation sources, extreme ultraviolet and electron beam techniques have been developed as radiation sources for next-generation lithography. Advancements of lithography techniques accompany the evolution of resist materials for the synchronous fulfillment of high sensitivity, high resolution, and high structural integrity. Our strategy for nanofabrication is a combination of bottom-up synthesis and top-down lithography. The use of cylindrical brush polymers, which can vertically align on substrates, affords access to electron-beam-generated patterns with the minimum pixel size determined by the cylinder diameter.

Cylindrical brush polymers for negative- and positive-tone photoresist materials were synthesized by controlled radical and olefin metathesis polymerization. Macromonomers with well-defined size variations were prepared by reversible addition-fragmentation chain transfer polymerization of monomers having surface energy reducing, substrate adhesion enhancing, and lithographically functioning moieties. Then, sequential ring-opening metathesis polymerization of the macromonomers *via* a “grafting-through” strategy allows precise control of concentric and lengthwise dimensions and compositions in the brush polymer structures.

The brush polymers consist of a rigid polymeric backbone with covalently tethered side chains which allow facile access to a cylindrical morphology due to their steric repulsion. Low surface energy of fluoropolymers at one end and the high polarity of groups at the other end drive the cylindrical brush polymers to vertically align on the polar silicon wafer substrate as characterized by surface analysis techniques. The stretched conformation of the brush polymers facilitates their assembly by reducing chain entanglement.

The chemically amplified resists from the brush polymers exhibit high lithographic performance with a few tens of nanometer resolution. The brush polymers with poly(*p*-hydroxystyrene)s yielded negative-tone features by crosslinking chemistry, while those having acid-labile tertiary esters gave positive-tone features. Cylindrical brush polymer based resists showed their superior lithographic performance over linear block copolymer precursors in both resolution and sensitivity by having each vertically aligned molecule act as a molecular pixel. As a result, the tuning of composition and dimension using bottom-up synthetic strategy allows the fine tuning of top-down lithographic performance.

## DEDICATION

To my family

## ACKNOWLEDGEMENTS

I would like to express my gratitude to my advisor, Dr. Karen L. Wooley, for her guidance, support and patient during my graduate study at Texas A&M University. Without her tremendous support, this work would not be possible. I also thank my committee members, Dr. Donald J. Darensbourg, Dr. James D. Batteas, Dr. Perla B. Balbuena, and Dr. Nicole Zacharia for their guidance.

I would like to thank my collaborator, Dr. Peter Trefonas, Dr. James W. Thackeray, Dr. Liam Spencer, Dr. Phillip D. Hustad, and Dr. Mingqi Li from Dow Electronic Materials for their helpful discussion with the research plans and Dr. Emile A. Scheweikert, Dr. Stanislav V. Verkhoturov, Dr. Micheal J. Eller, and Mr. Fan Yang for their efforts in analysis of polymer surface with secondary ion mass spectrometer during the collaborative projects.

I would like to acknowledge my past and present Wooley group members, Dr. Guorong Sun, Dr. Jeffery Raymond, Dr. Ang Li, Ms. Corrie Clark, Dr. Yannick Borguet, Dr. Ashlee Jahneke, Mr. Xun He, Mr. Eric Leonhardt, Mrs. Adriana Pavia-Sanders, Mr. Gyu Seong Heo, Mr. Fuwu Zhang, Dr. Amandine Noel, Dr. Jiong Zou and Dr. Mahmoud Elsabahy for their contributions to this work through either direct collaboration or helpful discussion. It's a privilege of mine to work with these excellent individuals and benefit from their expertise. I express my gratitude to all Wooley group members, Dr. Soon-Mi Lim, Dr. Marco Giles, Dr. Lu Su, Mr. Jungwei Fan, Ms. Simcha Felder, Ms. Jeniree Flores, Mr. Chris Komatsu, Ms. Samantha Kristufek, Mr. Richen Li, Mr. Young Lim, Ms. Lauren Link, Mr. Alexander Lonnecker, Ms. Kellie Seetho, Ms. Jennifer Summerhill, Mr. Timothy Tsao, Mr. Kevin Waker, Mr. Peter Wang, Ms. Amelia Gonzalez, Mr. Joel Russell, Ms. Sarah Ward, Dr. Tiffany

Gustafson, Dr. Koichiro Mikami, Dr. Kevin Pollack, Dr. Sandani Samarajeewa, Dr. Shiyi Zhang, Dr. Philip M. Imbesi, Dr. Nam S. Lee, Ms. Judy Taylor, Ms. Casey MacDonald and Mr. Andy Moutray, who have created an enjoyable laboratory environment.

I acknowledge Dow Chemical Company (collaborative research agreement), the National Science Foundation (DMR-1105304), and the Welch Foundation (W. T. Doherty-Welch Chair, A-0001) for financial support.

Finally, I would like to pay special thanks to my family for their love and support.

## NOMENCLATURE

AFM	Atomic force microscopy
AIBN	2,2'-Azobis(2-methylpropionitrile)
BC	Brush control
BCL	Block copolymer lithography
BCP	Block copolymer
BTFHMBMA	1,1,1-Trifluoro-2-(trifluoromethyl)-2-hydroxy-4-methyl-5-pentyl methacrylate
CAR	Chemically amplified resist
CB	Control brush
CH <sub>2</sub> Cl <sub>2</sub>	Dichloromethane
CRP	Controlled radical polymerization
CTA	Chain-transfer agent
DBT	Diblock brush terpolymer
DSA	Directed self-assembly
EBL	Electron beam lithography
ECPMA	1-Ethylcyclopentyl methacrylate
EUV	Extreme ultraviolet
EVE	Ethyl vinyl ether
GBLMA	$\gamma$ -Butyrolacton-2-yl methacrylate
GPC	Gel-permeation chromatography

HMMM	<i>N,N,N',N',N'',N''</i> -hexakis(methoxymethyl)-1,3,5-triazine-2,4,6-triamine
LC	Linear control
LER	Line-edge roughness
LMIS	Liquid metal ion source
MW	Molecular weight
NMR	Nuclear magnetic resonance
OWRK	Owens-Wendt-Rabel-Kaelble
P( <i>p</i> HS- <i>co</i> -PhMI)	Poly( <i>p</i> -hydroxy styrene- <i>co</i> - <i>N</i> -phenyl maleimide)
PAB	Post-apply baking
PAG	Photoacid generator
PBTFHMBMA	Poly(1,1,1-trifluoro-2-(trifluoromethyl)-2-hydroxy-4-methyl-5-pentyl methacrylate)
PDI	Polydispersity index
PEB	Post-exposure baking
PhMI	<i>N</i> -phenyl maleimide
<i>p</i> HS	4-hydroxystyrene
PNB	Polynorbornene
PTFEMA	Poly(2,2,2-trifluoroethyl methacrylate)
PTF <i>p</i> HS	Poly(tetrafluoro <i>p</i> -hydroxystyrene)
RAFT	Reversible addition-fragmentation chain transfer
RMS	Root-mean-square



ROMP	Ring-opening metathesis polymerization
SAA	Solvent-assisted annealing
SEM	Scanning electron microscope
SIMS	Secondary-ion mass spectrometry
$T_d$	Decomposition temperature
TFEMA	2,2,2-Trifluoroethyl methacrylate
TFpHS	2,3,5,6-Tetrafluoro-4-hydroxystyrene
$T_g$	Glass transition temperature
TGA	Thermogravimetric analysis
THF	Tetrahydrofuran
TMAH	Tetramethylammonium hydroxide
TOF	Time-of-flight
UV	Ultraviolet
XPS	X-ray photoelectron spectroscopy

## TABLE OF CONTENTS

	Page
ABSTRACT.....	ii
DEDICATION.....	iv
ACKNOWLEDGEMENTS.....	v
NOMENCLATURE.....	vii
TABLE OF CONTENTS.....	x
LIST OF FIGURES.....	xii
LIST OF SCHEMES.....	xvi
LIST OF TABLES.....	xvii
CHAPTER I INTRODUCTION.....	1
1.1 Photolithography and Electron Beam Lithography.....	1
1.2 Block Copolymer Lithography.....	3
1.3 Block Copolymer Lithography with Brush Polymer.....	7
1.4 Scope of the Thesis.....	9
CHAPTER II NANOSCOPIC CYLINDRICAL DUAL CONCENTRIC AND LENGTHWISE BLOCK BRUSH TERPOLYMERS AS COVALENT PRE-ASSEMBLED HIGH RESOLUTION AND HIGH SENSITIVITY NEGATIVE-TONE PHOTORESIST MATERIALS.....	12
2.1 Introduction.....	12
2.2 Results and Discussion.....	15
2.3 Experimental Section.....	36
2.4 Conclusion.....	50
CHAPTER III DIRECTING SELF-ASSEMBLY OF NANOSCOPIC CYLINDRICAL DIBLOCK BRUSH TERPOLYMERS INTO FILMS WITH DESIRED SPATIAL ORIENTATIONS: EXPANSION OF CHEMICAL COMPOSITION SCOPE.....	51

3.1 Introduction.....	51
3.2 Results and Discussion.....	54
3.3 Experimental Section.....	67
3.4 Conclusion.....	77
CHAPTER IV ADVANCED PHOTORESIST TECHNOLOGIES BY INTRICATE MOLECULAR BRUSH ARCHITECTURES: DIBLOCK BRUSH TERPOLYMER-BASED POSITIVE-TONE PHOTORESIST MATERIALS.....	79
4.1 Introduction.....	79
4.2 Results and Discussion.....	82
4.3 Experimental Section.....	98
4.4 Conclusion.....	107
CHAPTER V CONCLUSIONS.....	108
REFERENCES.....	111
APPENDIX A.....	124
APPENDIX B.....	129

## LIST OF FIGURES

	Page
Figure 1.1. Schematic representation of a generalized chemically amplified resist process.....	3
Figure 1.2. Phase diagram for coil-coil diblock copolymers in the bulk as a function of the volume fraction of one of the blocks ( $f_A$ ). Reprinted with permission from ref 20. Copyright 2010 Elsevier Ltd....	5
Figure 1.3. Synthetic strategies to prepare bottle brush polymers.....	7
Figure 1.4. Cylindrical diblock brush polymers for lithographic usage with their dimensional and compositional variation.....	10
Figure 2.1. (a) Schematic representation of the targeted dimensions for the diblock brush terpolymers (left), their ideal alignment after deposition as a monolayer thin film (center), and comparison with linear block copolymer thin films that require multi-molecular supramolecular assembly with morphological directionality (right). (b) Schematic diagram of the overall strategy.....	14
Figure 2.2. The GPC profiles (a) and $^1\text{H}$ NMR (500 MHz, $\text{DMSO}-d_6$ ) spectra (b, c) for the NB-PTF $p$ HS macromonomers prepared from RAFT homopolymerizations of TFP $p$ HS. The spectrum in (b) was from macromonomer <b>1</b> and the spectrum in (c) was from macromonomer <b>2</b> ..	19
Figure 2.3. The normalized GPC profiles of the RAFT homopolymerizations of $p$ HS; entries are from Table 2.1.....	20
Figure 2.4. The GPC profiles (a) and $^1\text{H}$ NMR (500 MHz, $\text{DMSO}-d_6$ ) spectra (b, c) for the NB-P( $p$ HS- <i>co</i> -PhMI) macromonomers prepared from RAFT copolymerizations of $p$ HS and PhMI. The spectrum in (b) was from macromonomer <b>3</b> and the spectrum in (c) was from macromonomer <b>4</b> .....	21
Figure 2.5. Preparation and characterizations of <b>LC</b> [NB-PTF $p$ HS $_{12}$ - <i>b</i> -P( $p$ HS $_{48}$ - <i>co</i> -PhMI $_{48}$ )]. (a) Schematic illustration of the synthesis. (b) GPC profiles of the macro-CTA (NB-PTF $p$ HS $_{12}$ , blue) and <b>LC</b> (red). (c) $^1\text{H}$ NMR (500 MHz, acetone- $d_6$ ) spectrum of the NB-PTF $p$ HS $_{12}$ - <i>b</i> -P( $p$ HS $_{48}$ - <i>co</i> -PhMI $_{48}$ ).....	22

Figure 2.6.	(a, b) The normalized GPC profile of the sequential ROMP for preparation of Brush <b>I</b> (a) and <b>II</b> (b), respectively. (c) $^1\text{H}$ NMR (500 MHz, $\text{DMSO}-d_6$ ) spectra for the Brush <b>I</b> (left) and Brush <b>II</b> (right), respectively.....	24
Figure 2.7.	Tapping-mode AFM height (top) and phase (bottom) images of thin films without acetone annealing obtained from $5 \times 5 \mu\text{m}$ area. Film from <b>linear control</b> . (b) Film from brush <b>I</b> . (c) Film from brush <b>II</b> . Scale bar (black): 500 nm. The inserted image in (a) was the representative part of the linear control film phase imaging obtained from $2 \times 2 \mu\text{m}$ area (white scale bar: 250 nm).....	25
Figure 2.8.	SIMS fluorine depth profile of film prepared from spin-casting brush <b>II</b> on silicon wafer. <i>Sputtering rates</i> : film of 80 wt% Pt/20 wt% Pd alloy: 0.15 nm/s (sputtering yield: 15 atoms/projectile); Si wafer: 0.042 nm/s (sputtering yield: 3.37 atoms/projectile). The depth scale of the organic film corresponds to the thickness of film ( $\sim 30$ nm) measured by AFM.....	27
Figure 2.9.	XPS survey spectra of thin films prepared from brush <b>I</b> (red profile), brush <b>II</b> (blue profile), and <b>linear control</b> (black profile) on silicon wafer.....	27
Figure 2.10.	Representative $\text{C}_{60}$ SIMS spectra of brushes at $m/z = 0-50$ range (a) and $m/z = 100-200$ range (b), respectively.....	28
Figure 2.11.	SIMS fluorine depth profile of film prepared from spin-casting of brush <b>II</b> on silicon wafer and annealed 20 h under acetone atmosphere. <i>Sputtering rates</i> : film of 80wt% Pt/20wt% Pd alloy: 0.15 nm/s (sputtering yield: 15 atoms/projectile); Si wafer: 0.042 nm/s (sputtering yield: 3.37 atoms/projectile). The depth scale of the organic film corresponds to the thickness of this film ( $\sim 30$ nm) measured by AFM.....	30
Figure 2.12.	Tapping mode AFM height images of patterns generated by PEB-EBL. (a, b) <b>CAR-I</b> and (c, d) <b>CAR-II</b> at 250 and 400 $\mu\text{C}/\text{cm}^2$ exposure dosage, respectively. Scale bars: 500 nm.....	32
Figure 2.13.	Tapping mode AFM height images of patterns generated by PEB-EBL of <b>CAR-LC</b> at 250 $\mu\text{C}/\text{cm}^2$ (a) and 400 $\mu\text{C}/\text{cm}^2$ (b) exposure dosage, respectively. Scale bar: 500 nm.....	33

Figure 2.14.	Evaluations of the line height (a and c) and width (b and d) of the latent lines AFM, respectively, which were generated by PEB-EBL of <b>CAR-I</b> and <b>CAR-II</b> at 250 and 400 $\mu\text{C}/\text{cm}^2$ exposure dosage and $\text{TMAH}_{(\text{aq.})}$ development. The height and width were measured by tapping-mode AFM. The line width was measured at 75% of the line height and deducted $2 \times \text{AFM tip diameter}$ (10 nm).....	34
Figure 2.15.	(a) Synthesis of <b>BC</b> . (b) Tapping mode AFM height images of patterns generated by PEB-EBL of <b>CAR-BC</b> at 250 $\mu\text{C}/\text{cm}^2$ dosage (a) and 400 $\mu\text{C}/\text{cm}^2$ exposure dosage (b).....	35
Figure 2.16.	Tapping mode AFM height images of patterns generated by “direct”-EBL of <b>CAR-I</b> at 400 $\mu\text{C}/\text{cm}^2$ (a) and 600 $\mu\text{C}/\text{cm}^2$ (b) exposure dosage, respectively. Scale bar: 500 nm.....	36
Figure 3.1.	(a) The $^1\text{H}$ NMR spectra for <b>M3</b> (500 MHz, $\text{CD}_2\text{Cl}_2$ ) and brush <b>A/B</b> (500 MHz, $\text{DMSO}-d_6$ ). (b) The $^1\text{H}$ NMR spectra for <b>M4/5</b> (500 MHz, $\text{DMSO}-d_6$ ) and brush <b>C/D</b> (500 MHz, $\text{DMSO}-d_6$ ). The blue profiles were from macromonomers and the red profiles were from brushes.....	56
Figure 3.2.	(a, b) The GPC profile of the ROMP for <b>M3</b> (a) and <b>M5</b> (b), respectively. (c-f) The GPC profile of the sequential ROMP for preparation of brush <b>A</b> (c), <b>B</b> (d), <b>C</b> (e), and <b>D</b> (f), respectively.....	58
Figure 3.3.	Tapping-mode AFM height images of as-spun thin films of brushes. (a) control brush <b>I</b> , (b) control brush <b>II</b> , (c) brush <b>A</b> , (d) brush <b>B</b> , (e) brush <b>C</b> , (f) brush <b>D</b> . Scale bars: 1 $\mu\text{m}$ .....	61
Figure 3.4.	Tapping-mode AFM phase images of as-spun thin films of brushes. (a) control brush <b>I</b> , (b) control brush <b>II</b> , (c) brush <b>A</b> , (d) brush <b>B</b> , (e) brush <b>C</b> , (f) brush <b>D</b> . Scale bars: 1 $\mu\text{m}$ .....	62
Figure 3.5.	Tapping-mode AFM height images of acetone-annealed thin films of brushes. (a) control brush <b>I</b> , (b) control brush <b>II</b> , (c) brush <b>A</b> , (d) brush <b>B</b> , (e) brush <b>C</b> , (f) brush <b>D</b> . Scale bars: 1 $\mu\text{m}$ .....	63
Figure 3.6.	Tapping-mode AFM phase images of acetone-annealed thin films of brushes. (a) control brush <b>I</b> , (b) control brush <b>II</b> , (c) brush <b>A</b> , (d) brush <b>B</b> , (e) brush <b>C</b> , (f) brush <b>D</b> . Scale bars: 1 $\mu\text{m}$ .....	64

Figure 4.1.	Schematic conceptualization of composition and preparation of <b>DBT</b> ; a positive-tone photoresist material; and lithographic process by using a monolayer thin film comprised of ideally vertically-aligned <b>DBTs</b> and physically-blended PAGs on a PS-primed silicon wafer.....	82
Figure 4.2.	(a, b) The $^1\text{H}$ NMR spectrum for <b>M1</b> (a, 500 MHz, $\text{CDCl}_3$ ) and <b>M2</b> (b, 500 MHz, $\text{CD}_2\text{Cl}_2$ ), respectively. (c, d) The GPC profile for <b>M1</b> (c) and <b>M2</b> (d), respectively.....	86
Figure 4.3.	Normalized GPC profiles of <b>M1</b> and <b>M2</b> (dashed lines), <b>M3</b> and <b>M4</b> (dotted lines), <b>DBT</b> and <b>CB</b> (solid lines).....	87
Figure 4.4.	(a, b) The $^1\text{H}$ NMR spectrum for <b>DBT</b> (a, 500 MHz, $\text{DMSO}-d_6$ ) and <b>CB</b> (b, 500 MHz, acetone- $d_6$ ), respectively. (c, d) The GPC profile for <b>DBT</b> (c) and <b>CB</b> (d), respectively.....	88
Figure 4.5.	Tapping-mode AFM height (left column) and phase (right column) images of as-cast <b>DBT</b> (A) and <b>CB</b> (B) films, respectively. Scale bars: 500 nm.....	90
Figure 4.6.	Tapping-mode AFM height (left column) and phase (right column) images of the acetone-annealed <b>CB</b> (a) and <b>DBT</b> (b) films, respectively. Scale bars: 500 nm.....	90
Figure 4.7.	$\text{C}_{60}$ SIMS spectrum of the as-cast <b>DBT</b> film.....	92
Figure 4.8.	(a) Percentage of the vertically aligned <b>DBTs</b> within the as-cast film (red bar), calculated based upon the relative surface F content measured from XPS vs. the theoretical F content. (b) Surface coverage by SIMS (pink bar), presented by the percentage of co-emitted F-containing ions from nanodomains of the as-cast <b>DBT</b> film.....	93
Figure 4.9.	Tapping-mode AFM images of latent 120/70 nm (a, b), 100/100 nm (c, d), and 60/100 nm (e, f) line/space patterns, respectively, generated from 70/120, 100/100, and 100/60 nm exposure line/space features PEB-EBL of <b>DBT CAR</b> at 50 (left column) and 60 (right column) $\mu\text{C}/\text{cm}^2$ exposure dosages. Scale bars: 200 nm.....	97

## LIST OF SCHEMES

	Page
Scheme 2.1. Synthesis of P(NB- <i>g</i> -PTF <i>p</i> HS)- <i>b</i> -P(NB- <i>g</i> -P( <i>p</i> HS- <i>co</i> -PhMI)) diblock brush terpolymers.....	16
Scheme 3.1. Syntheses of the diblock brush terpolymers.....	55
Scheme 4.1. Syntheses of <b>DBT</b> and <b>CB</b> .....	84



## LIST OF TABLES

	Page
Table 2.1. RAFT polymerizations of TF <i>p</i> HS and <i>p</i> HS; RAFT copolymerizations of <i>p</i> HS and PhMI.....	18
Table 2.2. Relative ratios of elements in polymer film surface from XPS measurements.....	29
Table 2.3. Summary of static contact angles and surface energies of polymer films.....	30
Table 3.1. Summary of the DBT thin film characterization data.....	60
Table 3.2. Relative ratios of elements in polymer films surface from XPS measurements.....	66
Table 3.3. Summary of static contact angles and surface free energies of polymer films.....	67
Table 4.1. Relative ratios of elements in polymer films surface from XPS measurements.....	94
Table 4.2. Summary of static contact angles and surface free energies of brush polymer films.....	94

# CHAPTER I

## INTRODUCTION

### **1.1. Photolithography and Electron Beam Lithography**

Since its invention in 1959, photolithography has served as an important tool for micro- and nanofabrication in the semiconductor industry and is used to transfer the pre-designed patterns on a mask to the underlying substrate. In photolithography, a light-sensitive material, known as a photoresist, is selectively exposed to ultraviolet (UV) light through a mask made of a transparent quartz substrate with arbitrary features in a metal film. The resist materials on the exposed area change their solubility by chemical reactions, and consequently patterned relief is generated by selective removal of the resist in the developing process.

As technology improves, the demand for massive storage and fast processing of data requires fabrication of more integrated circuit elements in a limited space, thus driving the need for nanofabrication technology. In general, the ultimate resolution of a pattern is governed by the wavelength of the radiation used to create it. Therefore, light with shorter wavelengths needs to be used as the radiation source in order to achieve patterning of higher resolution. Currently, extreme ultraviolet (EUV, 13.5 nm) seems to be the most appropriate candidate for next-generation lithography.<sup>1</sup> Alternatively, electrons replace photons as the radiation source and the technique is called electron beam lithography (EBL).<sup>2</sup> In EBL, a latent pattern is generated by scanning a high energy electron beam directly on electron sensitive polymer materials. Nanoscale features with a

routine resolution of 20 nm can be generated by EBL; however, generating dense line features smaller than 10 nm is limited due to the proximity effect.<sup>3,4</sup>

The advancement of lithography techniques is required to accompany the evolution of the resist materials used. Conventional photoresists, such as novolac-diazonaphthoquinone, used for photolithography are not suitable to be used in next-generation systems, such as EUV lithography and EBL as these photoresists have low sensitivity and high absorption in such short wavelength and high energy radiation.<sup>5</sup> A new class of radiation sensitive materials with high quantum yield and low absorption are classified as chemically amplified resists (CARs).<sup>6-8</sup> In these materials, a single chemical event causes a cascade of subsequent reactions leading to a change in solubility of the parent polymer matrix, which results in the high sensitivity of the resist. In general, a CAR is composed of a base polymer matrix, a photoacid generator (PAG) that generates a catalyst upon irradiation, and an active moiety differentiating the solubility of the base polymer in the exposed area from that in the unexposed area.

Resists are divided into negative- or positive-tone depending on whether the exposed or unexposed areas remain as the patterned relief (Figure 1.1). In negative-tone resists, the photochemical reaction renders the polymer matrix insoluble by crosslinking chemistry, leaving the exposed area as the patterned relief. For instance, epoxy materials are crosslinked by acid-catalyzed cationic polymerization.<sup>9</sup> Also, hydroxy functional polymers, e.g. poly(hydroxystyrene), react with crosslinking agents, e.g. melamine derivatives, to afford highly crosslinked networks through a condensation polymerization mechanism<sup>10,11</sup> or an electrophilic aromatic substitution mechanism.<sup>12</sup> On the other hand,

in positive-tone resists, the polymer matrix in the exposed area becomes soluble upon acid-catalyzed deprotection<sup>13</sup> or depolymerization<sup>14</sup> chemistry and is removed during the developing process.

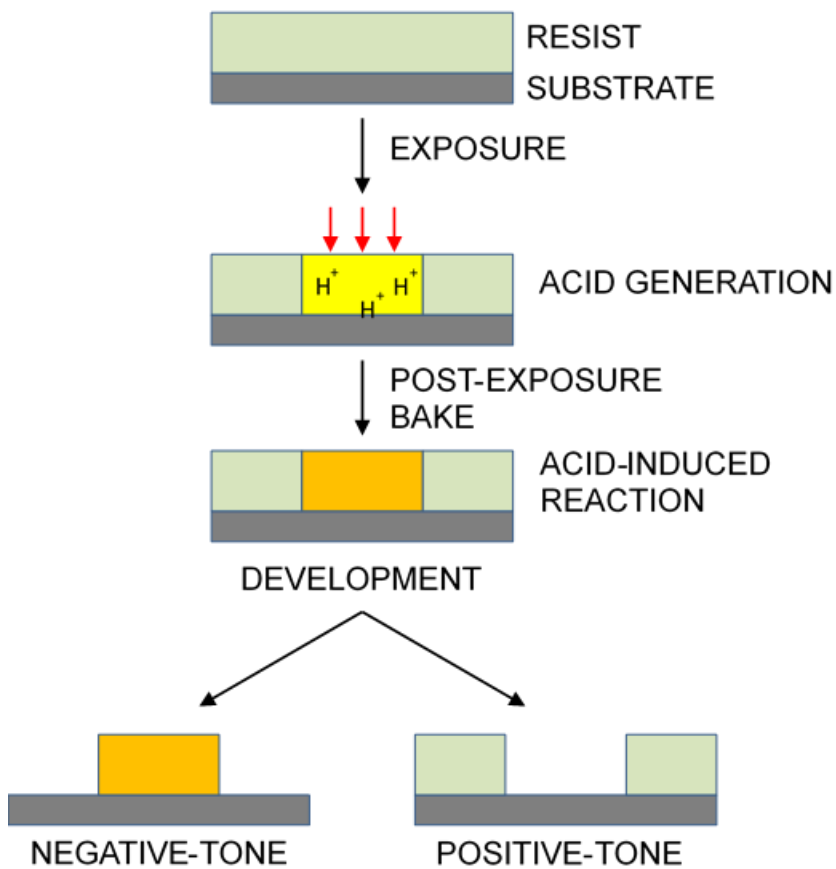


**Figure 1.1.** Schematic representation of a generalized chemically amplified resist process.

## 1.2. Block Copolymer Lithography

As an alternative technique for high throughput and low-cost nanofabrication, block copolymer lithography (BCL) has been developed to be used for lithographic masks

or as a template for nanostructure fabrication.<sup>15</sup> Block copolymers are composed of two or more chemically distinct homopolymers covalently linked to one another at their chain ends. In a mixture of homopolymers, the different chains tend to repulse each other and macroscopically phase segregate due to the low entropy of mixing. The covalent connectivity of the homopolymers in a block copolymer system, however, limits phase separation of the block copolymer to the scale of the polymer chain length, with typical domain dimensions of less than 100 nm. Upon heating, amorphous block copolymers self-assemble into thermodynamically stable structures containing nanoscopic domains. In general, the morphology of the nanodomains is determined by the volume fraction of each block, while the periodicity is determined by the molecular weight of the block copolymer.<sup>16</sup> Above the critical value of the strength of repulsive interaction,  $\chi N$  ( $\chi$  for the Flory-Huggins interaction parameter<sup>17-19</sup> and  $N$  for the overall degree of polymerization), for the order-disorder transition, the morphology varies from body-centered cubic spheres to hexagonally packed cylinders to bicontinuous gyroid to lamellae as the volume fraction of A,  $f_A$ , increases to 0.5 in simple coil-coil diblock copolymers (Figure 1.2).<sup>20,21</sup>

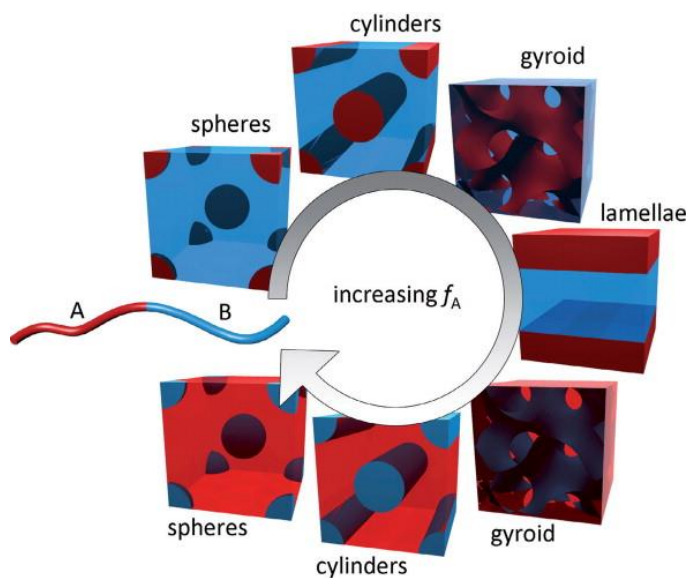


**Figure 1.2.** Phase diagram for coil-coil diblock copolymers in the bulk as a function of the volume fraction of one of the blocks ( $f_A$ ). Reprinted with permission from ref 20. Copyright 2010 Elsevier Ltd.

In addition to the segmental interaction between each block, the morphology in thin films of block copolymers is governed by the film thickness and the interfacial interaction at the air/polymer and polymer/substrate interfaces.<sup>21</sup> A low surface energy or a preferential interaction of one of the blocks leads to preferential wetting of one component to either air or the substrate. The interfacial interactions can be engineered in advance to tune the morphology of block copolymer thin films in order to obtain a high degree order. This technique is referred to as directed self-assembly (DSA).<sup>22-24</sup> In graphoepitaxial strategies, lithographically predefined posts or trenches topographically guide block copolymer self-assembly by providing additional interfacial interactions with them.<sup>24-26</sup> In chemoepitaxial strategies, a chemically modified substrate is used to enhance

the preferential affinity of one component to direct the alignment of the block copolymer domains.<sup>27-29</sup> The film thickness, especially the commensurability with the natural period of the block copolymer, is also an important factor for self-assembly of block copolymers in thin films. For example, block copolymers with a film thickness non-commensurable with their periodicity tend to orient normal to the substrate to minimize the energy of the copolymer.<sup>30,31</sup>

In BCL, annealing of a polymer film is a critical step for inducing long range order of the microdomains. Fast evaporation of the solvent during the deposition procedure, in general, leads to cast films of block copolymer solutions kinetically trapped in nonequilibrium and disorganized structures. In thermal annealing, heat above the glass transition temperature ( $T_g$ ) but below the decomposition temperature ( $T_d$ ) is applied to facilitate the formation of the equilibrium structure. However, thermal annealing is not effective for high molecular weight polymers and often requires long annealing times.<sup>32</sup> In solvent annealing,<sup>33</sup> cast films are exposed to solvent vapor causing swelling. The mobility of the polymer in the swollen state is enhanced leading to the thermodynamically favored arrangement. The parameters which affect the morphology of the final dried film include solvent selection,<sup>34-36</sup> either neutral or selective for one of the blocks, vapor pressure, exposure time,<sup>36,37</sup> and solvent evaporation rate.<sup>38,39</sup> The solvent compatibility with the polymer component affects the solvent uptake properties and the time required to reach the steady state where the chemical potential of the solvent has reached equilibrium both in the film and the vapor phase.<sup>40,41</sup> The gradient of solvent concentration and the rate of the change in solvent uptake or evaporation influence the propagation of local

ordering from the surface to the bottom of the polymer film resulting in the final morphological state.<sup>38</sup>

### 1.3. Block Copolymer Lithography with Brush Polymers

Brush polymers have been an emerging star in bottom-up nanomaterial fabrication due to their shape-persistent nature and outstanding spatial dimensions and available tunability.<sup>42</sup> Despite the need for periodic morphologies with large scale features (>100 nm) for optical devices such as photonic crystals or polarizers, the formation of well-defined structures of such large scale by the self-assembly of long linear block copolymers is limited due to the slow diffusion rate arising from their high chain entanglement.<sup>43</sup> Brush polymers are comprised of a polymeric backbones with densely grafted polymer bristles (Figure 1.3). The steric hindrance between the bristles forces the backbone to adopt a stretched conformation and reduces entanglement,<sup>44-46</sup> providing easy access to ordered nanostructures with large domain spacing despite their high molecular weight.<sup>47-</sup>

49

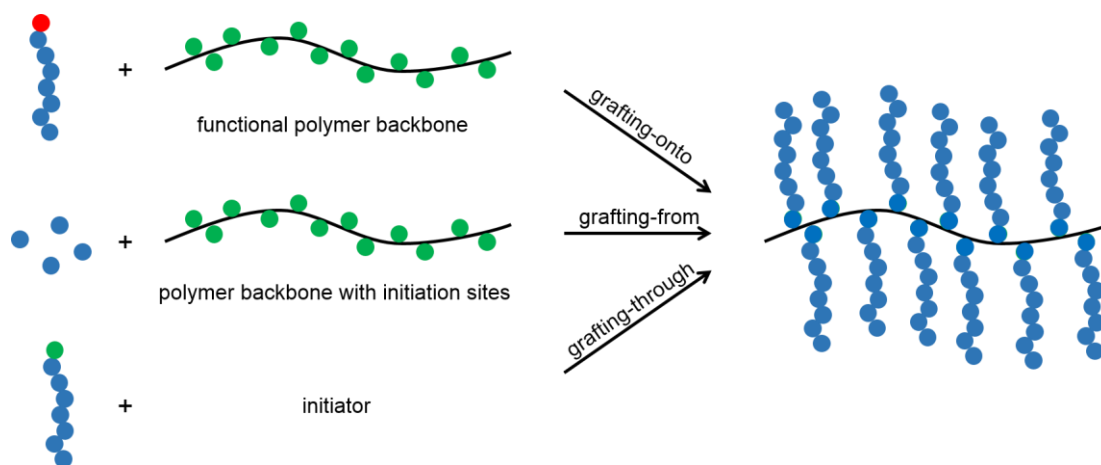


**Figure 1.3.** Synthetic strategies to prepare bottle brush polymers.



In the self-assembly process of brush polymers in melt or thin films, molecular architecture plays a significant role in the resulting morphologies. Symmetric brush polymers, having equal volume fraction of each block, self-assemble into lamellar structures with a domain spacing dictated by the backbone contour length for brush block copolymers<sup>50,51</sup> or the side chain length for brush random copolymers.<sup>51</sup> In general, highly asymmetric brush block copolymers do not tend to form well-ordered structures due to their reduced backbone flexibility and increased difficulty to adopt coiled conformations.<sup>51,52</sup> However, brush block copolymers with asymmetric side chain length self-assemble into a cylindrical morphology.<sup>53-55</sup> Even, multilayered structures can be assembled from random brush polymers having special end-groups on the side chains to give favorable interactions among them or with the substrate.<sup>56</sup>

Synthetic chemistry strategies allow for the preparation of molecular bottle brush polymers with a variety of architectures and chemical functionalities. Brush polymers can be constructed by three different synthetic strategies: grafting-onto, grafting-from, and grafting-through (Figure 1.3). In the “grafting-onto” strategy, an independently prepared backbone is functionalized with previously prepared polymer side chains through highly efficient click chemistry or nucleophilic substitution.<sup>57-59</sup> However, the coupling efficiency is limited with the increase of side chain density due to the steric hindrance. In the “grafting-from” strategy, monomers grow from a polyinitiator-backbone to form brush side chains through controlled radical or ring-opening polymerization.<sup>54,60,61</sup> Orthogonal polymerization or multistep processes are required to prepare backbone diblock brush polymers. In the “grafting-through” strategy, macromonomers, which will become the

side chains of the brush, are polymerized through the terminal functionalities to give the brush structure. In particular, the development of highly active ruthenium catalysts has enabled the synthesis of brush polymers with precise control of dimensions, side chain functionalities, and block sequence by ring-opening metathesis polymerization (ROMP) of norbornene-functionalized macromonomers.<sup>62-64</sup>

#### **1.4. Scope of the Thesis**

This dissertation is focused on the fundamental studies on the development of cylindrical bottle brush polymers that can vertically align on substrates, for use as high sensitivity photoresist materials. The brush architecture was selected for the facile access to cylindrical molecular structure which can serve as a pixel unit in lithographic patterns. The brush polymers, as shown in Figure 1.4, are prepared through a “grafting-through” strategy with precise control of dimensions and composition by reversible addition-fragmentation chain transfer (RAFT) polymerization and ROMP. First, the concentric and lengthwise dimensions of the cylindrical brushes are conveniently controlled by the variation of the absolute and relative lengths of the side chains versus the backbone. The sequential ROMP of pre-synthesized macromonomers with different chemical functionalities allows control of the composition within different regions of the cylindrical framework. The brush polymers are composed of three different structural and functional components: 1) the polynorbornene backbone supports the stretched conformation due to the steric hindrance of the dense side chains, which allows facile access to cylindrical nanoscopic objects; 2) the fluoropolymer side chains at one of the block act as the vertical alignment promoter due to their low surface energy; 3) the side chains of the other block

are composed of functionalities acting as reactive sites for lithography and substrate adhesion moieties giving an additional driving force for vertical alignment. The modularity of the bottom-up synthetic approach leads to efficient top-down lithography at the molecular level.

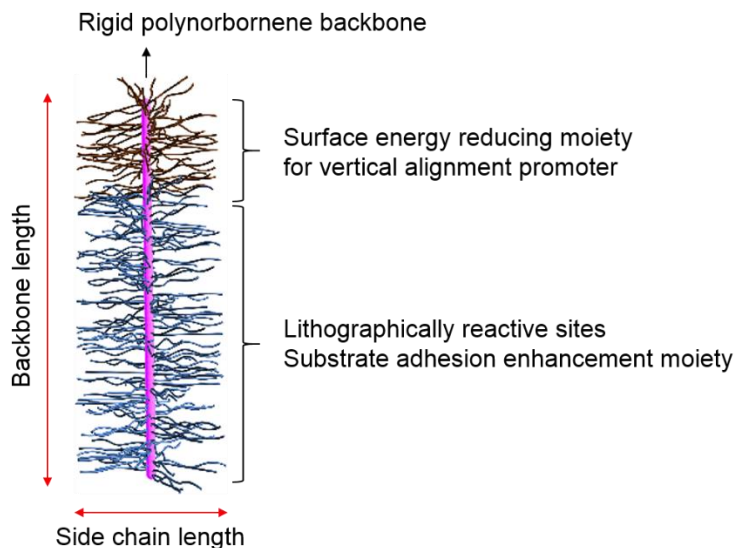


**Figure 1.4.** Cylindrical diblock brush polymers for lithographic usage with their dimensional and compositional variations.

Chapter II is focused on the preparation of nanoscopic cylindrical diblock brush terpolymers (DBTs) for negative-tone photoresists. Poly(tetrafluoro-*p*-hydroxystyrene) is used as the surface energy reducing moiety. Poly(*p*-hydroxystyrene) and poly(phenylmaleide) function as the reactive site for acid-catalyzed crosslinking chemistry and the substrate adhesion moiety, respectively. The vertical alignment of the cylindrical brush polymers on Si wafers is analyzed by surface analysis tools. Furthermore, the lithographic performance of negative-tone CARs based on the DBTs is studied by EBL.

In Chapter III, the self-assembly behavior of DBT within thin films upon variation of the composition and dimensions is thoroughly investigated. DBTs with three different fluoropolymers acting as the surface energy reducing moiety are prepared. The effects of composition, fluorine content, block length, and relative ratio of the graft versus backbone on the vertical alignment and phase segregation of the DBTs in thin films are studied by surface analysis tools such as atomic force microscopy (AFM), contact angle analysis, X-ray photoelectron spectroscopy (XPS), and secondary-ion mass spectrometry (SIMS).

In Chapter IV, the strategy of vertically alignable DBTs is applied to positive-tone resist materials. Different from the crosslinking chemistry of poly(*p*-hydroxystyrne), acid-catalyzed deblocking chemistry is utilized by installing acid-labile tertiary ester moieties as reactive sites in positive-tone resist materials. Also, a polar lactone is chosen as the substrate adhesion moiety. The vertical alignment and lithographic performance of positive-tone DBTs are examined.

## CHAPTER II

# NANOSCOPIC CYLINDRICAL DUAL CONCENTRIC AND LENGTHWISE BLOCK BRUSH TERPOLYMERS AS COVALENT PRE-ASSEMBLED HIGH RESOLUTION AND HIGH SENSITIVITY NEGATIVE-TONE PHOTORESIST MATERIALS\*

### 2.1. Introduction

Since chemically-amplified lithographic techniques were established in the 1980s,<sup>65,66</sup> functional polymer-based chemically-amplified resists (CARs) have been investigated intensively to meet the simultaneous requirements of high sensitivity, high resolution, and low line-edge roughness (LER) for photolithography and other top-down lithographic techniques.<sup>67-71</sup> To date, varieties of CARs have been commercialized and extensively used to facilitate latent pattern features on a sub-30 nm scale.<sup>67-71</sup> As a new pathway to extend the size roadmap of microelectronic devices,<sup>72</sup> block copolymer lithography (BCL)<sup>21,73</sup> has emerged as a powerful bottom-up lithographic technique. BCL involves supramolecular assembly of block copolymers (BCPs) into periodic arrays of diverse morphologies within thin films on a scale of tens of nanometers.<sup>74-79</sup> To fabricate microelectronic circuitry, the BCPs are assembled into domains of differential

---

\*Reprinted with permission from “Nanoscopic Cylindrical Dual Concentric and Lengthwise Block Brush Terpolymers as Covalent Pre-assembled High Resolution and High Sensitivity Negative-tone Photoresist Materials” by Guorong Sun, Sangho Cho, Corrie Clark, Stanislav V. Verkhoturov, Michael J. Eller, Ang Li, Adriana Pavía-Jiménez, Emile A. Schweikert, James W. Thackeray, Peter Trefonas, and Karen L. Wooley, *J. Am. Chem. Soc.* **2013**, 135(11), 4203-4206. Copyright 2013 American Chemical Society.

composition, typically with cylindrical or lamellar morphologies, oriented perpendicular to the substrate surface.<sup>74,78-84</sup> The morphology and orientation of BCP assemblies rely on the extent of immiscibility between covalently bonded block segments and on the chemical composition, block lengths, and block length ratio of the structural components,<sup>21,73</sup> requiring precise control to obtain large-scale vertical alignment of cylindrical assemblies.<sup>76-84</sup>

Beyond linear polymers, there is increasing interest in exploiting polymers with nonlinear topologies as photoresist materials, such as Fréchet's dendritic polymers<sup>85</sup> and Hadziioannou's hyperbranched polymers. In both cases, the branched architectures of the polymer framework constrains the chain entanglement and molecular sizes, thereby enhancing the overall patterning performance of the resists (i.e., higher sensitivity and lower LER) compared with the linear-polymer counterparts.

Inspired by these achievements, we developed a novel approach for photoresist polymer materials involving preconstruction of individually or collectively addressable block brush/graft terpolymer molecular brushes<sup>86</sup> that can align vertically on a substrate to form negative-tone molecular-scale resist features (Figure 2.1). The brush architecture was selected because it provides facile access to cylindrical nanoscopic objects<sup>51,87-90</sup> without the need for the supramolecular assembly processes that are typical with linear BCL. The diversity of chemical compositions and sizes can be tuned throughout the macromolecular brush framework with a high degree of control over the synthetic chemistry. The modularity of the bottom-up synthetic approach, based on sequentially "grafting-through"<sup>51,87-90</sup> pre-synthesized polymer segments (macromonomers) with

different compositions and functions for substrate alignment and cross-linking chemistry, respectively, into different regions of the molecular brush architecture, leads to efficient top-down patterning at the molecular level. As the current studies show, variation of the overall and relative lengths of the grafts versus the backbone allows the concentric and lengthwise dimensions to be modified conveniently, and control over the compositional placement within different regions of the cylindrical macromolecular framework provides a mechanism for aligning the polymer brushes and achieving electron-beam-generated patterns of a few macromolecules.

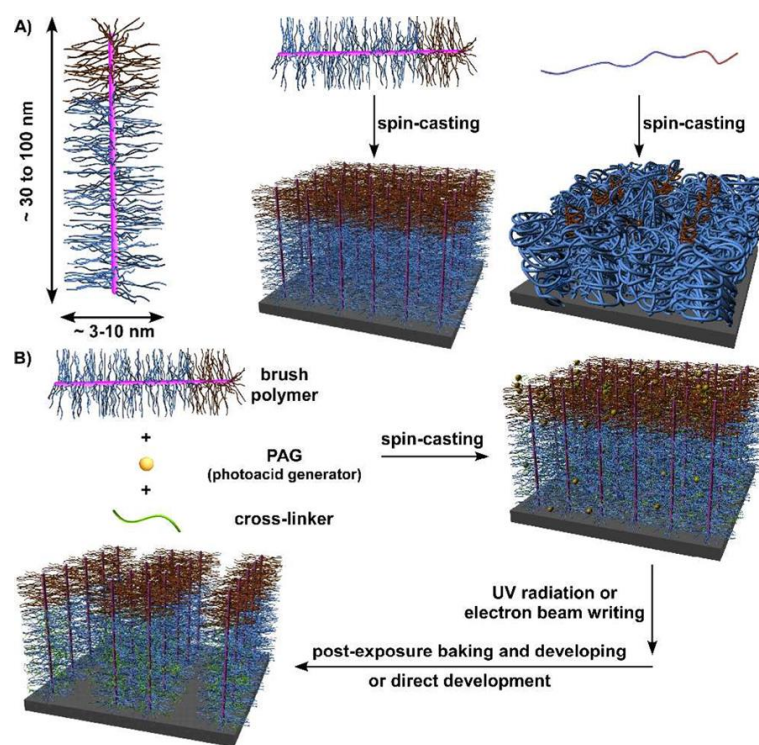


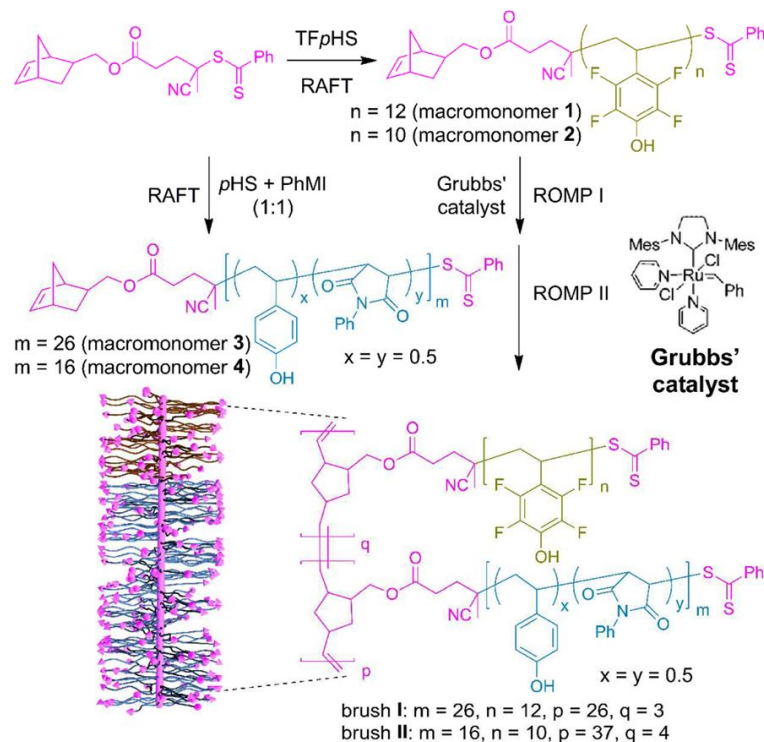
**Figure 2.1.** (a) Schematic representation of the targeted dimensions for the diblock brush terpolymers (left), their ideal alignment after deposition as a monolayer thin film (center), and comparison with linear block copolymer thin films that require multi-molecular supramolecular assembly with morphological directionality (right). (b) Schematic diagram of the overall strategy.

## 2.2. Results and Discussion

As shown in Figure 2.1b, spin-casting deposition of a solution of the diblock brush terpolymer (DBT) and a photoacid generator (PAG) results in vertical alignment of the brushes on the substrate as a PAG-containing monomer. UV or electron-beam irradiation through a predesigned pattern produces acid to promote cross-linking within the irradiated areas, with or without a postbaking step. Finally, solvent development reveals the latent patterned features. The target DBTs in this study were comprised of densely-grafted poly(tetrafluoro *p*-hydroxystyrene) (PTF*p*HS) and poly(*p*-hydroxy styrene-*co*-*N*-phenyl maleimide) [P(*p*HS-*co*-PhMI)] side chains covalently tethered along a rigid polynorbornene (PNB) backbone in a block manner. The fluorinated P(NB-*g*-PTF*p*HS) segment acted as the vertical alignment promoter because of the relatively lower surface energy of fluoropolymers.<sup>91</sup> The phenol functionalities accommodated within the P(NB-*g*-P(*p*HS-*co*-PhMI)) structural segments provided attractive interactions with the substrate surface and also served as reactive sites for acid-catalyzed electrophilic aromatic substitution cross-linking chemistry.



**Scheme 2.1.** Synthesis of P(NB-*g*-PTFpHS)-*b*-P(NB-*g*-P(*p*HS-*co*-PhMI)) diblock brush terpolymers



The P(NB-*g*-PTFpHS)-*b*-P(NB-*g*-P(*p*HS-*co*-PhMI)) brushes were synthesized by applying sequential ring-opening metathesis polymerization (ROMP)<sup>92</sup> of NB-terminated macromonomers [NB-PTFpHS and NB-P(*p*HS-*co*-PhMI), respectively] (Scheme 2.1). Consequently, the construction of structurally well-defined NB-PTFpHS and NB-P(*p*HS-*co*-PhMI) macromonomers was critical for controlled block copolymerization during implementation of “grafting-through” ROMP. To date, direct controlled radical polymerization (CRP) of vinylphenol-based monomers remains a challenge, so protection and deprotection chemistries are frequently employed to obtain well-defined poly(vinyl phenol) by CRPs.<sup>77,80</sup> Herein we report a copolymerization method based on reversible addition-fragmentation chain transfer (RAFT),<sup>93</sup> the most versatile CRP methodology, to

produce vinylphenol copolymers with well-defined structures, predictable and controllable molecular weights (MWs), and a norbornenyl  $\alpha$ -chain terminus for use in the subsequent two-stage ROMP to afford the desired DBTs of variable dimensions.

Although the RAFT homopolymerization of TF*p*HS from a NB-terminated dithioester chain-transfer agent (CTA) proceeded successfully to give macromonomers **1** and **2** [Scheme 1; see Figure 2.2 and Table 2.1, entries 1 and 2], the RAFT homopolymerization of *p*HS (Table 2.1, entries 3 and 4) afforded polymers with broader MW distributions (Figure 2.3), indicating inadequate control. To obtain a macromonomer of *p*HS for use as the reactive majority of the molecular brush structures, we turned to RAFT copolymerization, as the free-radical copolymerizations of *p*HS with methacrylates have recently been reported.<sup>94</sup> From the viewpoint of the comonomer pair, N-substituted maleimides were more effective candidates than methacrylates for RAFT copolymerization with *p*HS because of their well-documented low tendency to homopolymerize when undergoing significant cross-propagation with styrenic comonomers.<sup>95,96</sup> RAFT copolymerization using *p*HS and PhMI as a comonomer pair at a fixed 1:1 feed ratio afforded two macromonomers having different chain lengths (Table 2.1, entries 5 and 6). The well-defined structures of NB-P(*p*HS<sub>13</sub>-*co*-PhMI<sub>13</sub>) (**3**) and NB-P(*p*HS<sub>8</sub>-*co*-PhMI<sub>8</sub>) (**4**) (Scheme 2.1) were verified by <sup>1</sup>H NMR analyses (Figure 2.4b and c through the ca. 1:1 integral ratio of NB alkenyl protons (6.08 ppm) to the *m*-phenyl protons of the RAFT agent chain end (7.85 ppm). Gel-permeation chromatography (GPC) showed that both **3** and **4** had monomodal MW distributions with relatively low polydispersity indices (PDIs) of ca. 1.20 (Figure 2.4a). **1** was also utilized in this

copolymerization method as a macro-RAFT CTA to afford the diblock terpolymer NB-PTFpHS<sub>12</sub>-*b*-P(*p*HS<sub>48</sub>-*co*-PhMI<sub>48</sub>) diblock terpolymer (Figure 2.5), which served as the block terpolymer linear control (**LC**) for the following lithographic studies.

**Table 2.1.** RAFT polymerizations of TFpHS and *p*HS; RAFT copolymerizations of *p*HS and PhMI

entry	[M] <sub>0</sub> : [NB-CTA] <sub>0</sub> : [AIBN] <sub>0</sub> [mmol/L]	T [°C]	t [h]	Conversion <sup>a</sup>	M <sub>n</sub> , NMR [Da]	M <sub>n</sub> , GPC <sup>b</sup> [Da]	M <sub>n</sub> , GPC <sup>c</sup> [Da]	PDI <sup>d</sup>
1	2220:74:7.4 <sup>e</sup>	65	11	45%	2,690	1,860	2,750	1.07
2	2200:110:6.6 <sup>e</sup>	65	11	45%	2,300	1,270	2,450	1.08
3	555:11.1:1.67 <sup>f</sup>	65	21	10%	ND	ND	ND	ND
4	833:16.6:3.32 <sup>g</sup>	65	21	15%	ND	ND	ND	ND
5	1886:47.1:4.71 <sup>h</sup>	65	6.5	55%	4,200	3,530	6,870	1.20
6	2080:104:5.2 <sup>h</sup>	65	4.5	51%	2,730	2,550	3,800	1.12

<sup>a</sup> By <sup>1</sup>H NMR. <sup>b</sup> By GPC, RI detector. <sup>c</sup> By GPC, light scattering detector. <sup>d</sup> By GPC. <sup>e</sup> M = TFpHS, 2-butanone as solvent. <sup>f</sup> M = *p*HS, 2-butanone as solvent. <sup>g</sup> M = *p*HS, 1,4-dioxane as solvent. <sup>h</sup> M = *p*HS + PhMI (1:1), 1,4-dioxane as solvent. ND: not determined.

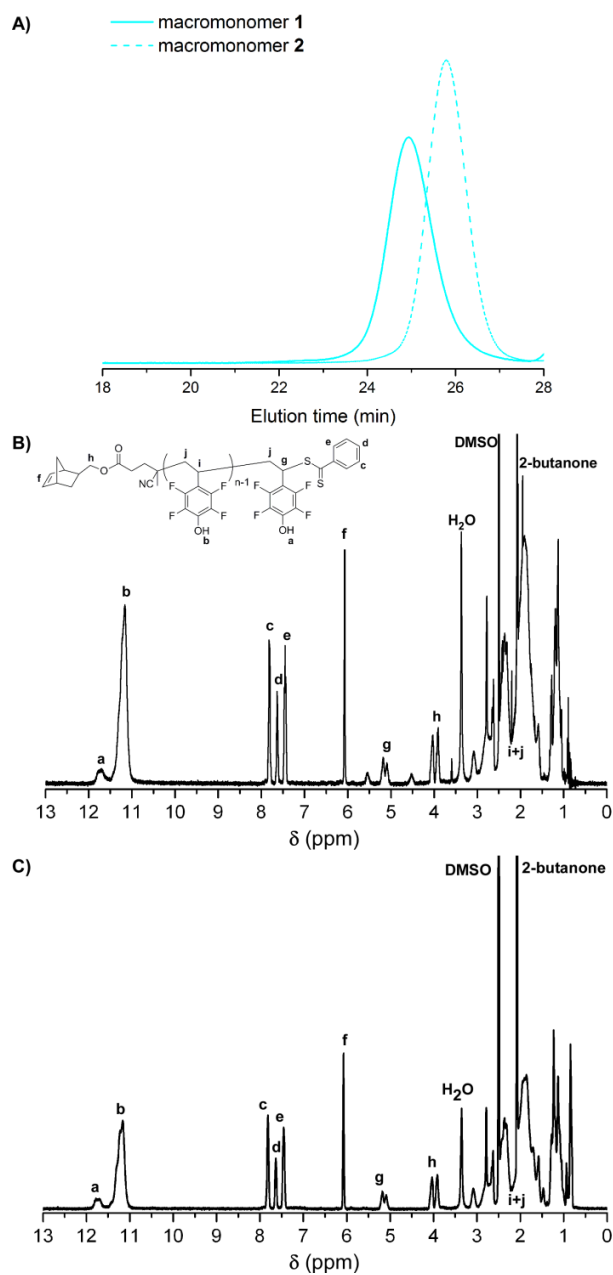


**Figure 2.2.** The GPC profiles (a) and  $^1\text{H}$  NMR (500 MHz,  $\text{DMSO}-d_6$ ) spectra (b, c) for the NB-PTFpHS macromonomers prepared from RAFT homopolymerizations of TFpHS. The spectrum in (b) was from macromonomer **1** and the spectrum in (c) was from macromonomer **2**.

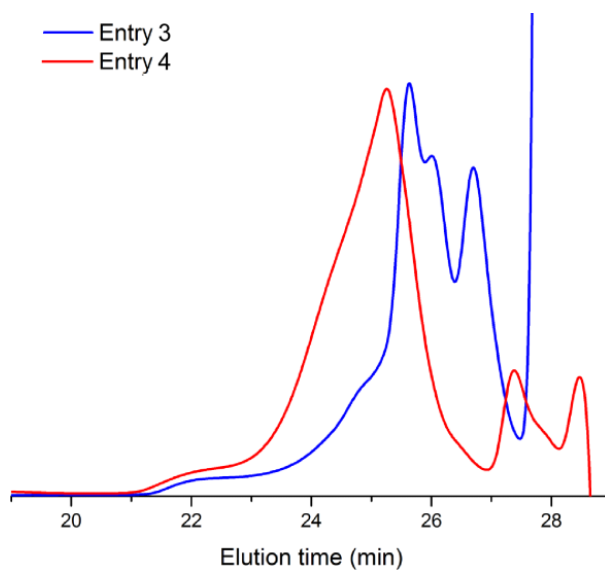


**Figure 2.3.** The normalized GPC profiles of the RAFT homopolymerizations of *p*HS; entries are from Table 2.1.

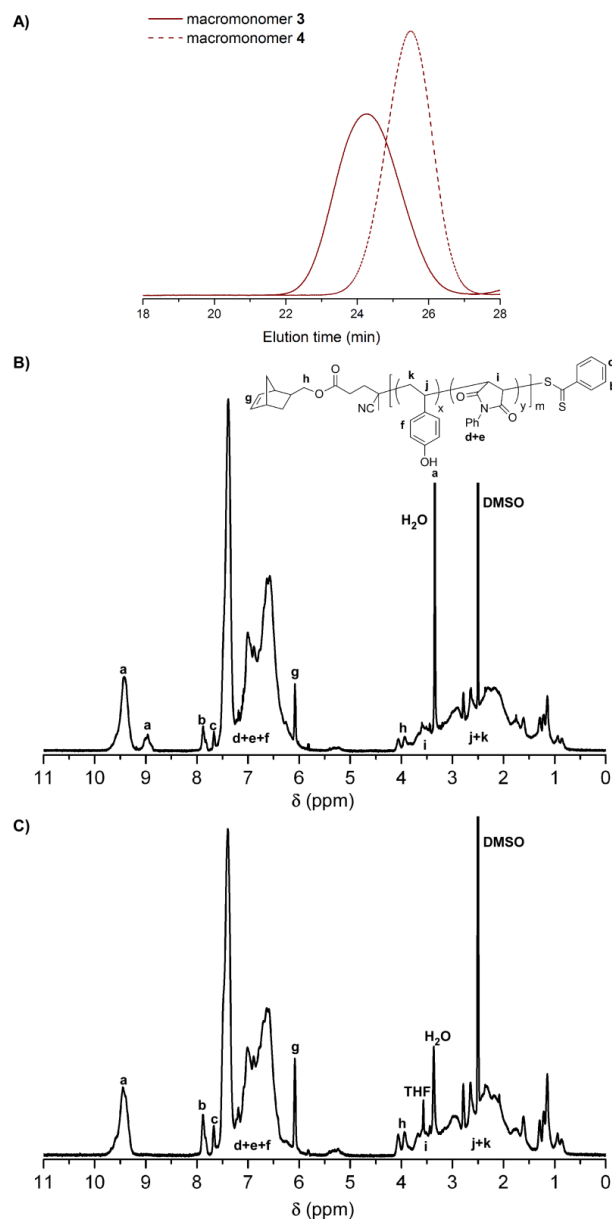


**Figure 2.4.** The GPC profiles (a) and  $^1\text{H}$  NMR (500 MHz,  $\text{DMSO}-d_6$ ) spectra (b, c) for the NB-P(*p*HS-*co*-PhMI) macromonomers prepared from RAFT copolymerizations of *p*HS and PhMI. The spectrum in (b) was from macromonomer **3** and the spectrum in (c) was from macromonomer **4**.

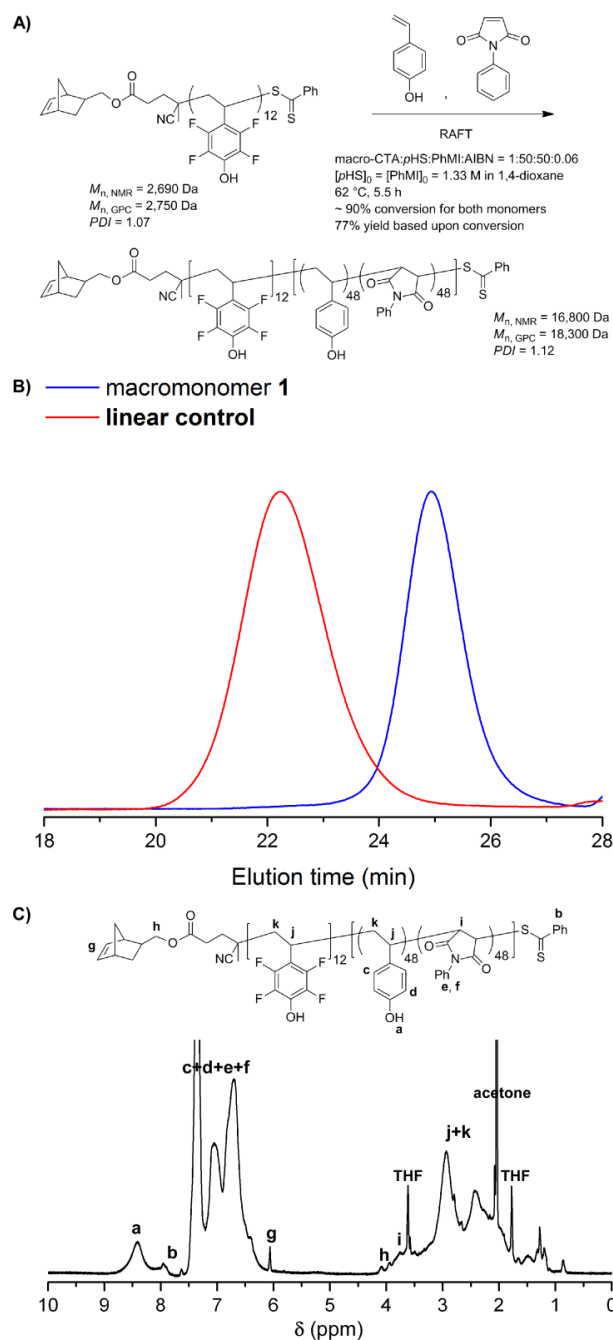


**Figure 2.5.** Preparation and characterizations of **LC** [NB-PTFpHS<sub>12</sub>-*b*-P(*p*HS<sub>48</sub>-*co*-PhML<sub>48</sub>)]. (a) Schematic illustration of the synthesis. (b) GPC profiles of the macro-CTA (NB-PTFpHS<sub>12</sub>, blue) and **LC** (red). (c) <sup>1</sup>H NMR (500 MHz, acetone-*d*<sub>6</sub>) spectrum of the NB-PTFpHS<sub>12</sub>-*b*-P(*p*HS<sub>48</sub>-*co*-PhML<sub>48</sub>).

Sequential ROMPs of ‘**1** and **3**’ or ‘**2** and **4**’ with the modified Grubbs’ catalyst were then used to construct P(NB-*g*-PTF*p*HS)-*b*-P(NB-*g*-P(*p*HS-*co*-PhMI)) DBTs with variation in both concentric and lengthwise dimensions (Scheme 2.1). The DBT [P(NB-*g*-PTF*p*HS<sub>12</sub>)<sub>3</sub>-*b*-P(NB-*g*-P(*p*HS<sub>13</sub>-*co*-PhMI<sub>13</sub>))<sub>26</sub>] (**I**) ( $M_n^{\text{GPC}} = 189$  kDa, PDI = 1.25, 1.45 wt% F) was prepared at [catalyst]:[**1**]:[**3**] feed ratio of 1:4:30. For the DBT [P(NB-*g*-PTF*p*HS<sub>10</sub>)<sub>4</sub>-*b*-P(NB-*g*-P(*p*HS<sub>8</sub>-*co*-PhMI<sub>8</sub>))<sub>37</sub>] (**II**) ( $M_n^{\text{GPC}} = 152$  kDa, PDI = 1.26, 2.00 wt% F), a 1:4.2:28 [catalyst]:[**2**]:[**4**] feed ratio was applied. The polymerizations were monitored by GPC, and obvious peak shifts were noticed during each ROMP process (Figure 2.6a and b). The reaction efficiencies were estimated as 80% for **1** and 90% for **2** after 40 min. In ROMP II, both **3** and **4** showed >90% conversions after 180 min to afford **I** and **II** with narrow, monomodal MW distributions. The concentric block structures within **I** and **II** were verified by <sup>1</sup>H NMR spectroscopy and differential scanning calorimetry. Two sets of phenolic protons centered at 9.50 and 11.20 ppm (Figure 2.6c) and two glass transition temperatures at 130 and 150 °C were observed, corresponding to the P(*p*HS-*co*-PhMI) and PTF*p*HS grafts, respectively.



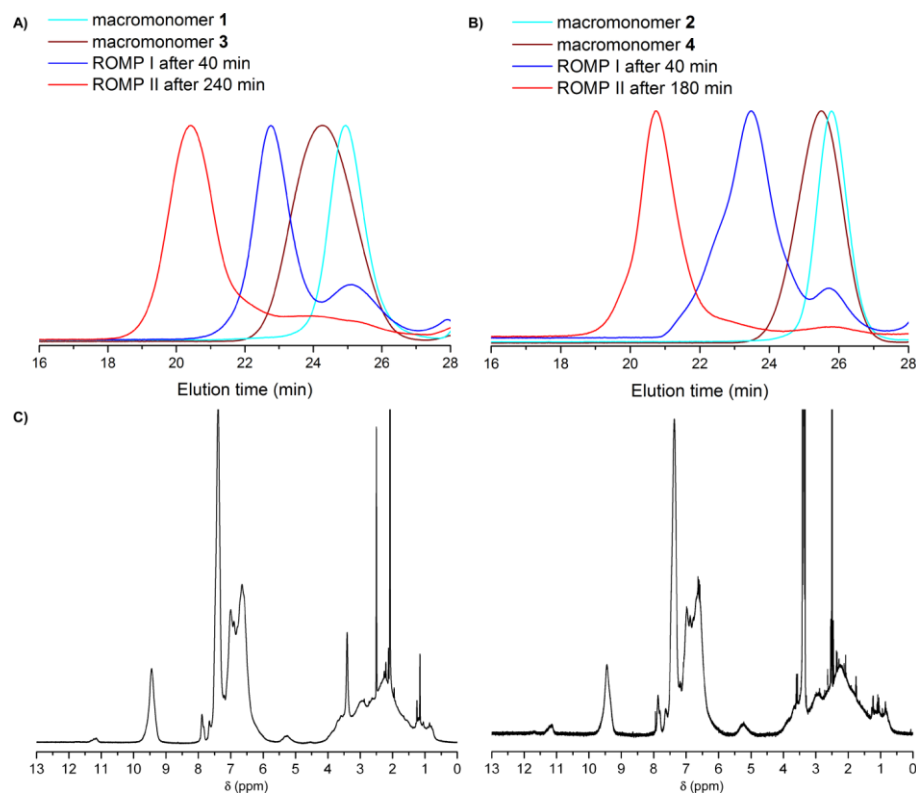


**Figure 2.6.** (a, b) The normalized GPC profile of the sequential ROMP for preparation of Brush **I** (a) and **II** (b), respectively. (c) <sup>1</sup>H NMR (500 MHz, *DMSO-d*<sub>6</sub>) spectra for the Brush **I** (left) and Brush **II** (right), respectively.

Polymer thin films were then prepared by spin-casting 1.0 wt% of solutions of **I**, **II**, or **LC** in cyclohexanone onto silicon wafers. As characterized by tapping-mode atomic force microscopy (AFM), the 25 nm thick **LC** film showed noticeable heterogeneity (Figure 2.7a). By comparison, the films of **I** and **II** exhibited sufficiently homogeneous surface topography (Figure 2.7b and c) with root-mean-square roughness of <0.2 nm. The film thicknesses measured by AFM were  $25 \pm 1$  nm for **I** and  $30 \pm 1$  nm **II**, in agreement with estimations of the extended brush backbone lengths (23 and 30 nm, respectively). The surface topographical homogeneities and the approximately monomolecular layer

thicknesses of the brush films suggested that the brush polymer components within the films adopted orientations perpendicular to the wafer surface.<sup>97,98</sup>

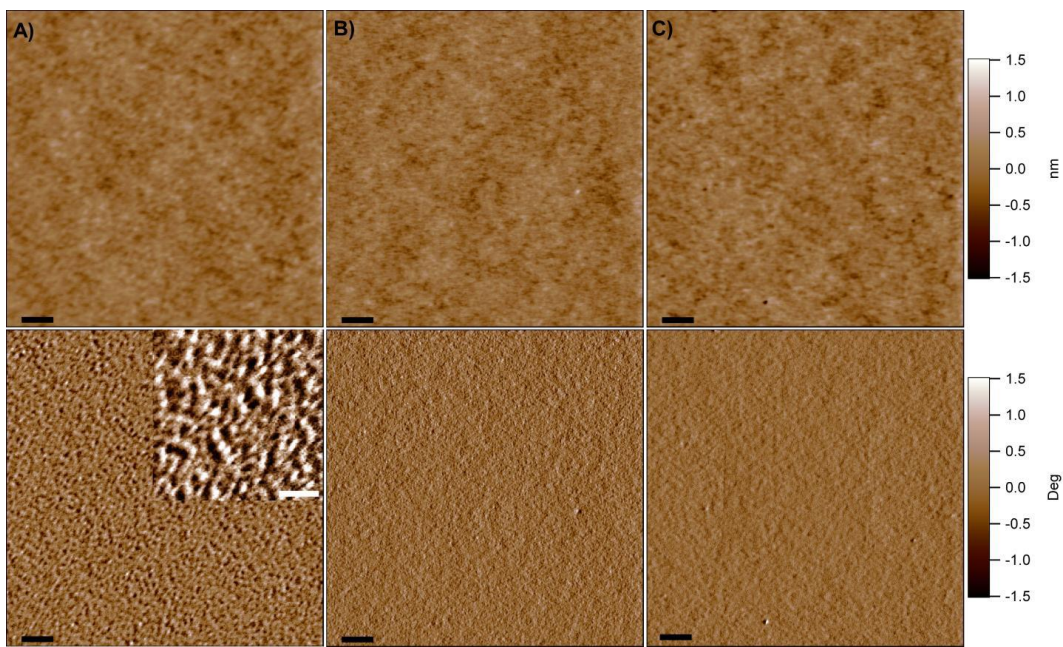


**Figure 2.7.** Tapping-mode AFM height (top) and phase (bottom) images of thin films without acetone annealing obtained from  $5 \times 5 \mu\text{m}$  area. (a) Film from **linear control**. (b) Film from brush **I**. (c) Film from brush **II**. Scale bar (black): 500 nm. The inserted image in (a) was the representative part of the linear control film phase imaging obtained from  $2 \times 2 \mu\text{m}$  area (white scale bar: 250 nm).

The vertical alignments of brushes across the wafer surface were confirmed by the secondary-ion mass spectrometry (SIMS) fluorine depth profiles (Figure 2.8). The F species in brush **II** were predominantly located within the topmost layer of the film with a thickness of ca. 7 nm and there was no F "signal" was detected at depths  $>13$  nm.<sup>99</sup> The vertical alignments could be attributed to the intrinsically cylindrical topology of DBTs induced by the strong size-exclusion effects between covalently tethered dense polymer grafts. Meanwhile, the fluorinated block segments in the DBTs would promote and assist

the vertical alignments as a result of their preferential surface migration driven by their relatively lower surface energies. The extents of brush vertical alignment were quantified by X-ray photoelectron spectroscopy (XPS) (Figure 2.9) and C<sub>60</sub> SIMS (Figure 2.10) through analyses of relative surface F contents [i.e., the ratios between measured and theoretical (100% vertical alignments of brushes) value]. For both brushes, the XPS measurements showed that ca. 55% of the brushes within films adopted vertical alignments across the substrate surface without any special treatments (Table 2.2). SIMS showed that ca. 65% of the brushes preferred the expected vertical orientations, consistent with the XPS results. Solvent-assisted annealing (SAA) of the brush films using acetone significantly improved the extent of vertical alignment, as the surface F contents increased to become approximately equal to the theoretical values (Table 2.2). The enhanced vertical alignments after SAA was also observed in the SIMS depth profile (Figure 2.11) and further increased the hydrophobicities of the film surfaces, as confirmed by increased static water contact angles and decreased surface energies of the films (Table 2.3).

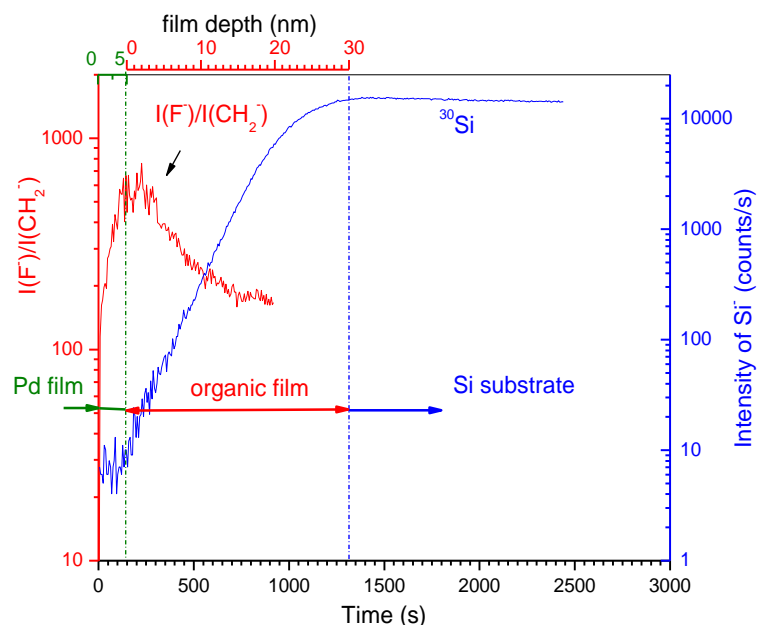


**Figure 2.8.** SIMS fluorine depth profile of film prepared from spin-casting brush **II** on silicon wafer. *Sputtering rates:* film of 80 wt% Pt/20 wt% Pd alloy: 0.15 nm/s (sputtering yield: 15 atoms/projectile); Si wafer: 0.042 nm/s (sputtering yield: 3.37 atoms/projectile). The depth scale of the organic film corresponds to the thickness of film ( $\sim 30$  nm) measured by AFM.

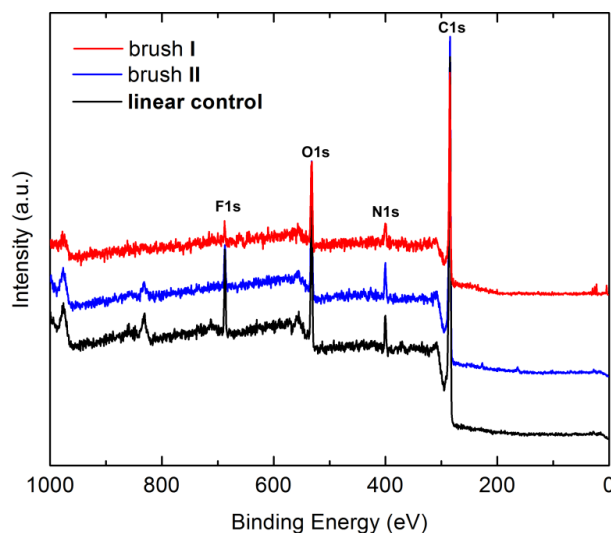


**Figure 2.9.** XPS survey spectra of thin films prepared from brush **I** (red profile), brush **II** (blue profile), and **linear control** (black profile) on silicon wafer.

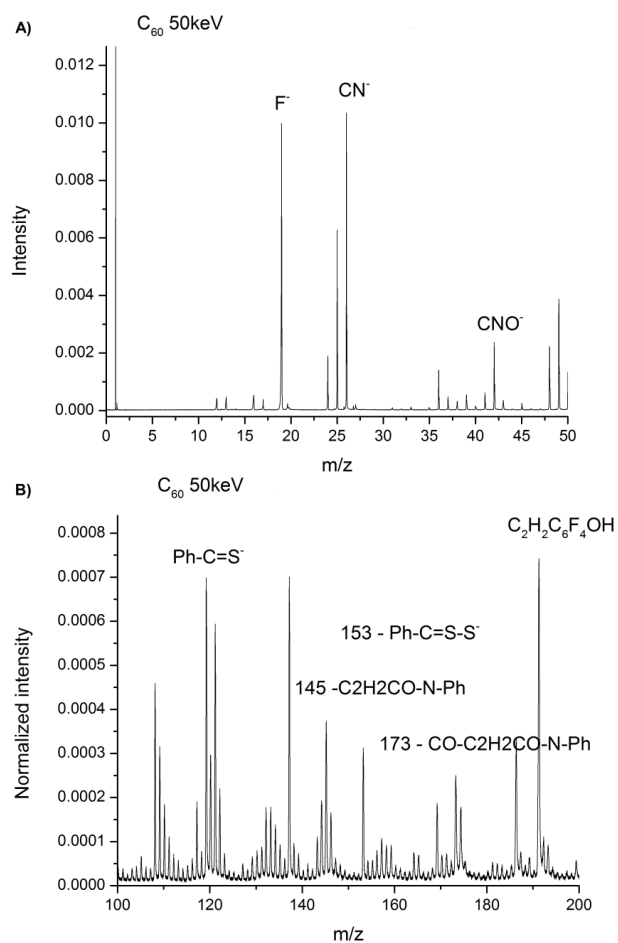


**Figure 2.10.** Representative  $C_{60}$  SIMS spectra of brushes at  $m/z = 0-50$  range (a) and  $m/z = 100-200$  range (b), respectively.

**Table 2.2.** Relative ratios of elements in polymer film surface from XPS measurements.

		C1s @ 285 eV	N1s @ 400 eV	O1s @ 532 eV	F1s @ 688 eV
<b>Brush I</b>	Spin-cast	75.5 %	4.9 %	17.9 %	1.7 %
	Solvent-annealed	72.2 %	4.0 %	20.8 %	3.1 %
	Random distributed	81.2 %	4.3 %	12.9 %	1.7 %
	Ideally vertical aligned <sup>a</sup>	80.4 %	4.1 %	12.6 %	3.0 %
<b>Brush II</b>	Spin-cast	83.1 %	3.6 %	10.7 %	2.7 %
	Solvent-annealed	80.8 %	3.7 %	10.7 %	4.8 %
	Random distributed	81.2 %	4.2 %	12.6 %	2.0 %
	Ideally vertical aligned <sup>a</sup>	79.3 %	3.8 %	12.0 %	5.0 %
<b>Linear control</b>	Spin-cast	80.1 %	3.4 %	12.3 %	4.2 %
	Solvent-annealed	79.2 %	3.9 %	12.0 %	4.9 %
	Random distributed	79.4 %	4.0 %	12.8 %	3.9 %
	Ideally vertical aligned <sup>a</sup>	80.2 %	0.2 %	10.1 %	9.5 %

<sup>a</sup>Depth up to 10 nm from the film surface.

$$\% \text{ Vertical alinement} = \frac{F_{\text{sample}}}{F_{\text{ideal}}} \times 100$$

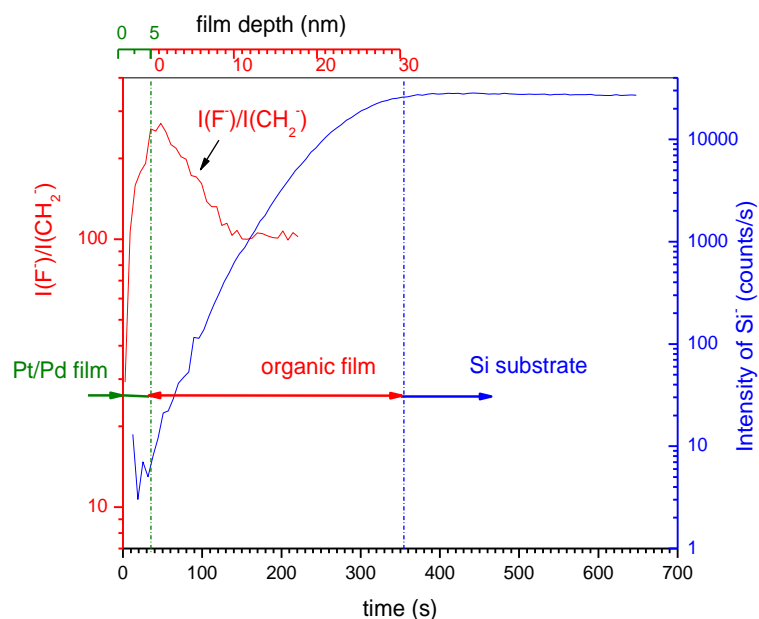


**Figure 2.11.** SIMS fluorine depth profile of film prepared from spin-casting of brush **II** on silicon wafer and annealed 20 h under acetone atmosphere. *Sputtering rates:* film of 80wt% Pt/20wt% Pd alloy: 0.15 nm/s (sputtering yield: 15 atoms/projectile); Si wafer: 0.042 nm/s (sputtering yield: 3.37 atoms/projectile). The depth scale of the organic film corresponds to the thickness of this film (~30 nm) measured by AFM.

**Table 2.3.** Summary of static contact angles and surface energies of polymer films.

		Static contact angle [°]		Surface energy [mJ/m <sup>2</sup> ]
		Water	Diiodomethane	
Brush <b>I</b>	Spin-cast	58 ± 2	26 ± 1	57.1
	Solvent-annealed	73 ± 2	34 ± 1	47.9
Brush <b>II</b>	Spin-cast	57 ± 2	24 ± 1	58.4
	Solvent-annealed	73 ± 1	37 ± 1	47.1
<b>Linear control</b>	Spin-cast	73 ± 1	31 ± 1	48.9
	Solvent-annealed	71 ± 2	40 ± 1	47.0

Finally, the lithographic behaviors of the molecular brush-based resists were explored. Triphenylsulfonium perfluoro-1-butanesulfonate was used as PAG and *N,N,N',N',N'',N''*-hexakis(methoxymethyl)-1,3,5-triazine-2,4,6-triamine (HMMM) was selected as both multivalent cross-linker and acid quencher. With a typical formulation for linear poly(vinylphenol)-based CARs [0.75:0.15:0.10 (w:w:w) brush:HMMM:PAG in cyclohexanone],<sup>100</sup> negative-tone post-exposure baking electron-beam lithography (PEB-EBL) of the brush CARs (**CAR-I** and **CAR-II**) was performed (Figure 2.12). The lithographic performance was evaluated by AFM measurements of the heights and widths of lines in designed pattern with line width ranging from 10–100 nm at two exposure dosages (250 and 400  $\mu\text{C}/\text{cm}^2$ ). As opposed to the neat molecular brush materials, the static contact angles of the spin-cast and the acetone-annealed resist films did not exhibit apparent differences (data not shown), which might be associated with the migration of PAGs to the topmost layer of the resist films due to the F-enriched counterion in the PAG molecule. Therefore, the prepared resist films with thicknesses of  $25 \pm 2$  nm (as measured by AFM) were directly used for lithographic studies.



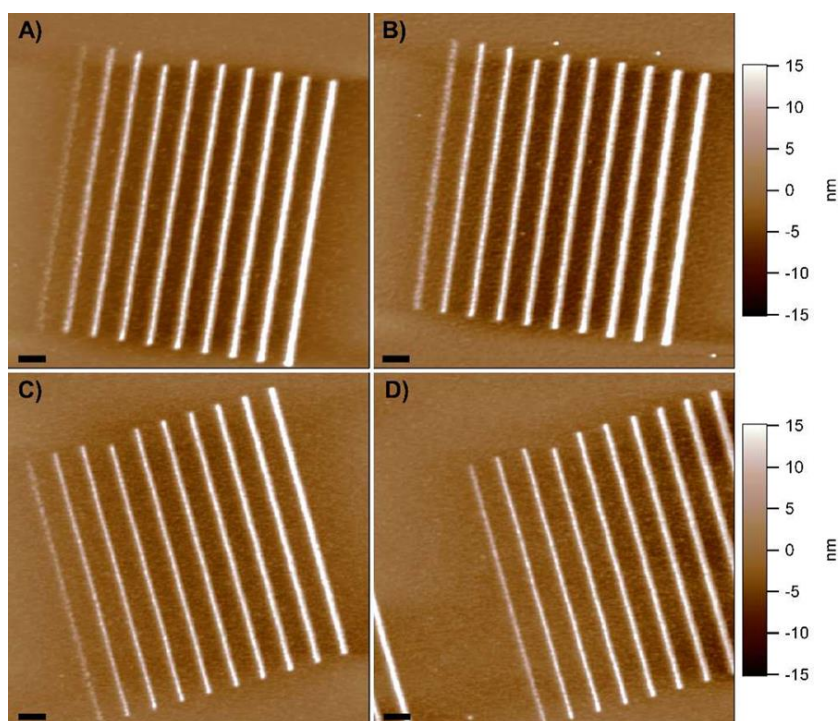


**Figure 2.12.** Tapping mode AFM height images of patterns generated by PEB-EBL. (a, b) **CAR-I** and (c, d) **CAR-II** at 250 and 400  $\mu\text{C}/\text{cm}^2$  exposure dosage, respectively. Scale bars: 500 nm.

Both **CAR-I** and **CAR-II** could be used to create patterns with full line integrities at each exposure dosage (Figure 2.12). In contrast, the patterns from **CAR-LC** had rational features for the 50–100 nm wide lines (Figure 2.13), even at 400  $\mu\text{C}/\text{cm}^2$  dosage. For the brush CARs in this study, the features of the latent 30–100 nm lines were satisfactory (Figure 2.14), especially for the **CAR-II** after 400  $\mu\text{C}/\text{cm}^2$  exposure (Figure 2.12d). We speculated that the better latent line-width features of **CAR-II** were induced by the intrinsic geometric factor of brush **II**, whose relatively shorter grafts rende it a “thinner” column by reducing the chain entanglements after vertical alignment on the substrate surface. Under current instrumental conditions, a ca. 30 nm isolated line was obtained for

**CAR-II** under the surveyed conditions. Thus, we can concluded that tuning of the lengthwise and concentric dimensions of the brush plays a critical role in the lithographic performance and that eventually molecular pixels could be realized through further systematic optimizations of brush backbone and side-chain lengths and chemical compositions.

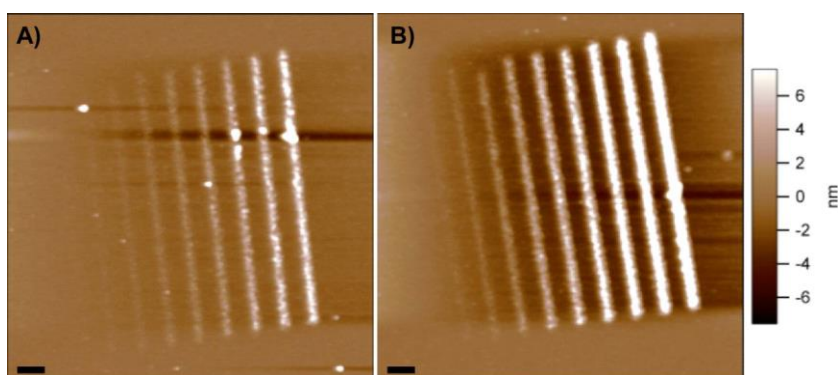


**Figure 2.13.** Tapping mode AFM height images of patterns generated by PEB-EBL of **CAR-LC** at  $250 \mu\text{C}/\text{cm}^2$  (a) and  $400 \mu\text{C}/\text{cm}^2$  (b) exposure dosage, respectively. Scale bar: 500 nm.

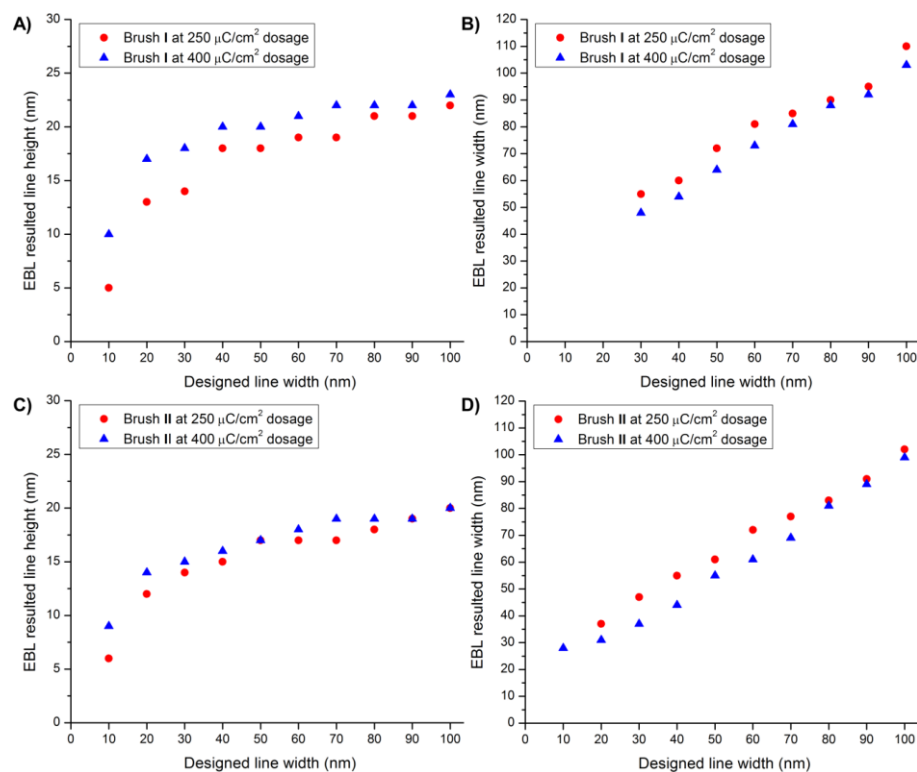


**Figure 2.14.** Evaluations of the line height (a and c) and width (b and d) of the latent lines AFM, respectively, which were generated by PEB-EBL of **CAR-I** and **CAR-II** at 250 and 400  $\mu\text{C}/\text{cm}^2$  exposure dosage and  $\text{TMAH}_{(\text{aq.})}$  development. The height and width were measured by tapping-mode AFM. The line width was measured at 75% of the line height and deducted  $2 \times \text{AFM tip diameter}$  (10 nm).

We also synthesized  $\text{P}(\text{NB-}g\text{-P}(\text{pHS}_{13}\text{-}co\text{-PhMI}_{13}))_{24}$  as a brush control (**BC**) lacking the fluorocarbon-based block (Figure 2.15a) and subjected it to PEB-EBL under similar conditions. The resulting patterns did not exhibit the designed features (Figure 2.15b). Because of the lack of fluorinated cap, the **BC** adopted random alignment across the wafer surface, and cross-linking occurred throughout the film because of the high sensitivity observed for brush CARs. These results further demonstrate the necessity of the combination of brush architecture for high sensitivity and the block brush composition for vertical alignment and high-resolution imaging of brush polymers within the resist film.

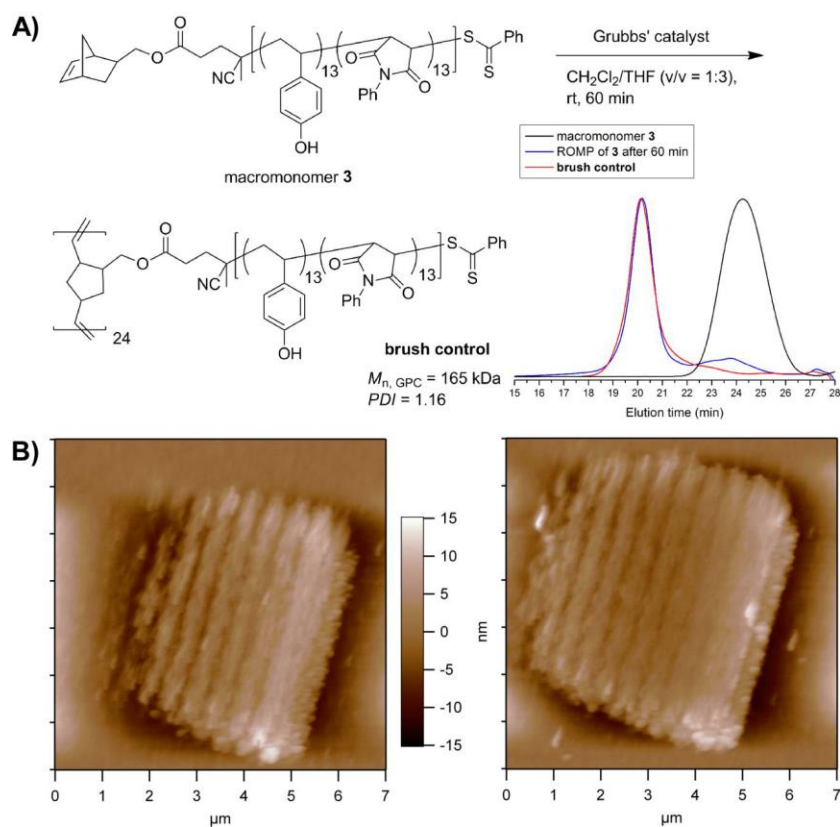


**Figure 2.15.** (a) Synthesis of **BC**. (b) Tapping mode AFM height images of patterns generated by PEB-EBL of **CAR-BC** at 250  $\mu\text{C}/\text{cm}^2$  dosage (a) and 400  $\mu\text{C}/\text{cm}^2$  exposure dosage (b).

Taking advantage of the higher sensitivity for the brush polymer CARs, we performed “direct”-EBL tests (i.e., direct development of the electron-beam-exposed resists with no PEB) of **CAR-I** and **CAR-II**. Interestingly, **CAR-II**, which showed better lithographic performance in PEB-EBL, could not generate latent patterns without PEB. In contrast, the “direct” EBL of **CAR-I** was achieved for >50 nm line features at an exposure dosage of 600  $\mu\text{C}/\text{cm}^2$  (Figure 2.16b), and the unexposed areas showed “cleaner” characteristics than the corresponding areas in PEB-EBL at an identical exposure dosage (Figure 2.16a vs 2.12b).

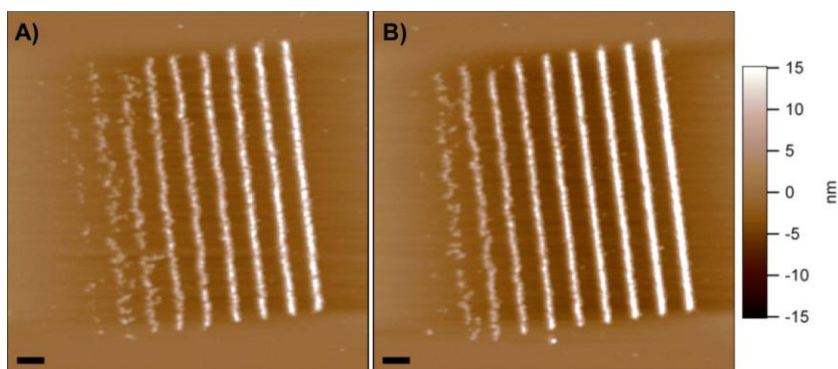


**Figure 2.16.** Tapping mode AFM height images of patterns generated by “direct”-EBL of **CAR-I** at  $400\ \mu\text{C}/\text{cm}^2$  (a) and  $600\ \mu\text{C}/\text{cm}^2$  (b) exposure dosage, respectively. Scale bar: 500 nm.

## 2.3. Experimental Section

### 2.3.1. Materials

The modified Grubbs catalyst,<sup>89</sup> 4-hydroxystyrene (*p*HS),<sup>101</sup> 2,3,5,6-tetrafluoro-4-hydroxystyrene (TF*p*HS),<sup>102</sup> and NB-CTA<sup>103</sup> were synthesized according to the literature reports. The *N,N,N',N',N'',N''*-hexakis(methoxymethyl)-1,3,5-triazine-2,4,6-triamine (HMMM) was purchased from TCI and used without further purification. The photoacid generator (PAG), triphenylsulfonium perfluoro-1-butanesulfonate for electron beam lithography (EBL), was provided by DOW Electronic Materials. Other chemicals were purchased from Aldrich, Acros, and VWR and were used without further purification unless otherwise noted. Prior to use, tetrahydrofuran (THF) was distilled over sodium and stored under N<sub>2</sub>. Dichloromethane (CH<sub>2</sub>Cl<sub>2</sub>) was distilled over calcium hydride and stored under N<sub>2</sub>.

### 2.3.2. Instruments

$^1\text{H}$  and  $^{13}\text{C}$  NMR spectra were recorded on a Varian 500 MHz spectrometer interfaced to a UNIX computer using Mercury software. Chemical shifts were referred to the solvent proton resonance. IR spectra were recorded on an IR Prestige 21 system (Shimadzu Corp.) and analyzed by using the IRsolution software.

The polymer molecular weight and molecular weight distribution were determined by Gel Permeation Chromatography (GPC). The GPC was conducted on a Waters 1515 HPLC (Waters Chromatography, Inc.) equipped with a Waters 2414 differential refractometer, a PD2020 dual-angle ( $15^\circ$  and  $90^\circ$ ) light scattering detector (Precision Detectors, Inc.), and a three-column series (PL gel  $5\mu\text{m}$  Mixed C,  $500\text{ \AA}$ , and  $10^4\text{ \AA}$ ,  $300 \times 7.5\text{ mm}$  columns; Polymer Laboratories, Inc.). The system was equilibrated at  $40^\circ\text{C}$  in THF, which served as the polymer solvent and eluent with a flow rate of  $1.0\text{ mL/min}$ . Polymer solutions were prepared at a known concentration ( $3 - 5\text{ mg/mL}$ ) and an injection volume of  $200\text{ }\mu\text{L}$  was used. Data collection and analysis were performed with Precision Acquire software and Discovery 32 software (Precision Detectors, Inc.), respectively. Inter-detector delay volume and the light scattering detector calibration constant were determined by calibration using a nearly monodispersed polystyrene standard (Polymer Laboratories,  $M_p = 90\text{ kDa}$ ,  $M_w/M_n < 1.04$ ). The differential refractometer was calibrated with standard polystyrene reference material (SRM 706 NIST), of known specific refractive index increment  $dn/dc$  ( $0.184\text{ mL/g}$ ). The  $dn/dc$  values of the analyzed polymers were then determined from the differential refractometer response.

The glass transition temperatures ( $T_g$ ) were measured by differential scanning calorimetry on a Mettler-Toledo DSC822 (Mettler-Toledo, Inc., Columbus, OH), with a heating rate of 10 °C /min. The measurements were analyzed by using Mettler-Toledo STARe software. The  $T_g$  was taken as the midpoint of the inflection tangent, upon the third heating scan. Thermogravimetric analysis (TGA) was performed under N<sub>2</sub> atmosphere using a Mettler-Toledo model TGA/SDTA851, with a heating rate of 5 °C /min. The measurements were analyzed by using Mettler-Toledo STARe software.

The thin film fluorine depth profiles of secondary ion mass spectrometry (SIMS) were obtained from a CAMECA 4F secondary ion mass spectrometer. Before measurement, the polymer film was coated with a thin layer of Pt/Pd alloy (80 wt%/20 wt%) at a thickness of 5 nm. The analyzed surface was sputtered by the 14.5 keV Cs<sup>+</sup> beam (diameter of ~1 μm) at a current of 6 nA. The raster was 500 × 500 μm<sup>2</sup> for the spin-casted sample, and 250 × 250 μm<sup>2</sup> for the acetone-annealed sample. The angle of incidence of the beam was 26°. The sputtering rates for polymer films, Pt/Pd film, and Si wafer were calculated by using the SRIM 2011.08 software.

The surface energy of the film was calculated with Owens–Wendt–Rabel–Kaelble (OWRK) method after measuring the contact angle with optical tensiometer (KSV Instruments, Attension Theta). The X-ray Photoelectron Spectroscopy (XPS) experiments were performed on a Kratos Axis Ultra XPS system with a monochromatic aluminum X-ray source (10 mA, 12 kV). The binding energy scale was calibrated to 285 eV for the main C1s peak.

The C<sub>60</sub>SIMS measurements were carried out with a custom-built SIMS instrument coupled to a time-of-flight (TOF) mass analyzer.<sup>104</sup> The instrument used in these studies is equipped with a C<sub>60</sub> effusion source capable of producing C<sub>60</sub><sup>+2</sup> projectiles with total impact energy of 50 keV. The SIMS analysis of the polymer samples was conducted in the superstatic regime, where less than 0.1% of the surface is impacted. This restriction ensured that each time the surface was impacted by a primary ion, an unperturbed area of the surface was sampled. The superstatic measurements were conducted in the event-by-event bombardment-detection mode, where a single primary ion impacted on the surface and the secondary ions were collected and analyzed prior to subsequent primary ions impacting the surface. All secondary ions detected in a single impact originated from a 10 nm radius on the surface.<sup>105</sup>

Each polymer sample was measured three times at different locations on the sample by TOF-SIMS. Each measurement consisted of  $\sim 3 \times 10^6$  projectile impacts on an area  $\sim 100 \mu\text{m}$  in radius. Multiple measurements were performed to ensure sample consistency. A quantitative estimate of surface coverage of fluorine containing molecules was calculated for each sample by using coincidence counting technique by the comparison of the signals at  $m/z = 19$ , corresponding to F anion, and  $m/z = 191$ , corresponding to C<sub>8</sub>F<sub>4</sub>H<sub>3</sub>O anion, with the signal of “coincidentally emitted/detected” F and C<sub>8</sub>F<sub>4</sub>H<sub>3</sub>O anions.<sup>106</sup>

The EBL was carried out by using JEOL JSM-6460 Scanning Electron Microscope (SEM) equipped with DEBEN laser stage. The system was operated at 30 kV accelerating voltage and 10 pA beam current with series of exposure dosage ranging from 200 to 600



$\mu\text{C}/\text{cm}^2$  (corresponding to 6 to 18  $\text{mJ}/\text{cm}^2$ ). A  $5 \times 5 \mu\text{m}$  pattern with features including varied line width, i.e., 10, 20, 30, 40, 50, 60, 70, 80, 90, and 100 nm, respectively, and fixed 500 nm space was designed and used to evaluate the lithographic behavior of polymer resists.

The Atomic Force Microscopy (AFM) imaging was performed on MFP-3D system (Asylum Research) in tapping mode using standard silicon tips (VISTAprobes, T190-25, resonance constant: 190 kHz, tip radius:  $\sim 10$  nm, spring constant: 48 N/m). The Field Emission Scanning Electron Microscope (FE-SEM) images were collected with JEOL JSM-7500F using an accelerating voltage of 7 kV.

### 2.3.3. *Synthesis of macromonomer 1 (NB-PTFPHS<sub>12</sub>)*

To a 25 mL Schlenk flask equipped with a magnetic stirring bar dried with flame under  $\text{N}_2$  atmosphere, was added NB-CTA (301 mg, 0.782 mmol), TFpHS (4.49 g, 23.4 mmol), AIBN (12.7 mg, 78.2  $\mu\text{mol}$ ), and 10.5 mL of 2-butanone. The mixture was stirred 10 min at rt, deoxygenated through five cycles of freeze-pump-thaw and back-filled with  $\text{N}_2$ . After the last cycle, the reaction mixture was stirred 10 min at rt and immersed into a pre-heated oil bath at 65  $^\circ\text{C}$  to start the polymerization. After 11 h, the polymerization was quenched by cooling the reaction flask with liquid  $\text{N}_2$ . The copolymer was purified by precipitation into 300 mL of hexane twice. The pink oil was collected through centrifugation, washed with 300 mL of hexane, and kept under vacuum overnight for removing residual solvents. Yield 1.4 g of product, 60% yield based upon  $\sim 45\%$  monomer conversion.  $M_{\text{n, GPC}} = 2,750$  Da (laser detector),  $PDI = 1.07$ .  $^1\text{H}$  NMR (500 MHz,  $\text{DMSO}-d_6$ )  $\delta$  10.95–11.90 (m, phenol OHs), 7.42–7.84 (m, Ar Hs from RAFT

functionality), 6.08 (s, NB CH=CH), 5.10–5.30 (br, backbone chain end CH), 3.90–4.10 (m, NB CH<sub>2</sub>OC(O)), 1.02–3.45 (m, all CH<sub>2</sub>s and CHs from TFpHS unit backbone and NB ring). <sup>13</sup>C NMR (125 MHz, DMSO-*d*<sub>6</sub>) δ 206.9, 172.2, 145.6, 144.3, 144.1, 138.7, 137.2, 136.5, 135.0, 133.8, 129.3, 127.0, 123.2, 108.4, 73.1, 68.4, 63.0, 45.0, 43.5, 42.4, 41.5, 40.5, 38.3, 37.9, 35.8, 34.6, 34.4, 33.2, 31.4, 31.1, 29.6, 29.4, 28.9. IR (cm<sup>-1</sup>): 3720–2610, 1714, 1658, 1523, 1495, 1459, 1351, 1245, 1142, 1048, 947, 866. *T*<sub>g</sub>: 150 °C.

#### 2.3.4. Synthesis of macromonomer 2 (NB-PTFpHS<sub>10</sub>)

To a 25 mL Schlenk flask equipped with a magnetic stirring bar dried with flame under N<sub>2</sub> atmosphere, was added NB-CTA (510 mg, 1.32 mmol), TFpHS (5.06 g, 26.4 mmol), AIBN (12.9 mg, 79.2 μmol), and 12 mL of 2-butanone. The mixture was stirred 10 min at rt, deoxygenated through five cycles of freeze-pump-thaw and back-filled with N<sub>2</sub>. After the last cycle, the reaction mixture was stirred 10 min at rt and immersed into a pre-heated oil bath at 65 °C to start the polymerization. After 11 h, the polymerization was quenched by cooling the reaction flask with liquid N<sub>2</sub>. The copolymer was purified by precipitation into 300 mL of hexane twice. The pink oil was collected through centrifugation, washed with 300 mL of hexane, and kept under vacuum overnight for removing residual solvents. Yield 1.7 g of product, 61% yield based upon ~45% monomer conversion. *M*<sub>n, GPC</sub> = 2,450 Da (laser detector), *PDI* = 1.08. The <sup>1</sup>H NMR, <sup>13</sup>C NMR and IR spectra were similar as **1**. *T*<sub>g</sub>: 150 °C.

#### 2.3.5. Synthesis of macromonomer 3 (NB-P(*p*HS<sub>13</sub>-co-PhMI<sub>13</sub>))

To a 100 mL Schlenk flask equipped with a magnetic stirring bar dried with flame under N<sub>2</sub> atmosphere, was added NB-CTA (635 mg, 1.65 mmol), *p*HS (3.95 g, 33.0 mmol),

PhMI (5.76 g, 33.0 mmol), AIBN (26.7 mg, 165  $\mu$ mol) and 35 mL of anhydrous 1,4-dioxane. The mixture was stirred 10 min at rt, deoxygenated through five cycles of freeze-pump-thaw and back-filled with N<sub>2</sub>. After the last cycle, the reaction mixture was stirred 15 min at rt and immersed into a pre-heated oil bath at 65 °C to start the copolymerization. After 6.5 h, the polymerization was quenched by cooling the reaction flask with liquid N<sub>2</sub>. The copolymer was purified by precipitation into 600 mL of diethyl ether twice. The pink precipitate was collected through centrifugation, washed with 200 mL of diethyl ether and 200 mL of hexane, and kept under vacuum overnight for removing residual solvents. Yield 3.4 g of product, 60% yield based upon ~ 55% conversion for both monomers.  $M_n$ , GPC = 3,520 Da (RI detector),  $M_n$ , GPC = 6,870 Da (laser detector),  $PDI$  = 1.20. <sup>1</sup>H NMR (500 MHz, DMSO-*d*<sub>6</sub>)  $\delta$  9.20–9.80 (br, phenol OHs), 6.20–7.92 (m, Ar Hs), 6.08 (br, NB CH=CH), 5.10–5.43 (br, backbone chain end CH), 3.90–4.13 (m, NB CH<sub>2</sub>OC(O)), 0.76–3.22 (m, all CH<sub>2</sub>s and CHs from *p*HS unit backbone and NB ring, all CHs from MI units). <sup>13</sup>C NMR (125 MHz, DMSO-*d*<sub>6</sub>)  $\delta$  204.9, 176.8, 171.8, 156.7, 154.9, 136.8, 136.2, 132.0, 129.7, 129.0, 128.8, 126.8, 115.5, 114.7, 68.0, 61.9, 51.6, 44.6, 43.2, 42.2, 41.1, 37.6, 34.8, 34.6, 34.4, 33.2, 31.4, 31.1, 29.6, 29.4, 28.9. IR (cm<sup>-1</sup>): 3700–3118, 3090–2790, 1774, 1701, 1610, 1506, 1450, 1380, 1262, 1185, 845, 750.  $T_g$ : 130 °C.

#### 2.3.6. Synthesis of macromonomer **4** (NB-*P*(*p*HS<sub>8</sub>-co-PhMI<sub>8</sub>))

To a 50 mL Schlenk flask equipped with a magnetic stirring bar dried with flame under N<sub>2</sub> atmosphere, was added NB-CTA (802 mg, 2.08 mmol), *p*HS (2.50 g, 20.8 mmol), PhMI (3.60 g, 20.8 mmol), AIBN (16.9 mg, 104  $\mu$ mol) and 20 mL of anhydrous 1,4-dioxane. The mixture was stirred 10 min at rt, deoxygenated through five cycles of freeze-

pump-thaw and back-filled with N<sub>2</sub>. After the last cycle, the reaction mixture was stirred 15 min at rt and immersed into a pre-heated oil bath at 65 °C to start the copolymerization. After 4.5 h, the polymerization was quenched by cooling the reaction flask with liquid N<sub>2</sub>. The copolymer was purified by precipitation into 600 mL of diethyl ether twice. The pink precipitate was collected through centrifugation, washed with 400 mL of diethyl ether and 400 mL of hexane, and kept under vacuum overnight for removing residual solvents. Yield 2.8 g of product, 73% yield based upon ~ 60% conversion for both monomers.  $M_n$ , GPC = 2,730 Da (RI detector),  $M_n$ , GPC = 3,800 Da (laser detector),  $PDI$  = 1.12. The <sup>1</sup>H NMR, <sup>13</sup>C NMR and IR spectra were similar as **3**.  $T_g$ : 130 °C.

#### 2.3.7. Synthesis of brush **I** ((PNB-g-PTFpHS<sub>12</sub>)<sub>3</sub>-b-(PNB-g-P(pHS<sub>13</sub>-co-PhMI<sub>13</sub>)<sub>26</sub>)

To a 10 mL Schlenk flask equipped with a magnetic stirring bar dried with flame under N<sub>2</sub> atmosphere, was added the modified Grubbs catalyst (3.37 mg, 4.63 μmol) and 0.6 mL of anhydrous CH<sub>2</sub>Cl<sub>2</sub>. The mixture was stirred 1 min at rt, deoxygenated through five cycles of freeze-pump-thaw and back-filled with N<sub>2</sub>. After the last cycle, the solution of **1** (51.0 mg, 18.5 μmol) in 0.2 mL of anhydrous THF (deoxygenated through two cycles of freeze-pump-thaw) was quickly added with an airtight syringe. The reaction mixture was allowed to stir for 40 min at rt before adding the solution of **3** (584 mg, 139 μmol) in 4.3 mL of anhydrous THF/CH<sub>2</sub>Cl<sub>2</sub> (v/v = 3.8:0.5, deoxygenated through two cycles of freeze-pump-thaw) with an airtight syringe. The reaction mixture was stirred for 4 h at rt before quenching the polymerization by adding 0.6 mL of ethyl vinyl ether (EVE), and was further allowed to stirred for 1 h at rt. The solution was diluted with 5 mL of THF and precipitated into 180 mL of MeOH. The precipitate was collected through

centrifugation and re-dissolved into 20 mL of THF/acetone (v/v = 1:1). The solution was then precipitated into 200 mL of diethyl ether. The precipitate was collected through centrifugation, washed with 200 mL of diethyl ether and 200 mL of hexane, and kept under vacuum overnight for removing residual solvents. Yield 270 mg of product, 48% yield based upon ~ 80% conversion for **1** and ~ 90% conversion for **3**, respectively.  $M_{n, \text{GPC}} = 189 \text{ kDa}$  (laser detector),  $PDI = 1.25$ .  $^1\text{H}$  NMR (500 MHz,  $\text{DMSO-}d_6$ )  $\delta$  10.95–11.90 (m, phenol OHs), 9.20–9.80 (br, phenol OHs), 7.42–7.84 (m, Ar Hs from RAFT functionality), 6.20–8.20 (br, Ar Hs), 4.98–5.56 (br, brush backbone  $\text{CH}=\text{CH}$ ), 0.76–4.06 (m,  $\text{CH}_2$ s and CHs from *p*HS, TF*p*HS, and MI unit backbones and PNB backbone).  $^{13}\text{C}$  NMR (125 MHz,  $\text{DMSO-}d_6$ )  $\delta$  197.8, 177.3, 172.1, 165.0, 157.2, 132.4, 129.3, 127.3, 115.9, 51.7, 42.2, 34.8. IR ( $\text{cm}^{-1}$ ): 3000–3690, 2770–2990, 1774, 1697, 1607, 1509, 1450, 1380, 1262, 1175, 1030, 886, 841, 750.  $T_g$ : 130 and 150 °C, respectively. TGA in  $\text{N}_2$ : 330–395 °C, 12% mass loss, 395–480 °C, 60% mass loss, 28% mass remaining above 500 °C.

#### 2.3.8. Synthesis of brush **II** ((PNB-*g*-PTF*p*HS<sub>10</sub>)<sub>4</sub>-*b*-(PNB-*g*-P(*p*HS<sub>8</sub>-*co*-PhMI<sub>8</sub>)<sub>37</sub>)

To a 10 mL Schlenk flask equipped with a magnetic stirring bar dried with flame under  $\text{N}_2$  atmosphere, was added the modified Grubbs catalyst (5.25 mg, 7.21  $\mu\text{mol}$ ) and 0.45 mL of anhydrous  $\text{CH}_2\text{Cl}_2$ . The reaction mixture was stirred 1 min at rt to obtain a homogeneous solution and deoxygenated through three cycles of freeze-pump-thaw and back-filled with  $\text{N}_2$ . After the last cycle, the solution of **2** (69.7 mg, 30.3  $\mu\text{mol}$ ) in 0.65 mL of anhydrous THF (deoxygenated through three cycles of freeze-pump-thaw) was quickly added with an airtight syringe. The reaction mixture was allowed to stir for 40 min at rt before adding the solution of **4** (550 mg, 201  $\mu\text{mol}$ ) in 5.0 mL of anhydrous THF

(deoxygenated through three cycles of freeze-pump-thaw) with an airtight syringe. The reaction mixture was stirred for 3 h at rt before quenching the polymerization by adding 0.5 mL of EVE, and was further allowed to stirred for 1 h at rt. The solution was precipitated into 90 mL of diethyl ether. The precipitate was collected through centrifugation and re-dissolved into 20 mL of acetone. The solution was then precipitated into 200 mL of diethyl ether. The precipitate was collected through centrifugation, washed with 200 mL of diethyl ether and 200 mL of hexane, and kept under vacuum overnight for removing residual solvents. Yield 550 mg of product, 94% yield based upon ~ 90% conversion for **2** and ~ 95% conversion for **4**, respectively.  $M_{n, GPC} = 152$  kDa (laser detector),  $PDI = 1.26$ . The  $^1H$  NMR,  $^{13}C$  NMR and IR spectra were similar as **I**.  $T_g$ : 130 and 150 °C, respectively. TGA in  $N_2$ : 330–396 °C, 11% mass loss, 396–470 °C, 61% mass loss, 28% mass remaining above 500 °C.

#### 2.3.9. Synthesis of brush control ((PNB-*g*-P(*pHS*<sub>13</sub>-co-PhMI<sub>13</sub>)<sub>24</sub>)

To a 10 mL Schlenk flask equipped with a magnetic stirring bar dried with flame under  $N_2$  atmosphere, was added the modified Grubbs catalyst (1.04 mg, 1.43  $\mu$ mol) and 0.3 mL of anhydrous  $CH_2Cl_2$ . The reaction mixture was stirred 1 min at rt to obtain a homogeneous solution, deoxygenated through three cycles of freeze-pump-thaw, and back-filled with  $N_2$ . After the last cycle, the solution of **3** (120 mg, 28.6  $\mu$ mol) in 0.9 mL of anhydrous THF (deoxygenated through three cycles of freeze-pump-thaw) was quickly added with an airtight syringe. The reaction mixture was allowed to stir for 60 min at rt before quenching the polymerization by adding 0.3 mL of EVE, and was further allowed to stirred for 1 h at rt. The solution was precipitated into 60 mL of diethyl ether. The

precipitate was collected through centrifugation and re-dissolved into 5 mL of acetone. The solution was then precipitated into 90 mL of diethyl ether/hexane (v/v = 2:1). The precipitate was collected through centrifugation, washed with 100 mL of hexane twice, and kept under vacuum overnight for removing residual solvents. Yield 95 mg of product, 83% yield based upon ~ 95% conversion for **3**.  $M_{n, GPC} = 165$  kDa (laser detector),  $PDI = 1.16$ .  $^1H$  NMR (500 MHz,  $DMSO-d_6$ )  $\delta$  9.20–9.80 (br, phenol OHs), 7.42–7.84 (m, Ar Hs from RAFT functionality), 6.20–8.20 (br, Ar Hs), 4.98–5.56 (br, brush backbone  $CH=CH$ ), 0.76–4.06 (m,  $CH_2$ s and CHs from *p*HS, and MI unit backbones and PNB backbone).  $^{13}C$  NMR (125 MHz,  $DMSO-d_6$ )  $\delta$  197.6, 177.4, 172.0, 165.0, 157.2, 132.4, 129.3, 127.3, 115.9, 51.7, 42.2, 34.8. IR ( $cm^{-1}$ ): 2880–3690, 1775, 1694, 1613, 1596, 1515, 1499, 1452, 1381, 1174, 841, 750, 689.  $T_g$ : 130 °C.

#### 2.3.10. General procedure for the preparation of polymer thin film

The solution of polymer (brush **I** or **II**, or **linear control**) in cyclohexanone (1.0 wt%) was prepared and passed through a PTFE syringe filter (220 nm pore size) before using. The solution was applied onto UV-O<sub>3</sub> pre-treated silicon wafer (*the amount of applied polymer solution should be sufficient to cover the whole wafer surface*) and spin coated at 500 rpm for 5 seconds, followed by spinning at 3,000 rpm for 30 seconds (*200 rpm/s acceleration rate for each step*) to afford thin film with 18 to 25 nm thickness.

#### 2.3.11. General procedure for the acetone annealing of polymer thin film

The polymer film-coated silicon wafer was kept in a desiccator filled with saturated acetone atmosphere under vacuum for 20 hours. After the annealing process,

the excess solvent was removed by pumping under vacuum and the N<sub>2</sub> gas was slowly backfilled to open the desiccator.

### 2.3.12. Fluorine depth profiles of SIMS for brush II thin films

The fluorine depth profiles were expressed by using a ratio of intensities between F and CH<sub>2</sub> ions. The usage of this ratio is based upon the following facts: 1) the sputtering process damages the film *via* ion-atom collisions, leading to the subsequent diffusion of recoiled/displaced atoms toward the substrate; 2) the implantation of the Cs atoms, delivered by the Cs<sup>+</sup> beam, increases the ionization coefficients of the sputtered species as a function of the increasing surface/interface Cs concentration; 3) the equilibrium concentration of the Cs atoms cannot be reached during the time period of profiling.

The measured intensity of F ions,  $I_F^-(t)$ , can be expressed as

$$I_F^-(t) = I_0 k Y_F^o(c_F) \alpha_F(c_{Cs}) \quad (1)$$

where  $I_0$  is the Cs beam current (ions/s);  $k$  is the transmission/detection efficiency of mass spectrometer;  $Y_F^o(c_F)$  is the sputtering yield of the F atoms (number of sputtered atoms per projectile impact). The parameter  $\alpha_F(c_{Cs})$  denotes an ionization probability of F atoms. The ionization probability is a function of the concentration of Cs atoms in the topmost layer of the sputtered film,  $c_{Cs}$ . A widely accepted mechanism of the negative ionization of the sputtered atoms is the tunneling of electron from the surface into the emitted atom.<sup>107</sup> For this mechanism, the ionization probability is a function of the atom electron affinity,  $A$ , and the surface work function,  $\varphi$ :

$$\alpha_F(c_{Cs}) \approx e^{-(\varphi - A_F)/\epsilon_0} \quad (2)$$



where the parameter  $\varepsilon_o$  presents the “typical excitation energy due to atom motion”.<sup>108</sup> This parameter is independent of moderate (1–2 eV) changes in  $\varphi$  and  $A$ . ( $A_F = 3.4$  eV;  $A_{CH_2} = 0.6$  eV). Hence, the following equation is obtained:

$$\frac{\alpha_F(c_{Cs})}{\alpha_{CH_2}(c_{Cs})} = e^{(A_F - A_{CH_2})/\varepsilon_o} \quad (3)$$

The ratio in (3) does not depend on the work function,  $\varphi$ . Therefore, the variation of  $\varphi$ , stimulated by the Cs implantation, does not affect the ratio of intensities:

$$\frac{I_F^-(t)}{I_{CH_2}^-(t)} = \frac{Y_F^o(c_F)}{Y_{CH_2}^o(c_F)} e^{(A_F - A_{CH_2})/\varepsilon_o} \quad (4)$$

Additionally, to reduce the effect of accumulation of Cs, a thin film ( $\sim 5$  nm) of Pd/Pt alloy was deposited on the top of the organic film. This metal film works as “an obstacle”, in which the first transition processes of bombardment occur,<sup>109</sup> including of initial accumulation of the Cs and diffusion of the target atoms. Taking in account the procedures mentioned above, we assume that the sputtering yield is a linear function of the concentration of F and CH<sub>2</sub>. Thus, the ratio of concentrations is a linear function of the ratio of intensities:

$$\frac{c_F(t)}{c_{CH_2}(t)} = \beta \frac{I_F^-(t)}{I_{CH_2}^-(t)} \quad (5)$$

where the constant,  $\beta$ , reflected the differences between F and CH<sub>2</sub> ions, which are their electron affinities and detection efficiencies.

To rescale the time of profiling into the profile depth of Pt/Pd alloy and Si, the sputtering rates (specified in the figure captions) were used, which were computed with the SRIM 2011.08 software. The depth scale of the organic film corresponds to the film thickness,  $\sim 30$  nm, measured by AFM.

Although the actual atomic stoichiometry of the fluorinated molecular top was used for computing, the film depth obtained was underestimated (~ 12 nm, instead of the measured ~ 30 nm by AFM). The discrepancy could be induced due to the fact that the implanted Cs atoms were not included into the atomic stoichiometry of the films.

#### *2.3.13. General procedure for preparation of polymer resist thin film for EBL*

The solution of polymer:HMMM:PAG (0.75 wt%:0.15 wt%:0.10 wt%) in cyclohexanone was prepared and passed through a PTFE syringe filter (220 nm pore size) before using. The solution was applied onto UV-O<sub>3</sub> pre-treated silicon wafer (*the amount of applied solution should be sufficient to cover the whole wafer surface*) and spin coated at 500 rpm for 5 seconds, followed by spinning at 3,000 rpm for 30 seconds (*200 rpm/s acceleration rate for each step*) to afford thin film with 25 to 28 nm thickness.

#### *2.3.14. General procedure for PEB-EBL*

After electron beam “writing” with predesigned pattern, the exposed wafer was post-baked on a 90 °C hotplate for 1 min and dipped into 0.25 M tetramethylammonium hydroxide (TMAH) aqueous solution for 1 min. The wafers were rinsed with DI water and dried by N<sub>2</sub> flow.

#### *2.3.15. General procedure for “direct”-EBL*

After electron beam “writing” with predesigned pattern, the exposed wafer was directly dipped into 0.25 M TMAH<sub>(aq)</sub> solution for 30 seconds. The wafers were rinsed with DI water and dried by N<sub>2</sub> flow.

## 2.4. Conclusion

In summary, DBTs with high degrees of versatility in chemical compositions and concentric and lengthwise dimensions were synthesized by RAFT (co)polymerizations to afford well-defined macromonomers followed by sequential ROMPs via the “grafting-through” strategy. These cylindrical  $P(\text{NB-}g\text{-PTFpHS})\text{-}b\text{-}P(\text{NB-}g\text{-}P(p\text{HS-co-PhMI}))$  brushes exhibited strong tendency to align vertically within thin films on substrates. The chemically amplified negative-tone PEB-EBL resists from the DBT precursors showed higher resolution and higher sensitivity than a linear block copolymer control. The thinner cylindrical DBTs could generate narrower line widths, whereas the thicker one allowed “direct”-EBL of brush CARs without requirement of a PEB step. Therefore, this bottom-up synthetic strategy enables fine-tuning of the full dimensions to balance the properties and performance during the top-down lithographic processing. Further optimizations, including the introduction of aliphatic fluorinated caps to enhance brush vertical alignments and the incorporation of covalently-attached PAGs into molecular brush resist systems to achieve features with sub-10 nm are currently underway.

CHAPTER III

DIRECTING SELF-ASSEMBLY OF NANOSCOPIC CYLINDRICAL DIBLOCK  
BRUSH TERPOLYMERS INTO FILMS WITH DESIRED SPATIAL  
ORIENTATIONS: EXPANSION OF CHEMICAL COMPOSITION SCOPE\*

### 3.1. Introduction

Bottom-up block copolymer (BCP) lithography, *i.e.*, self-assembly of BCPs into highly ordered lamellar, cylindrical, and spherical morphologies with controlled orientations and nanoscopic dimensions, has attracted significant interest in the fabrication of microelectronic devices.<sup>21,73</sup> The morphology and orientation of block copolymer assemblies are governed by parameterized energy differences, consisting of the strain energy and the interfacial/surface energy, between the covalently-bonded immiscible block segments. Meanwhile, the consequential thermo or solvent vapor annealing of BCP films have been developed and demonstrated as additional and critical processes to direct the morphology and orientation of BCP assemblies.<sup>22,110,111</sup> Another emerging technique to guide the lateral ordering of the micro-domains of BCP assemblies over large areas is the top-down pre-patterning of substrates through graphoepitaxial<sup>26,112-115</sup> or

---

\* Reprinted with permission from “Directing Self-Assembly of Nanoscopic Cylindrical Diblock Brush Terpolymers into Films with Desired Spatial Orientations: Expansion of Chemical Composition Scope” by Sangho Cho, Fan Yang, Guorong Sun, Michael J. Eller, Corrie Clark, Emile A. Schweikert, James W. Thackeray, Peter Trefonas and Karen L. Wooley, *Macromol. Rapid Commun.* **2014**, 35(4), 437-441. Copyright 2013 WILEY-VCH Verlag GmbH & Co. KGaA, Weinheim.

chemoepitaxial<sup>27,29,116,117</sup> approaches. The graphoepitaxy exploits topographical patterns, such as weirs or posts, to guide and constrain the film, while chemoepitaxy utilizes the variation of substrate surface energy to provide selective interaction of each block of the BCPs with the different parts of the substrates.

The topology of BCPs has also been recognized as an important factor that affects the self-assembly process and resulting assemblies. Different from linear BCPs, the dendritic,<sup>118-120</sup> star,<sup>121,122</sup> hyperbranched,<sup>123</sup> and brush<sup>50,124,125</sup> polymers have less inter-chain entanglements due to their stretched conformations, which are induced by the higher steric repulsion between side chains. Therefore, the self-assembly process of non-linear copolymers is “accelerated”, which represents an attractive feature for the formation of periodical patterns over large areas. As unique non-linear polymer architecture, the molecular brush or bottle brush, consisting of a backbone polymer to which side chain grafted polymers are attached at each repeat unit, usually exhibits a cylindrical shape that is rendered by the rigid backbone structure and the strong size-exclusion effects between covalently tethered dense polymer grafts.<sup>47,48,51,52,125,126</sup> Upon assembly, the microdomain morphology is produced by the chemical composition differences of the side chains and their immiscibility with each other, while the dimensions of brush polymer is comparable to the contour length of the side chain and backbone.<sup>51</sup> Therefore, a profound control of the assembled domain sizes can be practically achieved through the recently developed “grafting through” synthetic approach that enables high degree of tunability over both concentric and lengthwise dimensions of the brush polymers.<sup>47,51,52</sup>

Inspired by these accomplishments, we developed diblock brush terpolymers (DBTs) as pre-constructed cylindrical nanoscopic objects and utilized them as novel polymer materials for negative-tone molecular-scale photoresists.<sup>127,128</sup> The DBT, composed of a segmental block of fluorinated grafts, poly(tetrafluoro *para*-hydroxy styrene)s (PTFpHSs), for substrate alignment and a crosslinkable block of poly(*para*-hydroxy styrene-*co*-*N*-phenyl maleimide) (P(*p*HS-*co*-PhMI)) reactive grafts, showed a strong tendency toward vertical alignments on a silicon wafer surface, due to the combinatorial effects of the bottle brush topology and the relatively lower surface energy of the fluoropolymer graft segments. The design principle and the synthetic modularity (*vide infra*) of these DBTs provide versatility in the composition, structure, and properties for block brush copolymer systems and make them attractive for the development of novel photoresist technologies.

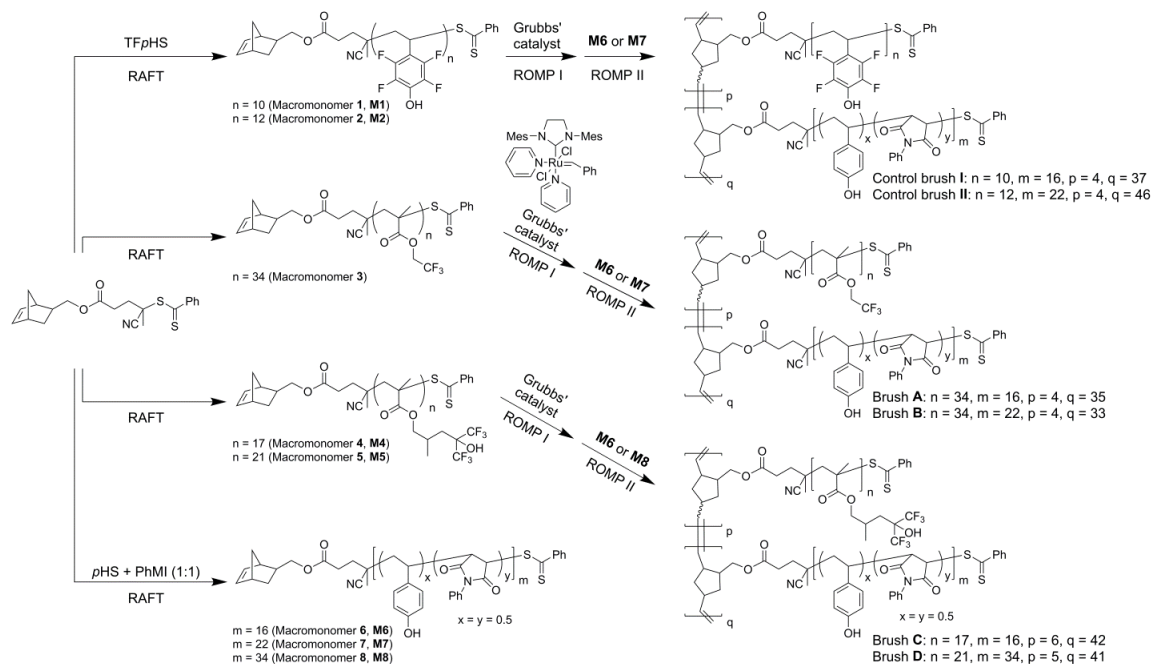
In this chapter, DBTs with densely-grafted poly(fluoro methacrylates) and P(*p*HS-*co*-PhMI) block segments have been synthesized with variations of the overall and relative lengths of the grafts *versus* the backbones. Meanwhile, the individual and collective effects of composition, fluorine content, block length, and block length ratio of the structural components of the DBTs to the vertical alignment have been studied. The introduction of fluoro methacrylates to the DBT system is highly desirable because (1) these monomers are commercially available at reasonable costs; (2) the shelf life of previous norbornenyl-terminated poly(tetrafluoro *para*-hydroxy styrene) (NB-PTFpHS) macromonomers is restricted due to the fact that 50% of the norbornenyl alkenes “disappeared” after 6 months of storage, as confirmed by <sup>1</sup>H NMR analyses (the integral

ratio between the NB alkenyl protons with the phenyl protons of the dithioester chain transfer agent (CTA) underwent reduction from 2:5 to 1:5). Although the mechanism behind this time-dependent reaction is not clear at the current stage, we speculate that electrophilic additions across the NB double bond might occur with the presence of the relatively acidic phenol protons from TFpHSs; (3) the fluoroalkyl groups usually exhibit relatively lower surface energy, compared with fluoroaromatic groups, which might further enhance the vertical alignments of DBTs on substrates.

### **3.2. Results and Discussion**

The DBTs were synthesized through a well-established and modular “grafting through” synthetic approach. In this strategy, norbornenyl-functionalized CTAs were utilized in reversible addition-fragmentation chain transfer (RAFT) controlled radical (co)polymerizations to generate macromonomers (**M**s). Sequential ring-opening metathesis polymerizations (ROMPs) of the **M**s were then carried out to complete the syntheses and afford diblock molecular brushes (Scheme 3.1).

### Scheme 3.1. Syntheses of the diblock brush terpolymers



Applying the RAFT polymerizations, well-defined NB-poly(2,2,2-trifluoroethyl methacrylate) and NB-poly(1,1,1-trifluoro-2-(trifluoromethyl)-2-hydroxy-4-methyl-5-pentyl methacrylate)s, *i.e.*, NB-PTFEMA<sub>34</sub> (**M3**), NB-PBTFHMBMA<sub>17</sub> (**M4**), and NB-PBTFHMBMA<sub>21</sub> (**M5**), respectively, were prepared (Scheme 3.1), with narrow molecular weight distributions (polydispersity indices, PDIs, <1.15, as determined by gel permeation chromatography, GPC). The well-defined structures of these macromonomers were verified by <sup>1</sup>H NMR chain-end analyses (Figure 3.1), which showed the correct integral ratios of NB alkenyl protons and RAFT agent phenyl protons as 2:5. All three NB-poly(fluoro methacrylate)s exhibited long shelf-lives with no significant decrease in NB functionality, as confirmed by <sup>1</sup>H NMR, after 6 months of storage at ambient temperature.



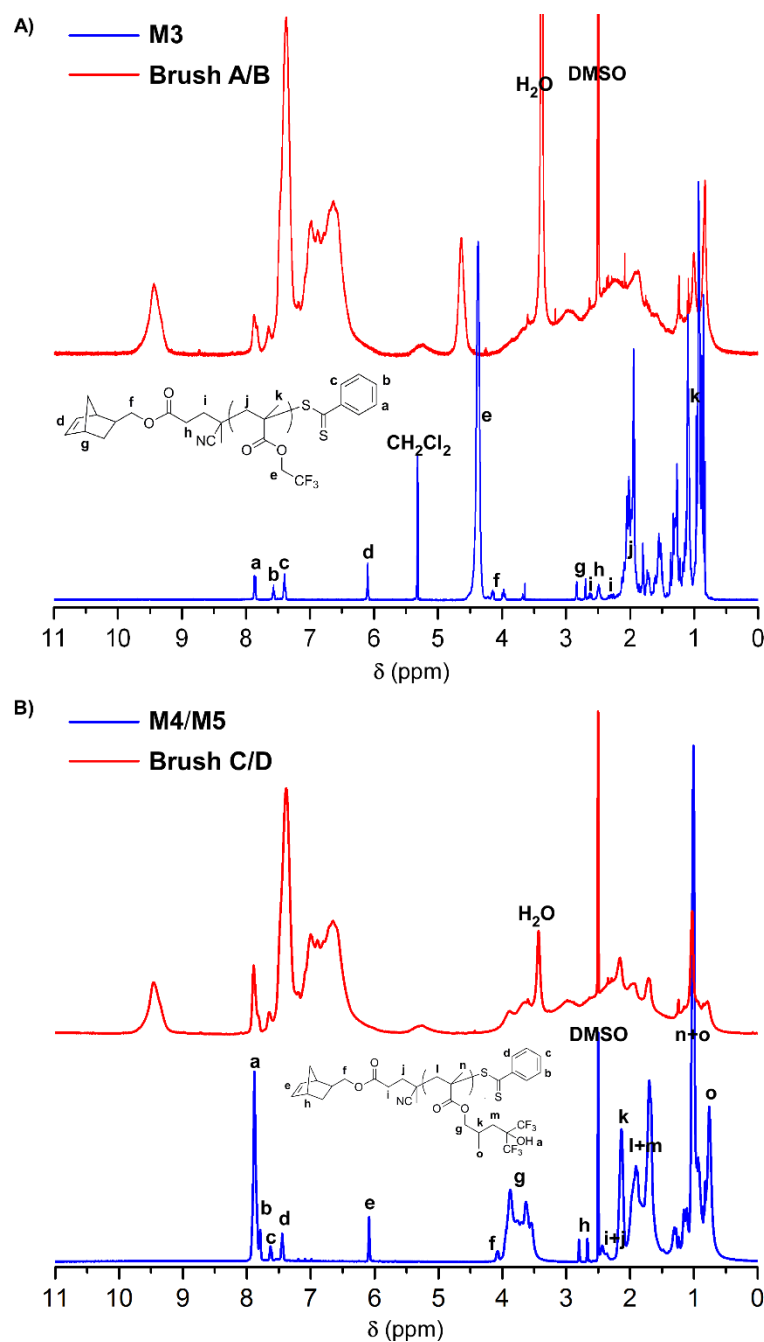


**Figure 3.1.** (a) The <sup>1</sup>H NMR spectra for **M3** (500 MHz, CD<sub>2</sub>Cl<sub>2</sub>) and brush **A/B** (500 MHz, DMSO-*d*<sub>6</sub>). (b) The <sup>1</sup>H NMR spectra for **M4/5** (500 MHz, DMSO-*d*<sub>6</sub>) and brush **C/D** (500 MHz, DMSO-*d*<sub>6</sub>). The blue profiles were from macromonomers and the red profiles were from brushes.

It is noteworthy that the measured molecular weight of resulting PTFEMA macromonomer was *ca.* twice that of the theoretical value calculated from monomer conversion. We found that *ca.* only 50% of the CTA was actually involved in the polymerization, with *ca.* 50% recovered as unreacted CTA, attributed to a slower chain transfer rate in the RAFT process, when compared to the propagation rate of TFEMA monomer. However, the atypical CTA conversion did not affect the quality of **M3**, as evidenced by the fact that GPC analysis of the ROMP of **M3** revealed that over 95% conversion of the macromonomers was reached within 30 min (Figure 3.2). The sequential ROMPs of **M3**, **M4**, and **M5** with NB-P(*p*HS-*co*-PhMI)s (**M6–8**) proceeded smoothly and resulted in four DBTs with monomodal molecular weight distributions (brush **A–D**, possessed number-averaged molecular weights from GPC,  $M_n^{\text{GPC}} = 189$  kDa, 217 kDa, 196 kDa, and 403 kDa, respectively, PDIs <1.30). As a note, the two controls, P(NB-*g*-PTF*p*HS)-*b*-P(NB-*g*-P(*p*HS-*co*-PhMI)) DBTs, (**I** and **II** in Scheme 3.1), were synthesized by following our previous report.<sup>127</sup>

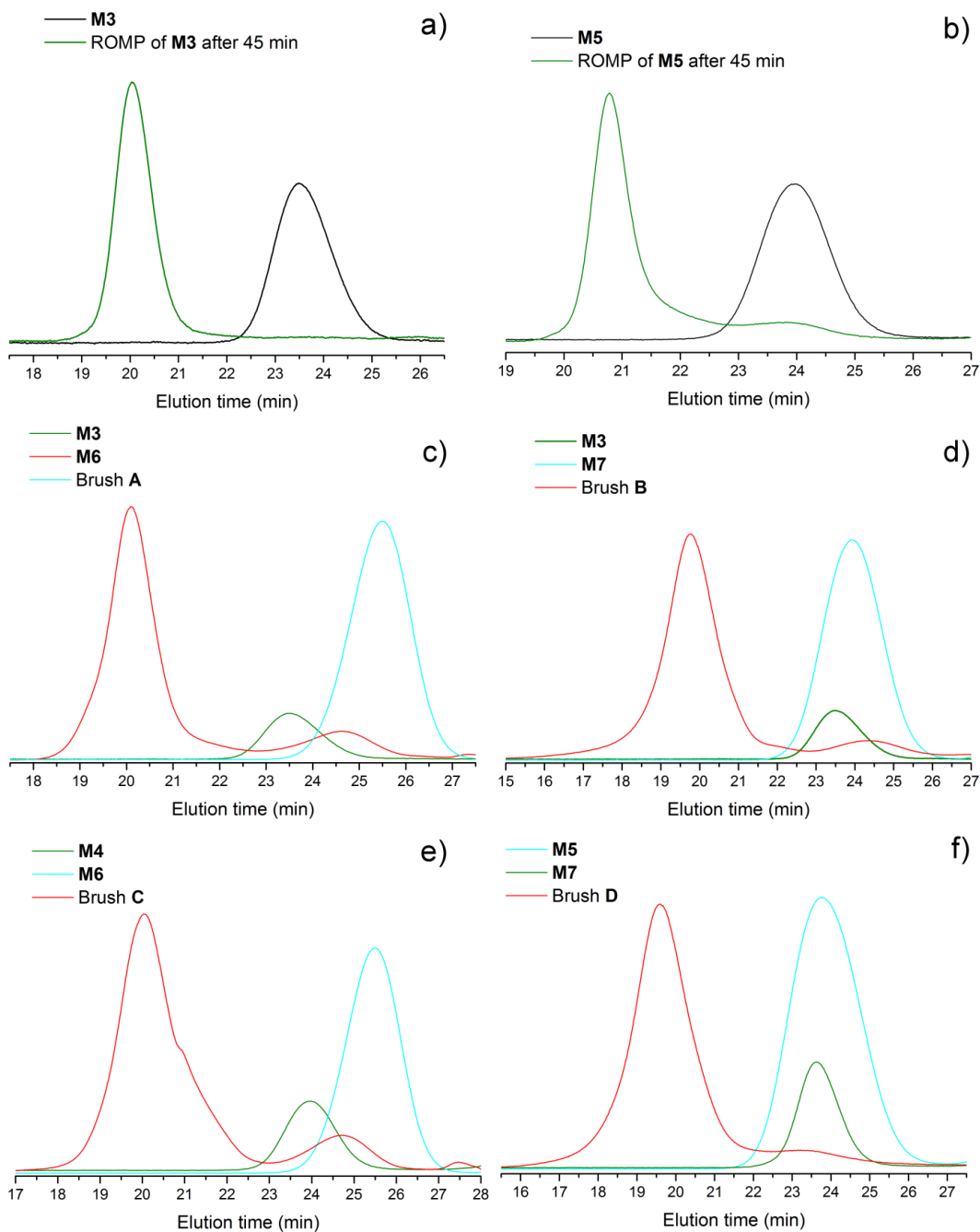


**Figure 3.2.** (a, b) The GPC profile of the ROMP for **M3** (a) and **M5** (b), respectively. (c-f) The GPC profile of the sequential ROMP for preparation of brush **A** (c), **B** (d), **C** (e), and **D** (f), respectively.

Polymer thin films were prepared by spin-casting 1.0 wt% solutions of brush polymers in cyclohexanone onto UV-O<sub>3</sub>-treated silicon wafers. To assist self-assembly, the thin films were annealed under saturated acetone vapor<sup>33</sup> for 24 h. The film thicknesses, as measured by atomic force microscopy (AFM), agreed with the estimated lengths of the extended brush backbones for all brush polymers (control **I–II** and **A–D**, Table 3.1), which indicated monolayer films. All spin-cast polymer films exhibited sufficiently homogeneous surface topographies (Figure 3.3 and 3.4) with height root-mean-square (RMS) roughnesses <0.2 nm. After acetone-annealing, the films composed of **I**, **II** and **B** maintained their surface homogeneity (Figures 3.5 and 3.6). In the higher fluorine content **A** and **C** films, irregular pores at the hundreds-of-nanometer scale (Figures 3.5 and 3.6) and increased RMS roughnesses (>0.6 nm) were observed. The microphase segregations for **A** and **C** after annealing could be attributed to their relatively longer poly(fluoro methacrylate) grafts ( $n/m = 2.125$  and  $1.063$ , respectively), compared with **I** ( $n/m = 0.625$ ). The lengthened PTFEMA and PBTFHMBMA side chains tend to “spread” over the P(NB-*g*-P(*p*HS-*co*-PhMI)) columns and to promote the formation of nanoscopic pores within the films during solvent vapor annealing process.<sup>33</sup> The energetic favor for film pores opening could be compensated through prolonging the chain length of P(*p*HS-*co*-PhMI) grafts, *e.g.*, brush **B**, which not only increased the association energy between adjacent brushes, but also enhanced the attractive interaction of brush with substrate (*vide infra*). As a note, the chemical composition of fluorinated block is still the main factor that dictates the mobility of swollen DBT as the improved interdigitation and

adhesion of P(NB-*g*-P(*p*HS-*co*-PhMI)) blocks in **D** ( $n/m = 0.618$ , a comparable value to **I**) could not provide sufficient “resistance” for acetone vapor.

**Table 3.1.** Summary of the DBT thin film characterization data.

Polymer Films	Th <sup>a</sup> [nm]	Th <sub>theo.</sub> <sup>b</sup> [nm]	R <sup>c</sup> [nm]	$\gamma^d$ [mJ m <sup>-2</sup> ]	[F] <sup>e</sup> [wt%]	A <sub>XPS</sub> <sup>f</sup> [%]	C <sub>SIMS</sub> <sup>g</sup> [%]
Control brush <b>I</b>	29 ± 1	24.5	0.2	58.4	2.00	51.5	74
Control brush <b>II</b>	25 ± 1	29.9	0.1	47.1	1.30	76.6	85
Brush <b>A</b>	22 ± 2	23.3	0.2	25.7	4.10	64.0	70
Brush <b>B</b>	21 ± 1	22.1	0.2	27.4	3.57	75.9	83
Brush <b>C</b>	23 ± 2	28.7	0.1	34.3	5.93	51.2	79
Brush <b>D</b>	25 ± 1	27.5	0.2	36.4	2.97	54.7	75

<sup>a</sup> Thickness of the spin-casted films from 1.0 wt% of polymer solutions in cyclohexanone;

<sup>b</sup> Calculated thickness of the films in monolayer based on the contour length of the brush polymers; <sup>c</sup> Height root-mean-square roughness of the films; <sup>d</sup> Surface free energy of the spin-cast films (see Table 3.3 for details); <sup>e</sup> F concentration in brush polymers. [F] = the atomic mass of F in the brush relative to atomic mass of brush ( $M_n^{GPC}$ ); <sup>f</sup> Percentage of vertical alignment within the films as spin-casted, calculated based upon the relative surface F contents from XPS (see Table 3.2 for details); <sup>g</sup> Surface coverage<sup>105</sup> by SIMS: percentage of co-emitted F-containing ions from nano-domains of spin-cast films.

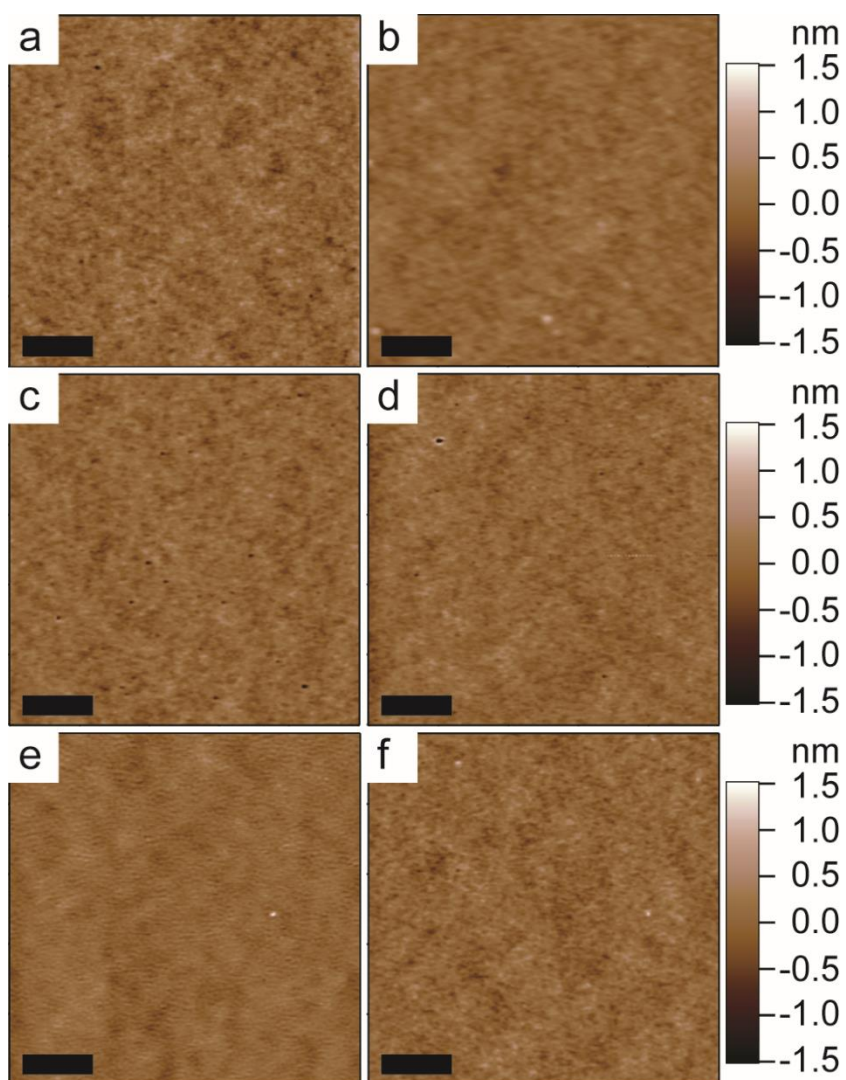


**Figure 3.3.** Tapping-mode AFM height images of as-spun thin films of brushes. (a) control brush **I**, (b) control brush **II**, (c) brush **A**, (d) brush **B**, (e) brush **C**, (f) brush **D**. Scale bars: 1  $\mu\text{m}$ .

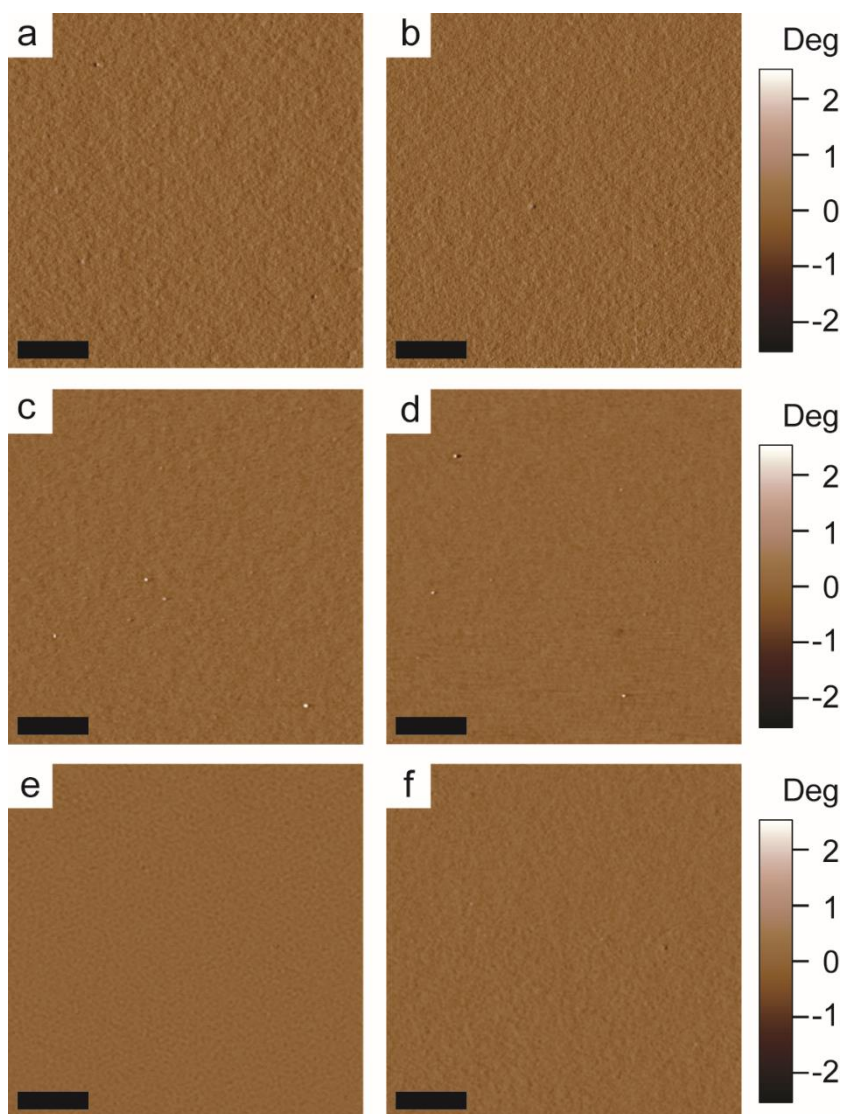


**Figure 3.4.** Tapping-mode AFM phase images of as-spun thin films of brushes. (a) control brush **I**, (b) control brush **II**, (c) brush **A**, (d) brush **B**, (e) brush **C**, (f) brush **D**. Scale bars: 1  $\mu\text{m}$ .

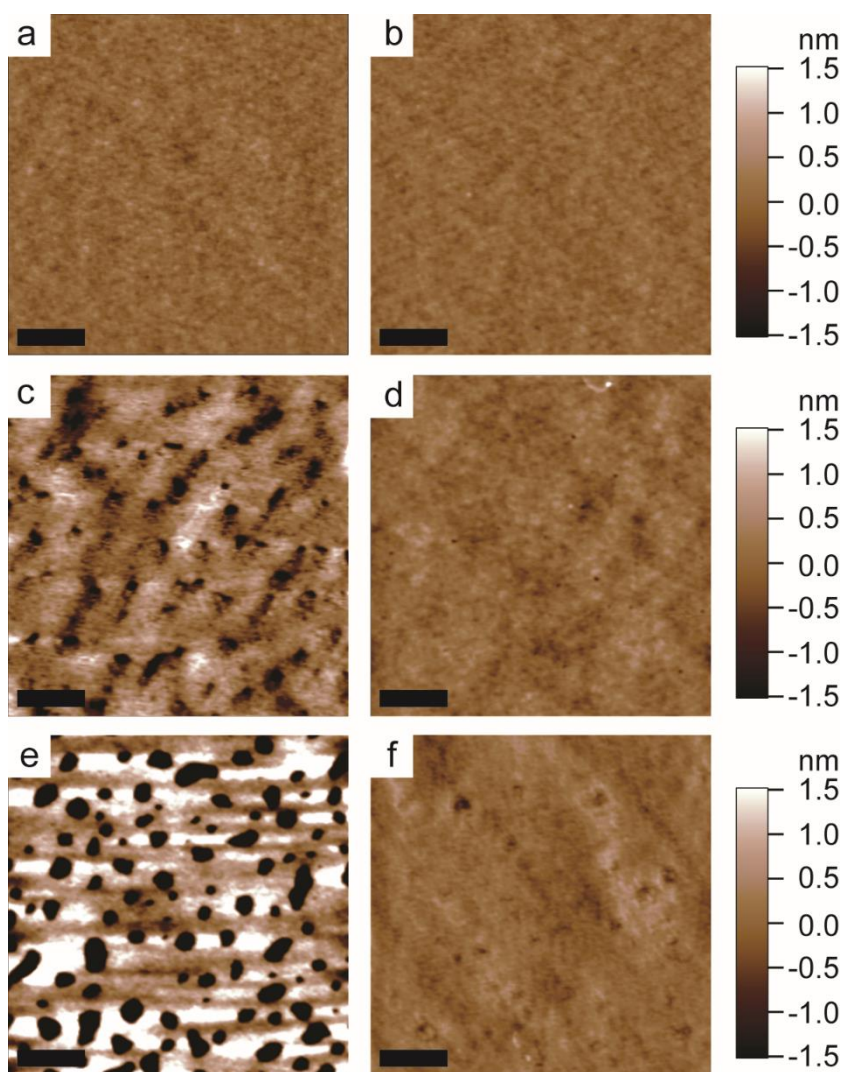


**Figure 3.5.** Tapping-mode AFM height images of acetone-annealed thin films of brushes. (a) control brush **I**, (b) control brush **II**, (c) brush **A**, (d) brush **B**, (e) brush **C**, (f) brush **D**. Scale bars: 1  $\mu\text{m}$ .



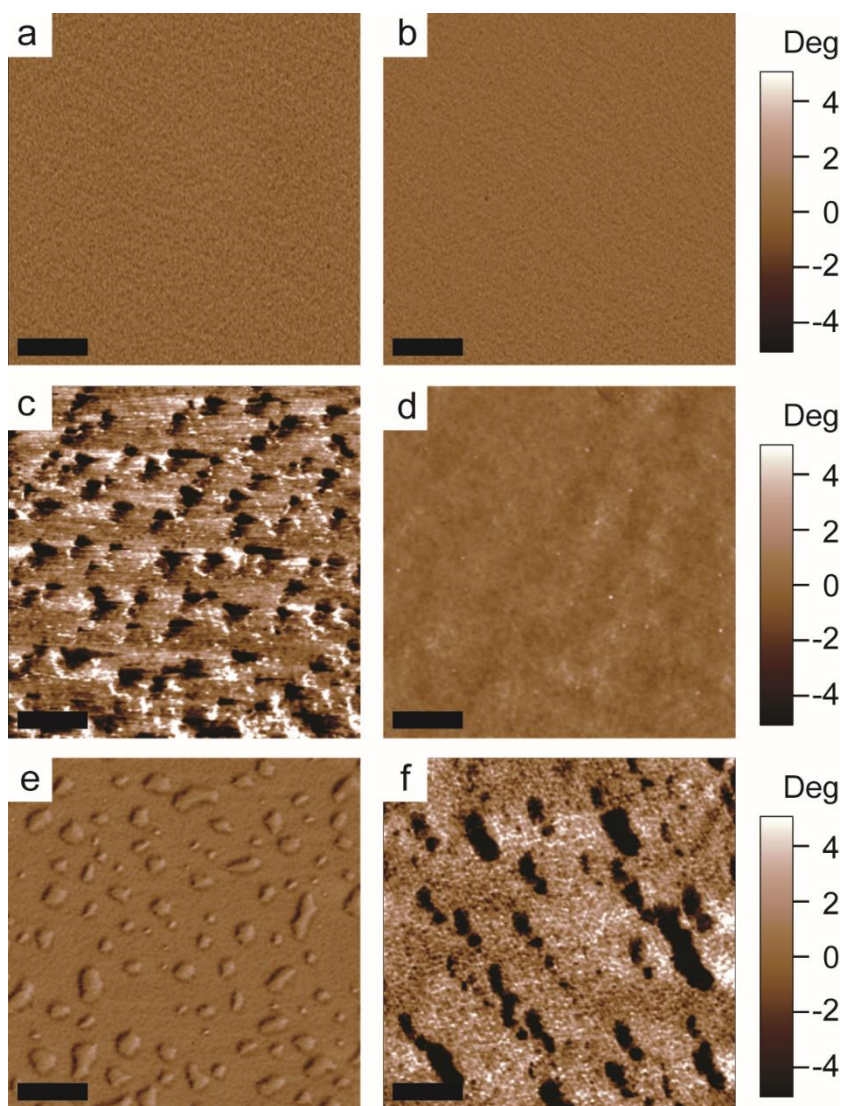


**Figure 3.6.** Tapping-mode AFM phase images of acetone-annealed thin films of brushes. (a) control brush **I**, (b) control brush **II**, (c) brush **A**, (d) brush **B**, (e) brush **C**, (f) brush **D**. Scale bars: 1  $\mu\text{m}$ .

The vertical alignments of brushes on the wafer surface were confirmed by X-ray photoelectron spectroscopy (XPS), secondary ion mass spectrometry (SIMS),<sup>105</sup> and contact angle analyses (Table 3.1–3.3). The intrinsic cylindrical topology of DBT provides an opportunity for perpendicular orientation to the substrate, which is driven by a combination of the surface energy-determined migration of the fluorinated block segment towards the film-air interface, and an attraction of the P(*p*HS-*co*-PhMI) grafts toward the substrate. By XPS, the introduction of a PTFEMA<sub>34</sub>-based fluorinated cap to DBT **A** improved its vertical alignment when compared with control **I**, which was expected given the 105% increase in fluorine content. However, further increase in fluorine content, *i.e.*, the P(NB-*g*-PBTFHMBMA<sub>17</sub>)<sub>6</sub> block in **C**, did not provide noticeable improvement on the extent of brush vertical alignment on the substrate. In our previous lithographic studies, the concentric and lengthwise dimensions of the substrate-attractive P(NB-*g*-P(*p*HS-*co*-PhMI)<sub>m</sub>)<sub>q</sub> block segments, which regulate the inclusive shape of DBTs, were found to be critical parameters that determined the features of latent patterns.<sup>127,128</sup> While “thinner” columns with smaller *m* and larger *q* values have shown advantages on resolving small pattern features, the “wider” **II**, **B**, and **D** with relatively lower fluorine contents showed higher degrees of vertical alignments for all of the three surveyed fluorinated caps, due to the larger substrate-contact areas and enhanced brush-substrate interactions.

**Table 3.2.** Relative ratios of elements in polymer films surface from XPS measurements.

		C1s@285 eV	O1s@532 eV	F1s@688 eV
		[%]	[%]	[%]
Control	Spin-cast	86.2	11.1	2.8
	Acetone-annealed	83.8	11.1	5.0
	Brush <b>I</b>			
	Random distributed	84.8	13.2	2.1
	Ideally vertical aligned <sup>a</sup>	82.3	12.6	5.2
Control	Spin-cast	82.8	12.7	4.5
	Acetone-annealed	80.3	14.4	5.3
	Brush <b>II</b>			
	Random distributed	85.0	13.4	1.6
	Ideally vertical aligned <sup>a</sup>	81.4	12.6	5.9
Control	Spin-cast	80.0	13.6	6.4
	Acetone-annealed	70.6	15.0	14.5
	Brush <b>A</b>			
	Random distributed	80.7	14.4	4.9
	Ideally vertical aligned <sup>a</sup>	74.8	15.2	10.0
Control	Spin-cast	81.7	13.5	6.3
	Acetone-annealed	79.0	14.4	6.7
	Brush <b>B</b>			
	Random distributed	81.5	14.4	4.1
	Ideally vertical aligned <sup>a</sup>	76.6	15.0	8.3
Control	Spin-cast	78.9	13.8	7.3
	Acetone-annealed	70.0	13.7	16.4
	Brush <b>C</b>			
	Random distributed	80.2	13.8	6.0
	Ideally vertical aligned <sup>a</sup>	71.6	14.1	14.3
Control	Spin-cast	81.9	13.0	5.1
	Acetone-annealed	76.8	13.2	10.0
	Brush <b>D</b>			
	Random distributed	82.4	14.0	3.5
	Ideally vertical aligned <sup>a</sup>	76.5	14.2	9.3

<sup>a</sup> The relative ratio of elements in ideally vertical aligned film is calculated based on the depth up to 10 nm from the film surface.

**Table 3.3.** Summary of static contact angles and surface free energies of polymer films.

		Static contact angle [°]		Surface free energy [mJ m <sup>-2</sup> ]
		Water	Diiodomethane	
Control	Spin-cast	57 ± 2	24 ± 1	58.4
Brush <b>I</b>	Acetone-annealed	73 ± 1	37 ± 1	47.1
Control	Spin-cast	73 ± 2	36 ± 2	47.1
Brush <b>II</b>	Acetone-annealed	74 ± 2	36 ± 1	47.0
Brush <b>A</b>	Spin-cast	95 ± 1	69 ± 1	25.7
	Acetone-annealed	97 ± 2	74 ± 2	22.8
Brush <b>B</b>	Spin-cast	93 ± 1	67 ± 1	27.4
	Acetone-annealed	91 ± 1	68 ± 2	27.1
Brush <b>C</b>	Spin-cast	75 ± 1	68 ± 1	34.3
	Acetone-annealed	79 ± 1	69 ± 1	31.9
Brush <b>D</b>	Spin-cast	73 ± 1	65 ± 2	36.4
	Acetone-annealed	80 ± 1	69 ± 1	31.5

### 3.3. Experimental Section

#### 3.3.1. Materials

The modified Grubbs catalyst,<sup>89</sup> 4-hydroxystyrene (*p*HS),<sup>101</sup> 2,3,5,6-tetrafluoro-4-hydroxystyrene (TF*p*HS),<sup>102</sup> NB-CTA,<sup>103</sup> macromonomers **1**, **2**, and **6–8**,<sup>127</sup> and control brushes **I** and **II**<sup>127</sup> were synthesized according to the literature reports. The 2,2,2-trifluoroethyl methacrylate (TFEMA) was purchased from Aldrich and purified by passing through a neutral alumina column to remove the inhibitor. The 1,1,1-trifluoro-2-(trifluoromethyl)-2-hydroxy-4-methyl-5-pentyl methacrylate (BTFHMBMA) was purchased from Aldrich and used without further purification. Other chemicals were purchased from Aldrich, Acros, and VWR and were used without further purification unless otherwise noted. Prior to use, tetrahydrofuran (THF) was distilled over sodium and stored under N<sub>2</sub>. Dichloromethane (CH<sub>2</sub>Cl<sub>2</sub>) was distilled over calcium hydride and stored under N<sub>2</sub>.

### 3.3.2. Instruments

$^1\text{H}$  and  $^{13}\text{C}$  NMR spectra were recorded on a Varian 500 MHz spectrometer interfaced to a LINUX computer using VNMR-J software. Chemical shifts were referred to the solvent proton resonance.

The polymer molecular weight and molecular weight distribution were determined by Gel Permeation Chromatography (GPC). The GPC was conducted on a Waters 1515 HPLC (Waters Chromatography, Inc.) equipped with a Waters 2414 differential refractometer, a PD2020 dual-angle ( $15^\circ$  and  $90^\circ$ ) light scattering detector (Precision Detectors, Inc.), and a three-column series (PL gel  $5\mu\text{m}$  Mixed C,  $500\text{ \AA}$ , and  $10^4\text{ \AA}$ ,  $300 \times 7.5\text{ mm}$  columns; Polymer Laboratories, Inc.). The system was equilibrated at  $40^\circ\text{C}$  in THF, which served as the polymer solvent and eluent with a flow rate of  $1.0\text{ mL/min}$ . Polymer solutions were prepared at a known concentration ( $3\text{--}5\text{ mg/mL}$ ) and an injection volume of  $200\text{ }\mu\text{L}$  was used. Data collection and analysis were performed with Precision Acquire software and Discovery 32 software (Precision Detectors, Inc.), respectively. Inter-detector delay volume and the light scattering detector calibration constant were determined by calibration using a nearly monodispersed polystyrene standard (Polymer Laboratories,  $M_p = 90\text{ kDa}$ ,  $M_w/M_n < 1.04$ ). The differential refractometer was calibrated with standard polystyrene reference material (SRM 706 NIST), of known specific refractive index increment  $dn/dc$  ( $0.184\text{ mL/g}$ ). The  $dn/dc$  values of the analyzed polymers were then determined from the differential refractometer response.

The glass transition temperatures ( $T_g$ ) were measured by differential scanning calorimetry on a Mettler-Toledo DSC822 (Mettler-Toledo, Inc., Columbus, OH), with a

heating rate of 10 °C/min. The measurements were analyzed by using Mettler-Toledo STARE software. The  $T_g$  was taken as the midpoint of the inflection tangent, upon the third heating scan. Thermogravimetric analysis (TGA) was performed under N<sub>2</sub> atmosphere using a Mettler-Toledo model TGA/SDTA851, with a heating rate of 5 °C/min. The measurements were analyzed by using Mettler-Toledo STARE software.

The surface energy of the film was calculated with Owens–Wendt–Rabel–Kaelble (OWRK) method after measuring the contact angle with optical tensiometer (KSV Instruments, Attension Theta). The X-ray Photoelectron Spectroscopy (XPS) experiments were performed on a Kratos Axis Ultra XPS system with a monochromatic aluminum X-ray source (10 mA, 12 kV). The binding energy scale was calibrated to 285 eV for the main C1s peak.

The Secondary Ion Mass Spectrometry (SIMS) measurements were carried out with a custom-built SIMS instrument coupled to a time-of-flight (TOF) mass analyzer.<sup>129</sup> The instrument used in these studies is equipped with a Au liquid metal ion source (Au-LMIS) capable of producing Au<sub>400</sub><sup>4+</sup> projectiles with total impact energy of 520 keV. The SIMS analysis of the polymer samples was conducted in the superstatic regime, where less than 0.1% of the surface is impacted. This restriction ensured that each time the surface was impacted by a primary ion, an unperturbed area of the surface was sampled. The superstatic measurements were conducted in the event-by-event bombardment-detection mode, where a single primary ion impacted on the surface and the secondary ions were collected and analyzed prior to subsequent primary ions impacting the surface. The event-by-event bombardment mode enables quantitative surface analysis without

external standardization.<sup>106,130</sup> Coincidence mass spectra, *i.e.*, spectra showing ions co-emitted with a specific secondary ion of interest were extracted from the records of the individual impacts. All secondary ions detected in a single impact originated from a 10 nm radius on the surface.<sup>105</sup>

Each polymer sample was measured three times at different locations on the sample by TOF-SIMS. Each measurement consisted of  $\sim 4 \times 10^6$  projectile impacts on an area  $\sim 250\text{--}500$   $\mu\text{m}$  in radius. Multiple measurements were performed to ensure sample consistency. A quantitative estimate of surface coverage of fluorine containing molecules was calculated for each sample by using coincidence counting technique by the comparison of the signals at  $m/z = 19$ , corresponding to  $\text{F}^-$ ,  $m/z = 69$ , corresponding to  $\text{CF}_3^-$ ,  $m/z = 99$ , corresponding to  $\text{CF}_3\text{CH}_2\text{O}^-$ ,  $m/z = 167$ , corresponding to  $\text{C}_2\text{F}_6\text{CHO}^-$ ,  $m/z = 191$ , corresponding to  $\text{C}_8\text{F}_4\text{H}_3\text{O}^-$ , and  $m/z = 239$ , corresponding to  $\text{C}_2\text{F}_6\text{OC}_5\text{H}_9\text{O}^-$ , with the signal of “coincidentally emitted/detected” anions.<sup>106</sup>

The Atomic Force Microscopy (AFM) imaging was performed on MFP-3D system (Asylum Research) in tapping mode using standard silicon tips (VISTAprobes, T190-25, resonance constant: 190 kHz, tip radius:  $\sim 10$  nm, spring constant: 48 N/m).

### 3.3.3. Synthesis of macromonomer 3 (**M3**, NB-PTFEMA<sub>34</sub>)

To a 25 mL Schlenk flask equipped with a magnetic stirring bar dried with flame under  $\text{N}_2$  atmosphere, was added NB-CTA (151 mg, 0.390 mmol), TFEMA (2.62 g, 15.6 mmol), AIBN (3.17 mg, 19.5  $\mu\text{mol}$ ) and 5 mL of anhydrous 1,4-dioxane. The mixture was stirred 5 min at rt, deoxygenated through three cycles of freeze-pump-thaw and back-filled with  $\text{N}_2$ . After the last cycle, the reaction mixture was stirred 10 min at rt and

immersed into a pre-heated oil bath at 63 °C to start the copolymerization. After 10 h, the polymerization was quenched by cooling the reaction flask with liquid N<sub>2</sub>. The copolymer was purified by precipitation into 150 mL of hexane twice. The pink precipitate was collected through centrifugation, washed with 150 mL of hexane, and kept under vacuum overnight for removing residual solvents. Yield 1.0 g of product, 68% yield based upon ~ 50% conversion for both monomer and NB-CTA.  $M_{n, GPC}$  = 6,050 Da (RI detector),  $M_{n, NMR}$  = 6,100 Da, PDI = 1.13. <sup>1</sup>H NMR (500 MHz, CD<sub>2</sub>Cl<sub>2</sub>) δ 7.38–7.88 (m, Ar *H*s), 6.10 (br, NB *CH=CH*), 4.28–4.50 (br, TFEMA OCH<sub>2</sub>CF<sub>3</sub>), 3.94–4.18 (m, NB CH<sub>2</sub>OC(O)), 2.81–2.85 and 2.68–2.71 (m, NB allylic *H*s), 0.76–2.65 (m, all CH<sub>3</sub>s, CH<sub>2</sub>s and CHs from TFEMA unit backbone, NB ring, and CTA). <sup>13</sup>C NMR (125 MHz, CD<sub>2</sub>Cl<sub>2</sub>) δ 175.9, 175.6, 175.3, 174.9, 174.7, 171.9, 170.3, 170.1, 144.6, 136.9, 136.1, 132.9, 128.4, 126.5, 124.2, 121.9, 119.7, 68.8, 61.2, 60.9, 52.0, 45.0, 44.7, 43.6, 41.6, 37.9, 36.1, 34.6, 34.1, 29.6, 29.4, 29.0, 25.2, 18.4, 16.6, 11.2. *T*<sub>g</sub>: 135 °C.

#### 3.3.4. Synthesis of macromonomer 4 (**M4**, NB-PBTFHMBMA<sub>17</sub>)

To a 25 mL Schlenk flask equipped with a magnetic stirring bar dried with flame under N<sub>2</sub> atmosphere, was added NB-CTA (204 mg, 53.0 μmol), BTFHMBMA (4.93 g, 16.0 mmol), AIBN (12.9 mg, 79.6 μmol), and 8 mL of 2-butanone. The mixture was stirred 10 min at rt, deoxygenated through four cycles of freeze-pump-thaw and back-filled with N<sub>2</sub>. After the last cycle, the reaction mixture was stirred 10 min at rt and immersed into a pre-heated oil bath at 65 °C to start the polymerization. After 7.5 h, the polymerization was quenched by cooling the reaction flask with liquid N<sub>2</sub>. The polymer was purified by precipitation into 150 mL of cold hexane (~ -10 °C) twice. The precipitate



was collected through centrifugation, washed with 100 mL of hexane, and kept under vacuum overnight for removing residual solvents. Yield 1.6 g of product, 65% yield based upon ~ 45% conversion of BTFHMBMA.  $M_{n, GPC} = 5,100$  Da (RI detector), PDI = 1.08.  $M_{n, NMR} = 5,650$  Da.  $^1H$  NMR (500 MHz,  $DMSO-d_6$ ,  $\delta$ ) 7.40–8.00 (m, Ar  $H$ s from RAFT functionality and  $HOC(CF_3)_2$ ), 6.09 (br, NB  $CH=CH$ ), 3.39–4.12 (m, NB  $CH_2OC(O)$  and BTFHMBMA  $CH_2OC(O)$ ), 2.63–2.83 (m, NB allylic  $H$ s), 0.54–2.83 (m, all  $CH$ s,  $CH_2$ s and  $CH_3$ s from CTA, NB ring and BTFHMBMA units).  $^{13}C$  NMR (125 MHz,  $DMSO-d_6$ )  $\delta$  177.1, 176.1, 172.2, 171.3, 144.6, 137.2, 136.5, 133.4, 129.1, 127.3, 126.5, 124.1, 122.7, 122.2, 120.4, 76.1, 69.9, 68.4, 62.4, 59.1, 54.7, 54.2, 52.5, 44.9, 44.7, 44.4, 43.5, 41.5, 38.0, 33.3, 29.6, 27.3, 18.7, 18.0, 16.1, 15.8, 11.7.  $T_g$ : 130 °C.

### 3.3.5. Synthesis of macromonomer 5 (**M5**, NB-PBTFHMBMA<sub>21</sub>)

To a 25 mL Schlenk flask equipped with a magnetic stirring bar dried with flame under  $N_2$  atmosphere, was added NB-CTA (171 mg, 444  $\mu$ mol), BTFHMBMA (4.02 g, 13.1 mmol), AIBN (10.5 mg, 65.0  $\mu$ mol), and 12 mL of 2-butanone. The mixture was stirred 5 min at rt, deoxygenated through five cycles of freeze-pump-thaw and back-filled with  $N_2$ . After the last cycle, the reaction mixture was stirred 10 min at rt and immersed into a pre-heated oil bath at 65 °C to start the polymerization. After 7.5 h, the polymerization was quenched by cooling the reaction flask with liquid  $N_2$ . The copolymer was purified by precipitation into 200 mL of cold hexane at 0 °C twice. The pink solid was collected through centrifugation, washed with 200 mL of hexane, and kept under vacuum overnight for removing residual solvents. Yield 1.6 g of product, 57% yield based

upon ~65% monomer conversion.  $M_{n, \text{GPC}} = 7,450$  Da (RI detector), PDI = 1.07.  $M_{n, \text{NMR}} = 6,850$  Da. The  $^1\text{H}$  and  $^{13}\text{C}$  NMR spectra were similar as **M4**.

### 3.3.6. Synthesis of brush A ( $P(\text{NB-g-PTFEMA}_{34})_4\text{-b-}P(\text{NB-g-}P(\text{pHS}_8\text{-co-PhMI}_8))_{35}$ )

To a 10 mL Schlenk flask equipped with a magnetic stirring bar dried with flame under  $\text{N}_2$  atmosphere, was added the modified Grubbs catalyst (2.64 mg, 3.63  $\mu\text{mol}$ ) and 0.4 mL of anhydrous  $\text{CH}_2\text{Cl}_2$ . The reaction mixture was stirred 1 min at rt to obtain a homogeneous solution and deoxygenated through three cycles of freeze-pump-thaw and back-filled with  $\text{N}_2$ . After the last cycle, the solution of **M3** (87.3 mg, 14.5  $\mu\text{mol}$ ) in 0.6 mL of anhydrous  $\text{CH}_2\text{Cl}_2$  (deoxygenated through three cycles of freeze-pump-thaw) was quickly added with an airtight syringe. The reaction mixture was allowed to stir for 35 min at rt before adding the solution of **M6** (275 mg, 101  $\mu\text{mol}$ ) in 2.2 mL of anhydrous THF (deoxygenated through three cycles of freeze-pump-thaw) with an airtight syringe. The reaction mixture was stirred for 3.5 h at rt before quenching the polymerization by adding 0.3 mL of EVE, and was further allowed to stir for 1.5 h at rt. The solution was precipitated into 40 mL of diethyl ether. The precipitate was collected through centrifugation and re-dissolved into 12 mL of THF. The solution was then precipitated into 100 mL of diethyl ether. The precipitate was collected through centrifugation, washed with 90 mL of diethyl ether and 90 mL of hexane, and kept under vacuum overnight for removing residual solvents. Yield 250 mg of product, 72% yield based upon ~ 98% conversion for **M3** and ~ 95% conversion for **M6**, respectively.  $M_{n, \text{GPC}} = 189$  kDa (laser detector), PDI = 1.30.  $^1\text{H}$  NMR (500 MHz,  $\text{DMSO-}d_6$ ,  $\delta$ ) 9.20–9.75 (br, phenol OHs), 7.75–8.00 (m, Ar Hs from RAFT functionality), 6.20–7.75 (m, Ar Hs), 5.00–5.50 (br,

brush backbone  $CH=CH$ ), 4.40–4.80(br, TFEMA  $OCH_2CF_3$ ), 0.60–4.20 (all  $CH_3$ s,  $CH_2$ s, and  $CH$ s from *p*HS, MI, and TFEMA unit backbones, and PNB backbone). TGA in  $N_2$ : 340–415 °C, 37% mass loss, 415–485 °C, 5% mass loss, 56% mass remaining above 500 °C.

### 3.3.7. Synthesis of brush **B** ( $P(NB-g-PTFEMA_{34})_4-b-P(NB-g-P(pHS_{11}-co-PhMI_{11}))_{33}$ )

To a 10 mL Schlenk flask equipped with a magnetic stirring bar dried with flame under  $N_2$  atmosphere, was added the modified Grubbs catalyst (3.20 mg, 4.40  $\mu$ mol) and 0.3 mL of anhydrous  $CH_2Cl_2$ . The reaction mixture was stirred 1 min at rt to obtain a homogeneous solution and deoxygenated through three cycles of freeze-pump-thaw and back-filled with  $N_2$ . After the last cycle, the solution of **M3** (106 mg, 17.6  $\mu$ mol) in 0.7 mL of anhydrous  $CH_2Cl_2$  (deoxygenated through three cycles of freeze-pump-thaw) was quickly added with an airtight syringe. The reaction mixture was allowed to stir for 35 min at rt before adding the solution of **M7** (444 mg, 123  $\mu$ mol) in 3.5 mL of anhydrous THF (deoxygenated through three cycles of freeze-pump-thaw) with an airtight syringe. The reaction mixture was stirred for 4 h at rt before quenching the polymerization by adding 0.45 mL of EVE, and was further allowed to stir for 1 h at rt. The solution was precipitated into 100 mL of diethyl ether. The precipitate was collected through centrifugation and re-dissolved into 15 mL of THF. The solution was then precipitated into 150 mL of diethyl ether. The precipitate was collected through centrifugation, washed with 100 mL of diethyl ether and 100 mL of hexane, and kept under vacuum overnight for removing residual solvents. Yield 440 mg of product, 82% yield based upon ~ 98%

conversion for **M3** and ~ 93% conversion for **M7**, respectively.  $M_{n, GPC} = 217$  kDa (laser detector), PDI = 1.20. The  $^1\text{H}$  NMR spectrum was similar as **A**.

### 3.3.8. Synthesis of brush **C** ( $P(\text{NB-g-PBTFHMBMA}_{17})_6\text{-b-}P(\text{NB-g-}P(p\text{HS}_8\text{-co-PhMI}_8))_{42}$ )

To a 10 mL Schlenk flask equipped with a magnetic stirring bar dried with flame under  $\text{N}_2$  atmosphere, was added the modified Grubbs catalyst (3.21 mg, 4.41  $\mu\text{mol}$ ) and 0.5 mL of anhydrous  $\text{CH}_2\text{Cl}_2$ . The reaction mixture was stirred 1 min at rt to obtain a homogeneous solution, deoxygenated through three cycles of freeze-pump-thaw, and back-filled with  $\text{N}_2$ . After the last cycle, the solution of **M4** (150 mg, 26.6  $\mu\text{mol}$ ) in 1.0 mL of anhydrous THF/ $\text{CH}_2\text{Cl}_2$  (v/v = 3:7, deoxygenated through three cycles of freeze-pump-thaw) was quickly added with an airtight syringe. The reaction mixture was allowed to stir for 55 min at rt before adding the solution of **M6** (386 mg, 142  $\mu\text{mol}$ ) in 2.5 mL of anhydrous THF (deoxygenated through three cycles of freeze-pump-thaw) with an airtight syringe. The reaction mixture was stirred for 4 h at rt before quenching the polymerization by adding 0.4 mL of EVE, and was further allowed to stir for 1.5 h at rt. The solution was precipitated into 85 mL of diethyl ether. The precipitate was collected through centrifugation and re-dissolved into 12 mL of THF. The solution was then precipitated into 80 mL of diethyl ether. The precipitate was collected through centrifugation, washed with 100 mL of diethyl ether and 100 mL of hexane, and kept under vacuum overnight for removing residual solvents. Yield 363 mg of product, 73% yield based upon ~ 95% conversion for **M4** and ~ 92% conversion for **M6**, respectively.  $M_{n, GPC} = 196$  kDa (laser detector), PDI = 1.30.  $^1\text{H}$  NMR (500 MHz,  $\text{DMSO-}d_6$ ,  $\delta$ ) 9.13–9.95 (br, phenol OHs), 5.91–8.05 (m, Ar Hs from RAFT functionality, *p*HS, and PhMI units,

and  $\text{HOC}(\text{CF}_3)_2$ ), 4.90–5.58 (br, brush backbone  $\text{CH}=\text{CH}$ ), 0.54–4.09 (m,  $\text{CH}_2\text{OC}(\text{O})$  from NB and BTFHMBMA units, all  $\text{CH}_3$ s,  $\text{CH}_2$ s, and  $\text{CH}$ s from BTFHMBMA unit,  $p\text{HS}$ , MI, and BTFHMBMA unit backbones, and PNB backbone). TGA in  $\text{N}_2$ : 290–405 °C, 50% mass loss, 405–480 °C, 10% mass loss, 33% mass remaining above 500 °C.

### 3.3.9. Synthesis of brush **D** ( $P(\text{NB-g-PBTFHMBMA}_{21})_5\text{-b-P}(\text{NB-g-P}(p\text{HS}_{17}\text{-co-PhMI}_{17}))_{41}$ )

To a 10 mL Schlenk flask equipped with a magnetic stirring bar dried with flame under  $\text{N}_2$  atmosphere, was added the modified Grubbs catalyst (3.02 mg, 4.15  $\mu\text{mol}$ ) and 0.4 mL of anhydrous  $\text{CH}_2\text{Cl}_2$ . The reaction mixture was stirred 1 min at rt to obtain a homogeneous solution, deoxygenated through three cycles of freeze-pump-thaw, and back-filled with  $\text{N}_2$ . After the last cycle, the solution of **M5** (142 mg, 20.7  $\mu\text{mol}$ ) in 1.1 mL of anhydrous THF/ $\text{CH}_2\text{Cl}_2$  (v/v = 3:8, deoxygenated through three cycles of freeze-pump-thaw) was quickly added with an airtight syringe. The reaction mixture was allowed to stir for 45 min at rt before adding the solution of **M8** (656 mg, 125  $\mu\text{mol}$ ) in 4.5 mL of anhydrous THF/ $\text{CH}_2\text{Cl}_2$  (v/v = 2:1, deoxygenated through three cycles of freeze-pump-thaw) with an airtight syringe. The reaction mixture was stirred for 6 h at rt before quenching the polymerization by adding 0.6 mL of EVE, and was further allowed to stir for 1 h at rt. The solution was precipitated into 200 mL of diethyl ether. The precipitate was collected through centrifugation and re-dissolved into 20 mL of THF. The solution was then precipitated into 180 mL of diethyl ether. The precipitate was collected through centrifugation, washed with 200 mL of diethyl ether and 200 mL of hexane, and kept under vacuum overnight for removing residual solvents. Yield 538 mg of product, 71% yield

based upon ~ 95% conversion for **M5** and ~ 95% conversion for **M8**, respectively.  $M_n$ , GPC = 403 kDa (laser detector), PDI = 1.28. The  $^1\text{H}$  NMR spectrum was similar as **C**.

#### 3.3.10. General procedure for the preparation of polymer thin film

The solution of brush polymer in cyclohexanone (1.0 wt%) was prepared and passed through a PTFE syringe filter (220 nm pore size) before using. The solution was applied onto UV-O<sub>3</sub> pre-treated silicon wafer (*the amount of applied polymer solution should be sufficient to cover the whole wafer surface*) and spin coated at 500 rpm for 5 seconds, followed by spinning at 3,000 rpm for 30 seconds (*200 rpm/s acceleration rate for each step*) to afford thin film with 20 to 30 nm thickness.

#### 3.3.11. General procedure for the acetone annealing of polymer thin film.

The polymer film-coated silicon wafer was kept in a desiccator filled with saturated acetone atmosphere under vacuum for 24 hours. After the annealing process, the excess solvent was removed by pumping under vacuum and the N<sub>2</sub> gas was slowly backfilled to open the desiccator.

### 3.4. Conclusion

In summary, nanoscopic cylindrical DBTs with lithographically-addressable block segments, including poly(fluoro methacrylate)-based blocks that function as substrate vertical alignment promoters and P(*p*HS-*co*-PhMI)-based blocks that serve both to further enhance vertical alignment via promotion of substrate adhesion and to undergo crosslinking chemistry for the production of lithographic patterns, were synthesized by combinations of controlled radical and ring opening metathesis polymerizations. By performing bottom-up pre-assembly of block copolymer segments, which individually or

collectively have lithographically-addressable components covalently incorporated into different regions of the molecular brush architecture, cylindrical nanoscopic objects are generated and utilized for assembly into photoresist thin films, a second bottom-up approach. The structure-property-relationship studies were designed to probe the effects of their compositions and dimensions concentrically and lengthwise, revealing that the more hydrophobic PTFEMA grafts in one domain and higher cross-section of polar grafts in the other domain optimized their vertical alignment on the polar silicon wafer substrates. The thin films composed of vertically-assembled block brush copolymers of highly uniform composition and chain length offer opportunities to demonstrate efficient top-down patterning approaches to advanced photolithography.

CHAPTER IV

ADVANCED PHOTORESIST TECHNOLOGIES BY INTRICATE MOLECULAR  
BRUSH ARCHITECTURES: DIBLOCK BRUSH TERPOLYMER-BASED  
POSITIVE-TONE PHOTORESIST MATERIALS\*

#### 4.1. Introduction

Patterning technique advances that allow fabrication of materials on continuously shrinking scales serve as enablers in the enhancement of high-speed computing and high-capacity data storage devices. Currently, the cost of reducing the wavelength of the photons used in conventional top-down photolithography increases exponentially. This high cost leads to consideration of alternative patterning strategies such as the bottom-up optimization and redesign of functional polymers for chemically-amplified resists (CARs)<sup>67,131,132</sup> to extend the device shrink roadmap accessible to the microelectronics industry. In addition to the chemical functionality and the microstructure,<sup>67,132</sup> the topology of polymer photoresist materials has been recognized and demonstrated as an emerging parameter in the development of CARs; specifically in areas with the simultaneous requirements of high sensitivity, high resolution and high structural integrity.<sup>127,133-137</sup> For several decades, Jean Fréchet has been a leader in the introduction

---

\* Reprinted with permission from “Advanced Photoresist Technologies by Intricate Molecular Brush Architectures: Diblock Brush Terpolymer-Based Positive-Tone Photoresist Materials” by Guorong Sun, Sangho Cho, Fan Yang, Xun He, Adriana Pavia-Sanders, Corrie Clark, Jeffery E. Raymond, Stanislav V. Verkhoturov, Emile A. Schweikert, James W. Thackeray, Peter Trefonas, and Karen L. Wooley, *J. Polym. Sci., Part A: Polym. Chem.* **2015**, 53(2), 193-199. Copyright © 2014 Wiley Periodicals, Inc.



of creative chemistries that have significantly advanced photoresist technologies for application in the microelectronics industry.<sup>85,100,135-146</sup> Early contributions, together with C. Grant Willson and Hiroshi Ito, led to the fundamental acid-catalyzed chemistry<sup>100,138-141</sup> that serves as the foundation of CARs,<sup>147</sup> and more recently, Fréchet and co-workers introduced a novel class of dendritic polymers,<sup>85,137,146</sup> which represents the first nonlinear polymer architecture towards high-performance resist materials. The repetitively-branched topology of the dendrimers limits chain entanglements and molecular volume, which consequently results in higher sensitivity of the resist and reduces the line-edge roughness of generated patterns. This strategy has also been leveraged *via* the use of hyperbranched polymers<sup>133</sup> and star polymers<sup>134</sup> with relatively facile accessibilities (controlled radical polymerizations), displaying enhanced lithographic behaviors when producing latent patterns at low exposure dosages.

The unique architecture of bottle brush polymers<sup>49,86</sup> or molecular brushes makes these systems attractive for the development of novel photoresist technologies. The individually- or collectively-addressable rigid backbone and densely tethered grafts dictate that the macromolecules behave as cylindrical nanoscopic objects, and also allow for partitioning of specific chemical functionalities into selective regions.<sup>51,53,90,125</sup> When prepared *via* a “grafting through” synthetic approach,<sup>49,86</sup> the resulting modularity provides pathways to an array of macromolecular functionalities, shapes, and dimensions.<sup>51,53,90,125,127</sup> This diversity can then be applied to produce a high degree of control over the synthetic chemistry and allow tuning of the chemical composition and microstructure throughout the entire brush framework.

In our previous investigations, the utilization of diblock brush terpolymers (DBTs) as negative-tone photoresists for electron beam lithography (EBL) with high sensitivity and high resolution was realized.<sup>127,128</sup> The particular design principle, construction of molecular brushes consisting of a surface energy reducing block and a lithographic functional block with concentric blocking manner, promotes the vertical alignment of brushes on substrates and provides reactive sites for photoacid-catalyzed chemical reactions. In this work, we apply a similar strategy to positive-tone photoresist materials. Our system is comprised of three elementary chemical components: (1) an alkyl fluorocarbon to drive vertical alignment from the substrate, (2) an acid-labile tertiary ester to enable acid-catalyzed deblocking chemistry, and (3) a polar lactone to enhance surface adhesion (Figure 4.1). The results presented in this communication confirmed the validities of our conceptual designs and established a positive-tone CAR that can create dense patterns with 70 nm line features at exposure dosage less than 2.0 mJ/cm<sup>2</sup>.

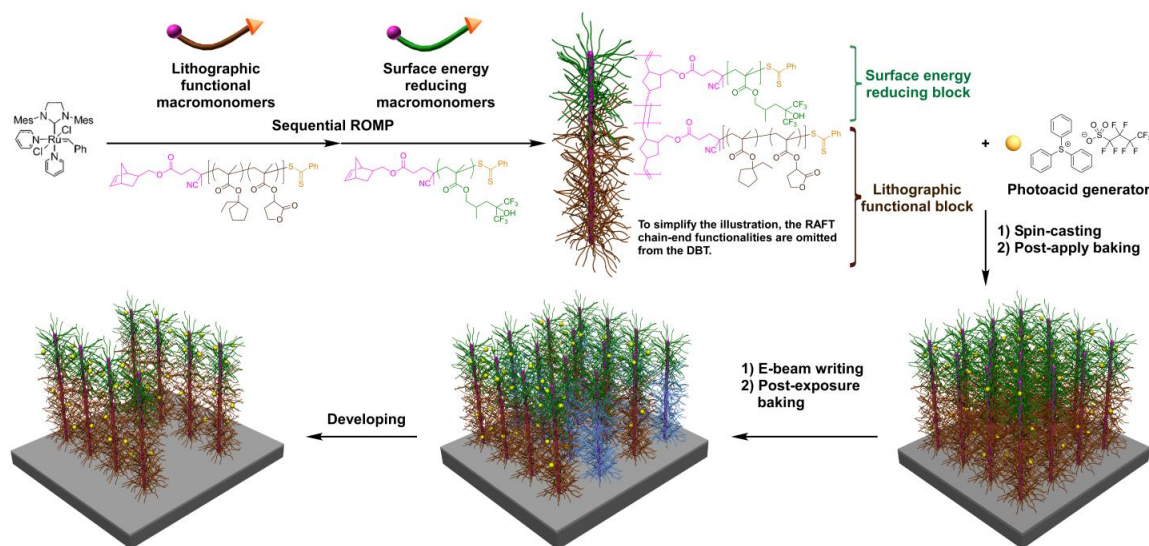


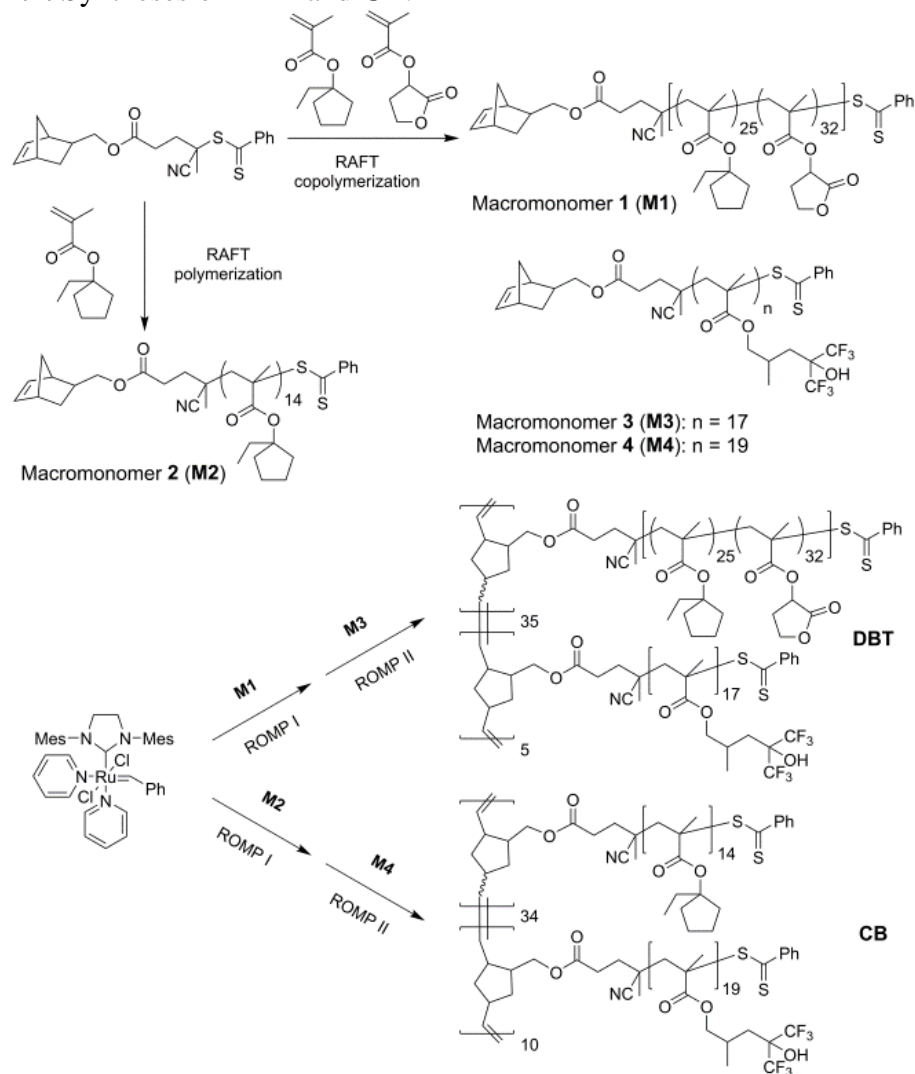
**Figure 4.1.** Schematic conceptualization of composition and preparation of **DBT**; a positive-tone photoresist material; and lithographic process by using a monolayer thin film comprised of ideally vertically-aligned **DBT**s and physically-blended PAGs on a PS-primed silicon wafer.

## 4.2. Results and Discussion

As depicted in Figure 4.1 and Scheme 4.1, the designed **DBT** and control brush systems were synthesized through sequential ring-opening metathesis polymerization (ROMP)<sup>92</sup> of preconstructed macromonomers<sup>51,90,125,127</sup> bearing norbornene (NB) chain-end functionalities. From a NB-terminated dithioester chain transfer agent, the reversible addition-fragmentation chain transfer (RAFT) copolymerization of 1-ethylcyclopentyl methacrylate (ECPMA) and  $\gamma$ -butyrolactone-2-yl methacrylate (GBLMA) as a comonomer pair at an ECPMA:GBLMA feed ratio of 1:1 (Supporting Information, Experimental Section) afforded NB-P(ECPMA<sub>25</sub>-co-GBLMA<sub>32</sub>) macromonomer (**M1**, Scheme 4.1). We also prepared a NB-PECPMA<sub>14</sub> macromonomer (**M2**) from RAFT homopolymerization of ECPMA, which served as a building block to construct a control

brush (**CB**) for studying the structure-performance relationship of the lactone functional group. Interestingly, faster polymerization kinetics for ECPMA was observed during the copolymerization process, *i.e.*, >80% conversion after 14 h *vs.* 70% after 17 h in homopolymerization. This difference could be attributed to a polarity-activation mechanism in the copolymerization.<sup>148</sup> The RAFT polymerization of 1,1,1-trifluoro-2-(trifluoromethyl)-2-hydroxy-4-methyl-5-pentyl methacrylate (BTFHMBMA) was used to synthesize the fluorinated macromonomers **3** and **4** (**M3**, NB-PBTFHMBMA<sub>17</sub> and **M4**, NB-PBTFHMBMA<sub>19</sub>). The preparation and characterization of these macromonomers are reported elsewhere.<sup>149</sup>

**Scheme 4.1. Syntheses of DBT and CB.**



The well-defined structures of **M1** and **M2** were confirmed by  $^1\text{H}$  NMR spectroscopic analyses (Figure 4.2), in which the peak integral ratios of the characteristic polymer chain-end NB alkenyl (6.08 ppm) and RAFT agent phenyl (7.30–7.90 ppm) protons closely agreed with the theoretical value of 2:5. In addition, the  $^1\text{H}$  NMR-determined number-averaged molecular weights ( $M_{\text{n}}$ s) of **M1** (10,400 Da) and **M2** (2,940 Da) had rational consistency with the gel permeation chromatography (GPC)

measurements (11,700 Da and 3,460 Da from laser detection, for **M1** and **M2**, respectively). The GPC characterizations of both macromonomers confirmed their monomodal and narrow molecular weight distributions (Figure 4.3, dashed lines) with low polydispersity indices (PDIs) of *ca.* 1.10. The spectroscopic and size exclusion results further verify the overall controlled manner of these RAFT polymerizations. As a note, the actual repeat unit ratio between GBLMA and ECPMA in **M1** was 28% higher than the comonomer pair feed ratio. This difference is reasonably attributed to the complicated cross-propagation and cross-chain transfer processes in the RAFT copolymerization of methacrylate comonomers with noticeable steric hindrance and polarity differences.

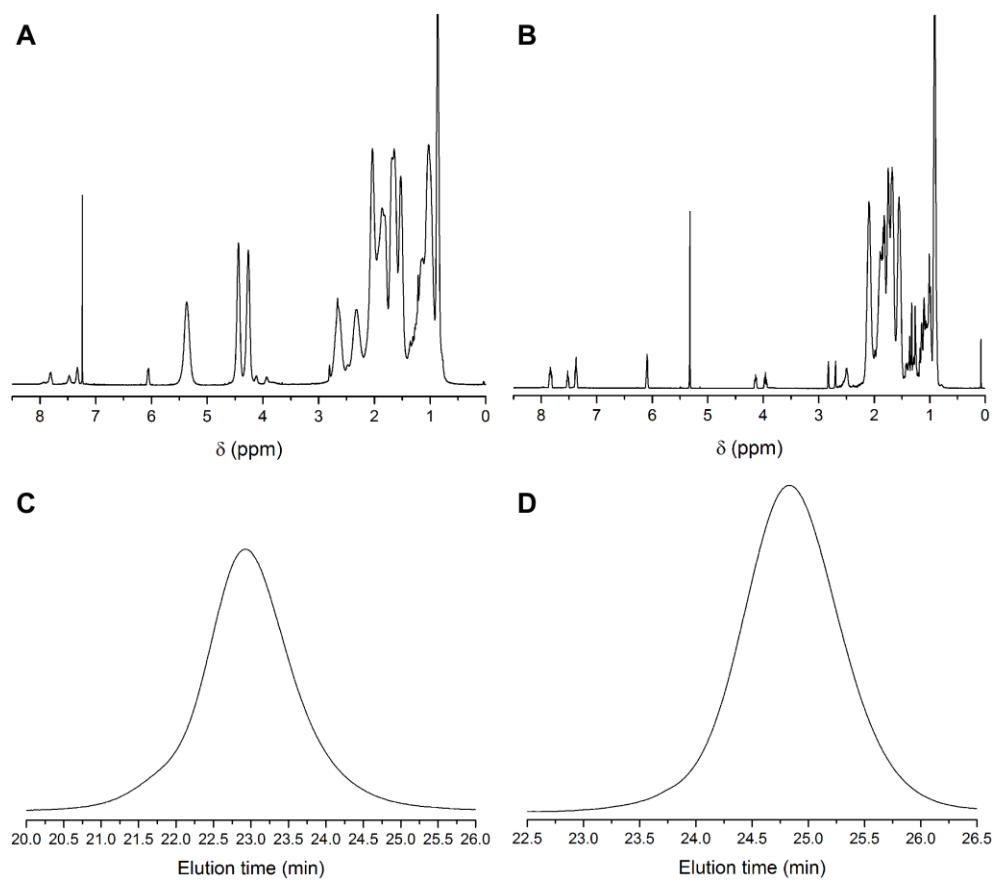


**Figure 4.2.** (a, b) The  $^1\text{H}$  NMR spectrum for **M1** (a, 500 MHz,  $\text{CDCl}_3$ ) and **M2** (b, 500 MHz,  $\text{CD}_2\text{Cl}_2$ ), respectively. (c, d) The GPC profile for **M1** (c) and **M2** (d), respectively.

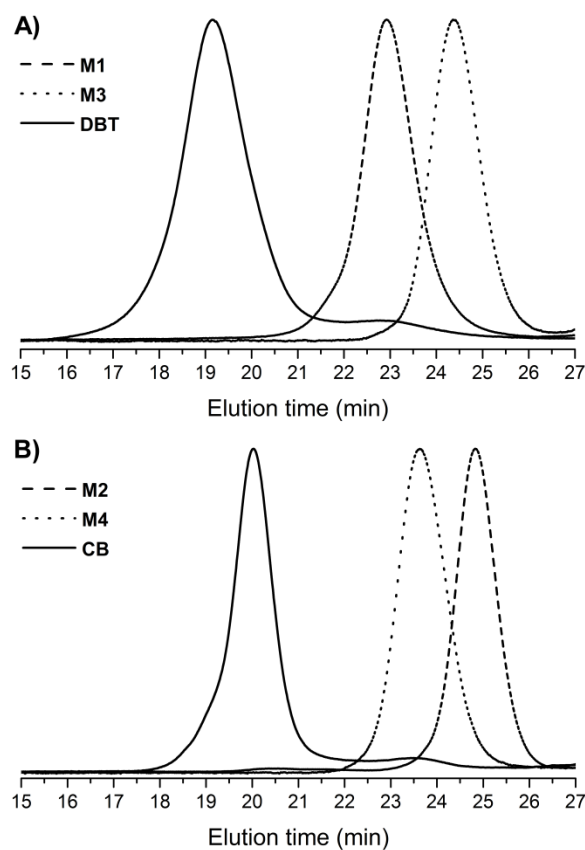


**Figure 4.3.** Normalized GPC profiles of **M1** and **M2** (dashed lines), **M3** and **M4** (dotted lines), **DBT** and **CB** (solid lines).

The **DBT** [P(NB-*g*-P(ECPMA<sub>25</sub>-*co*-GBLMA<sub>32</sub>)<sub>35</sub>-*b*-P(NB-*g*-PBTFHMBMA<sub>17</sub>)<sub>5</sub>,  $M_n^{\text{GPC}} = 443$  kDa, PDI = 1.18, 2.19 wt% F, Figure 4.3a] and the **CB** [P(NB-*g*-PECPMA<sub>14</sub>)<sub>34</sub>-*b*-P(NB-*g*-PBTFHMBMA<sub>19</sub>)<sub>10</sub>,  $M_n^{\text{GPC}} = 205$  kDa, PDI = 1.15, 10.6 wt% of F, Figure 4.3b] were constructed by a sequential grafting-through strategy of the corresponding macromonomer pairs utilizing a modified Grubbs' catalyst (Scheme 4.1, applying a fixed feed ratio of 1:30:6 for [cat.]<sub>0</sub>:**[M1]**<sub>0</sub>:**[M3]**<sub>0</sub> and [cat.]<sub>0</sub>:**[M2]**<sub>0</sub>:**[M4]**<sub>0</sub>). The sequential ROMPs were monitored by <sup>1</sup>H NMR analysis of aliquots withdrawn at pre-determined time intervals, in which >90% conversion was observed for each



macromonomer, as evidenced by the “disappearance” of NB alkenyl protons. The appearances of characteristic  $\text{CH}_2\text{OC}(\text{O})$  methylene protons (3.50–4.00 ppm) from BTFHMBMA in the  $^1\text{H}$  NMR spectra of both brushes (Figure 4.4), in addition to the resonances from ECPMA (**CB**) and from ECPMA and GBLMA (**DBT**), clearly confirmed the establishment of the block terpolymer structures.

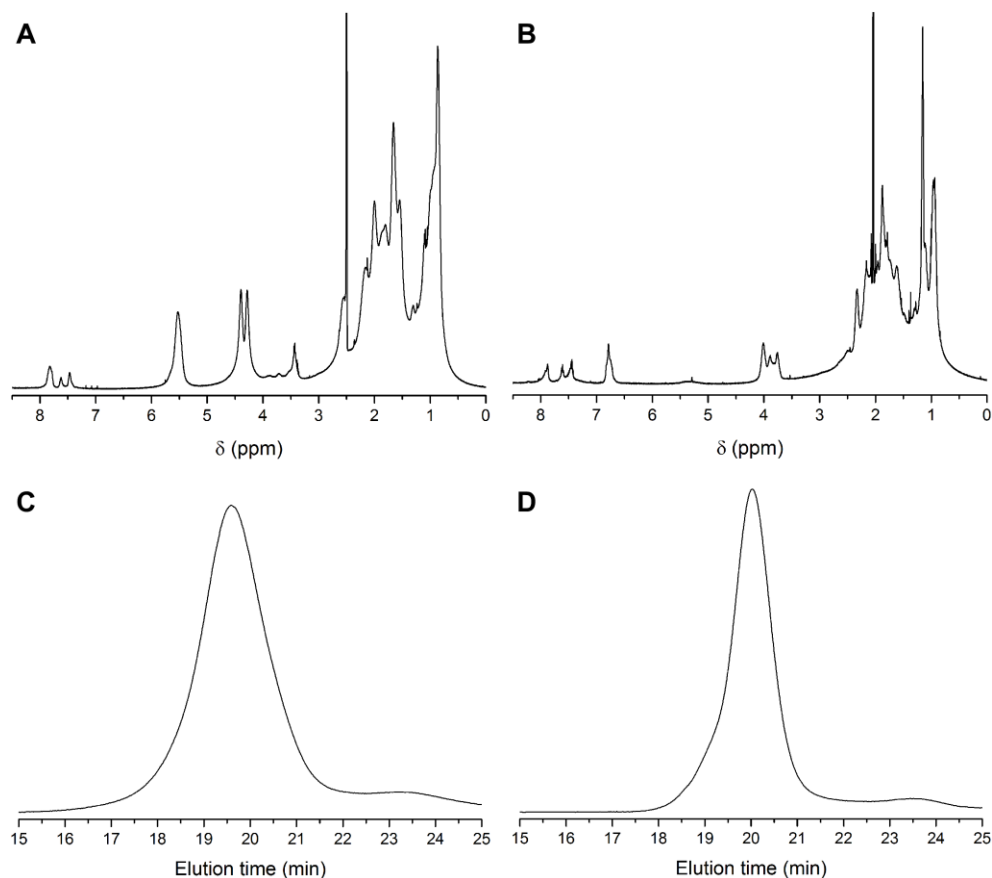


**Figure 4.4.** (a, b) The  $^1\text{H}$  NMR spectrum for **DBT** (a, 500 MHz,  $\text{DMSO}-d_6$ ) and **CB** (b, 500 MHz,  $\text{acetone}-d_6$ ), respectively. (c, d) The GPC profile for **DBT** (c) and **CB** (d), respectively.

Polymer thin films were prepared by spin-casting 1.0 wt% solutions of molecular brushes in cyclohexanone onto UV-O<sub>3</sub> treated silicon wafers. As characterized by tapping-mode atomic force microscopy (AFM), the as-cast **DBT** films exhibited sufficiently homogeneous surface topography (Figure 4.5a) with height root-mean-square (RMS) roughness <0.3 nm. The film thickness from the selected concentration was  $25 \pm 1$  nm (measured by AFM), which showed agreement with the corresponding PNB backbone contour length (estimated 24 nm based upon 0.6 nm for each NB unit<sup>63</sup>) and indicated that the **DBT** film comprises a monolayer of the molecular brush components that preferably adopted vertical alignment on the substrate. By comparison, the thickness of as-cast **CB** film,  $20 \pm 1$  nm by AFM, was 23% lower than the backbone contour length (estimated 26 nm), which suggested that the brushes might be quasi-aligned through mixed spatial orientations within the **CB** film. Meanwhile, the AFM images showed noticeably increased film surface heterogeneity with height RMS roughness of 0.6 nm (Figure 4.5b). We speculate that these phenomena are caused by insufficient attractions between the PECPMA grafts and the polar UV-O<sub>3</sub>-treated silicon wafer surface due to a lack of lactone functionalities in **CB** precursors. This hypothesis was supported by the morphological variations of **CB** film after acetone vapor annealing, in which large “island” features of microscopic size were formed (Figure 4.6b). For the **DBT** film, the solvent annealing process actually promoted the brushes to reach fully perpendicular orientations within the film (*vide infra*) and a more homogeneous film surface was observed.

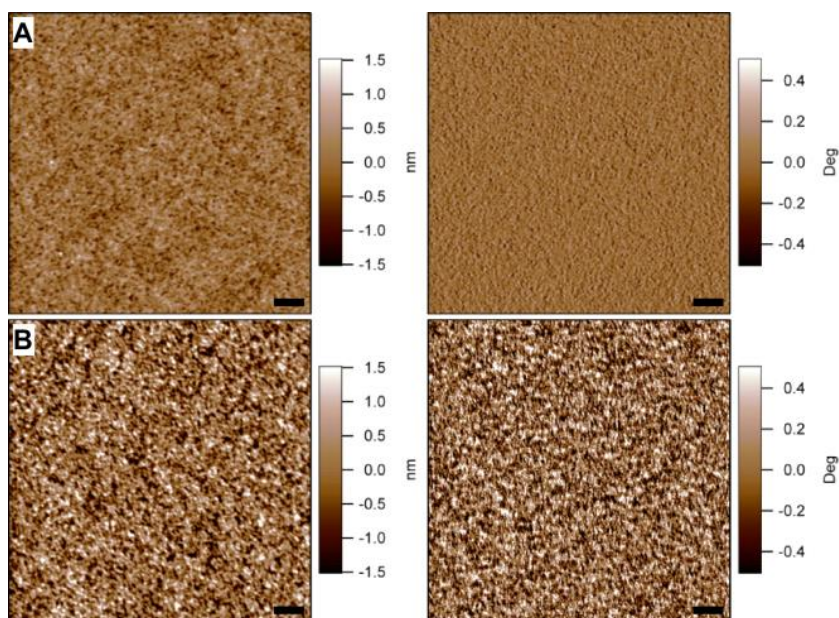


**Figure 4.5.** Tapping-mode AFM height (left column) and phase (right column) images of as-cast **DBT** (a) and **CB** (b) films, respectively. Scale bars: 500 nm.

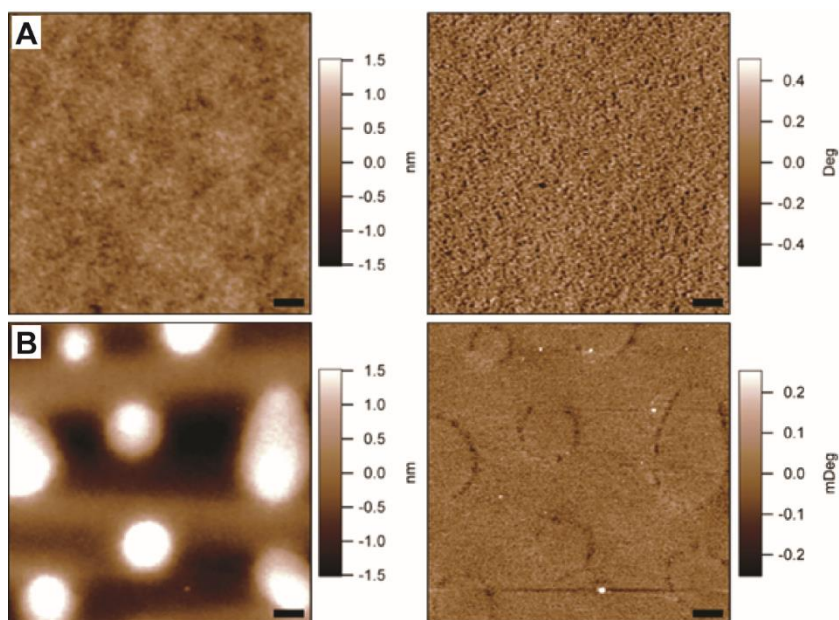


**Figure 4.6.** Tapping-mode AFM height (left column) and phase (right column) images of the acetone-annealed **CB** (a) and **DBT** (b) films, respectively. Scale bars: 500 nm.

The relative surface F content and the surface coverage of the **DBT** film, from X-ray photoelectron spectroscopy (XPS, Table 4.1) and  $C_{60}$  secondary-ion mass spectrometry (Figure 4.7), quantified that over 83% of the brushes were vertically aligned across the substrate surface without any special annealing treatment (Figure 4.8). Compared with the film from **CB**, there was a 20% increase in the extent of brush vertical alignment within the **DBT** film. The incorporation of GBL as a surface adhesion functionality in **DBT** increased the attractions between the P(ECPMA-*co*-GBLMA) grafts and the substrate, providing assistance to the surface energy-driven migration of the F-containing block towards the air interface, ensuring a higher extent of **DBT** with perpendicular off-plane orientations within the film. It is noteworthy that the larger substrate contact area and weaker “pulling” interactions in **DBT** (*vs.* **CB**), enabled by the longer lithographic functional side chains and shorter surface energy reducing block, may also result in a synergistic effect for better vertical alignment of the brushes. Upon annealing the **DBT** film with acetone vapor, the relative surface F content and the surface coverage became equal to the theoretical values (Table 4.1), which confirmed the full elongation to an uncompromised vertical alignment of the brushes. The morphological improvements in the film consequently enhanced the film surface hydrophobicity, as evidenced by the increased water static contact angle and the decreased surface free energy (Table 4.2).

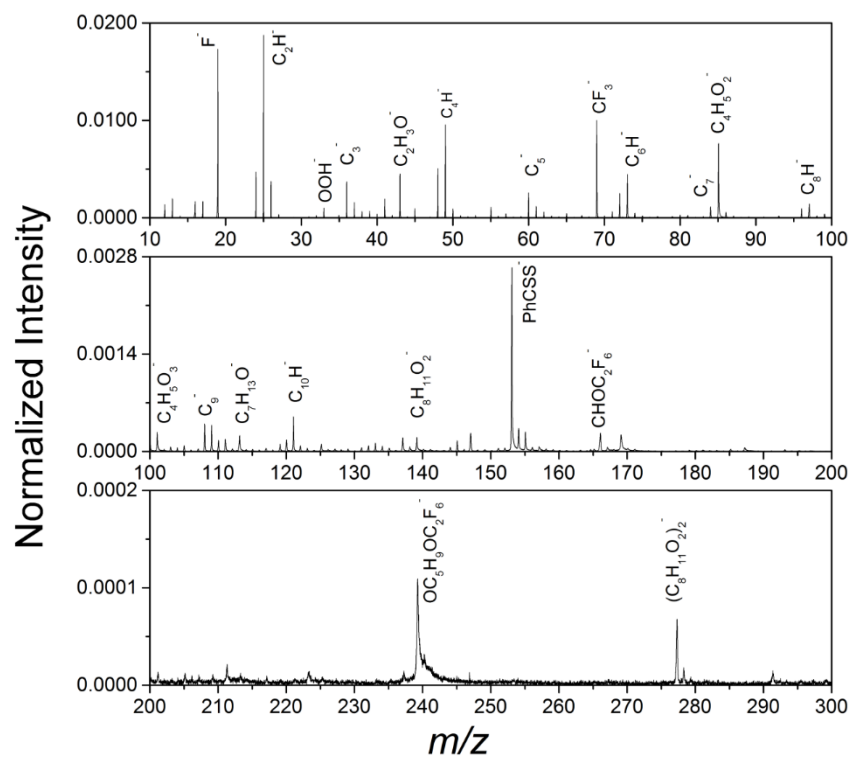


**Figure 4.7.**  $C_{60}$  SIMS spectrum of the as-cast DBT film.

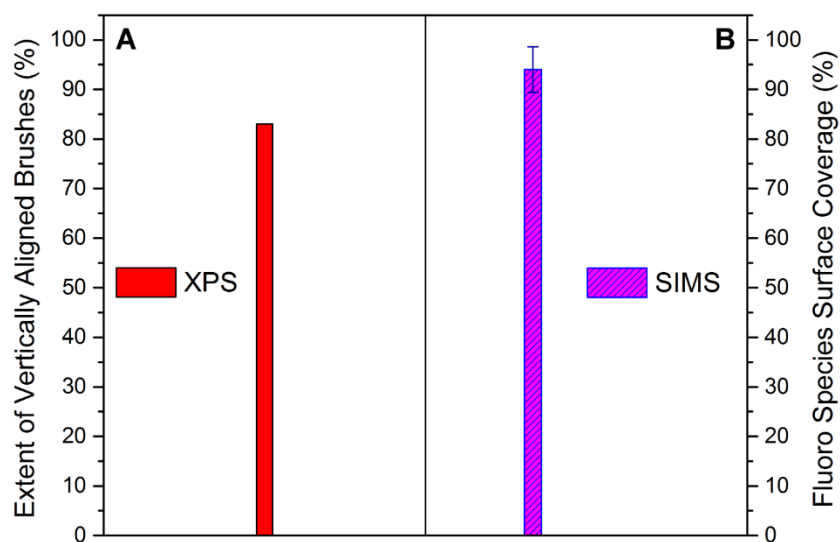


**Figure 4.8.** (a) Percentage of the vertically aligned **DBTs** within the as-cast film (red bar), calculated based upon the relative surface F content measured from XPS *vs.* the theoretical F content. (b) Surface coverage by SIMS (pink bar), presented by the percentage of co-emitted F-containing ions from nanodomains of the as-cast **DBT** film.

**Table 4.1.** Relative ratios of elements in polymer films surface from XPS measurements.

		C1s@285 eV	O1s@532 eV	F1s@688 eV
		[%]	[%]	[%]
<b>DBT</b>	Spin-cast	74.2	21.7	3.8
	Acetone-annealed	72.6	22.0	4.8
	Random distributed	74.1	23.9	1.9
	Ideally vertical aligned <sup>a</sup>	72.2	22.8	4.8
<b>CB</b>	Spin-cast	73.1	13.9	12.3
	Acetone-annealed	71.5	13.6	14.4
	Random distributed	74.7	14.6	10.3
	Ideally vertical aligned <sup>a</sup>	64.3	14.6	20.8

<sup>a</sup> The relative ratio of elements in ideally vertical aligned film is calculated based on the depth up to 10 nm from the film surface.

$$\% \text{ Vertical alinement} = \frac{F_{\text{sample}}}{F_{\text{ideal}}} \times 100$$

**Table 4.2.** Summary of static contact angles and surface free energies of brush polymer films.

		Static contact angle [°]		Surface free
		Water	Diiodomethane	energy [mJ m <sup>-2</sup> ]
<b>DBT</b>	Spin-cast	78 ± 1	58 ± 1	36.4
	Acetone-annealed	83 ± 1	57 ± 1	34.6
<b>CB</b>	Spin-cast	76 ± 1	68 ± 1	33.8
	Acetone-annealed	84 ± 1	67 ± 1	30.3

The lithographic performance of a **DBT**-based CAR was evaluated by performing post-exposure baking EBL (PEB-EBL) and measuring the width of the resulting lines from three designed patterns, having 70/120, 100/100, and 100/60 nm exposure line/space features, respectively. Triphenylsulfonium perfluoro-1-butanefosonate was used as a physically-blended photoacid generator (PAG), at a formulation of **DBT**:PAG = 0.9 wt%:0.1 wt% in cyclohexanone. Different from our previous negative-tone PEB-EBL

work, a hydroxyl-terminated polystyrene ( $M_n^{\text{GPC}} = 3,950$  Da, PDI = 1.08) priming of the silicon wafer<sup>150</sup> was found to be a necessary step for optimizing the production of latent patterns. The primed surface offers supplementary substrate adhesion of non-deblocking brushes<sup>151</sup> after PEB-EBL, ultimately resulting in enhanced stability of the patterned features. After spin-casting the CAR onto the PS-primed wafers, post-apply baking (PAB) was conducted at 90 °C for 2 min to afford  $22 \pm 1$  nm films. The selected PAB temperature was below the glass transition temperature of **DBT** (105 °C from differential scanning calorimetry analysis) to limit potential thermal disorder. Solvent vapor annealing was not applied, in an attempt to avoid complications that might induce heterogeneous distribution of PAGs in the CAR film, *i.e.*, concentration of the F-rich ionic PAGs into the P(NB-*g*-PBTFHMBMA) domain. These films were then used for EBL at 50 and 60  $\mu\text{C}/\text{cm}^2$  exposure dosages (1.5 and 1.8  $\text{mJ}/\text{cm}^2$ , respectively), followed by empirical PEB processes (100 °C for 2 min) to complete the acidolysis of ECPMA within the exposed areas. To reduce alkaline hydrolysis of lactone functionalities during development (typically an aqueous tetramethylammonium hydroxide, TMAH, solution is used in lithography),<sup>152</sup> which can produce a polarity change for unexposed brushes and affect their substrate adhesion and solubility, a shorter developing time (20 sec) in a weaker developer (0.1 M TMAH<sub>aq.</sub>) was used.

As shown in Figure 4.9 (right column), the **DBT** CAR could resolve all three designed patterns and generate satisfactory line and space features at 115/75 (Figure 4.9b), 105/95 (Figure 4.9d), and 70/90 (Figure 4.9f) nm line/space widths,<sup>153</sup> respectively, from the 60  $\mu\text{C}/\text{cm}^2$  exposure dosages. By comparison, the patterns generated from 50  $\mu\text{C}/\text{cm}^2$



exposure dosages (Figure 4.9, left column) showed either microbridge defects (Figure 4.9a, left corner) or larger line roughnesses (Figure 4.9c and 4.9e). Accounting for the higher extent of brush vertical alignment and the diameter of the cylindrical **DBT** in this study, *i.e.*, ~ 35 nm assuming full extension of an all-*trans* conformation of the P(ECPMA-*co*-GBLMA) grafts, the ca. 70-nm lines could be an assembly of two to three vertically-aligned **DBT** molecules. Other patterns with lateral line widths less than 50 nm were also tested, by applying the current resist. However, the approach to molecular pixel scale caused insufficient two-dimensional support from neighboring molecules. Further systematic and precise optimizations of the **DBT** lengthwise and concentric dimensions, to achieve higher resolution images, are currently underway.

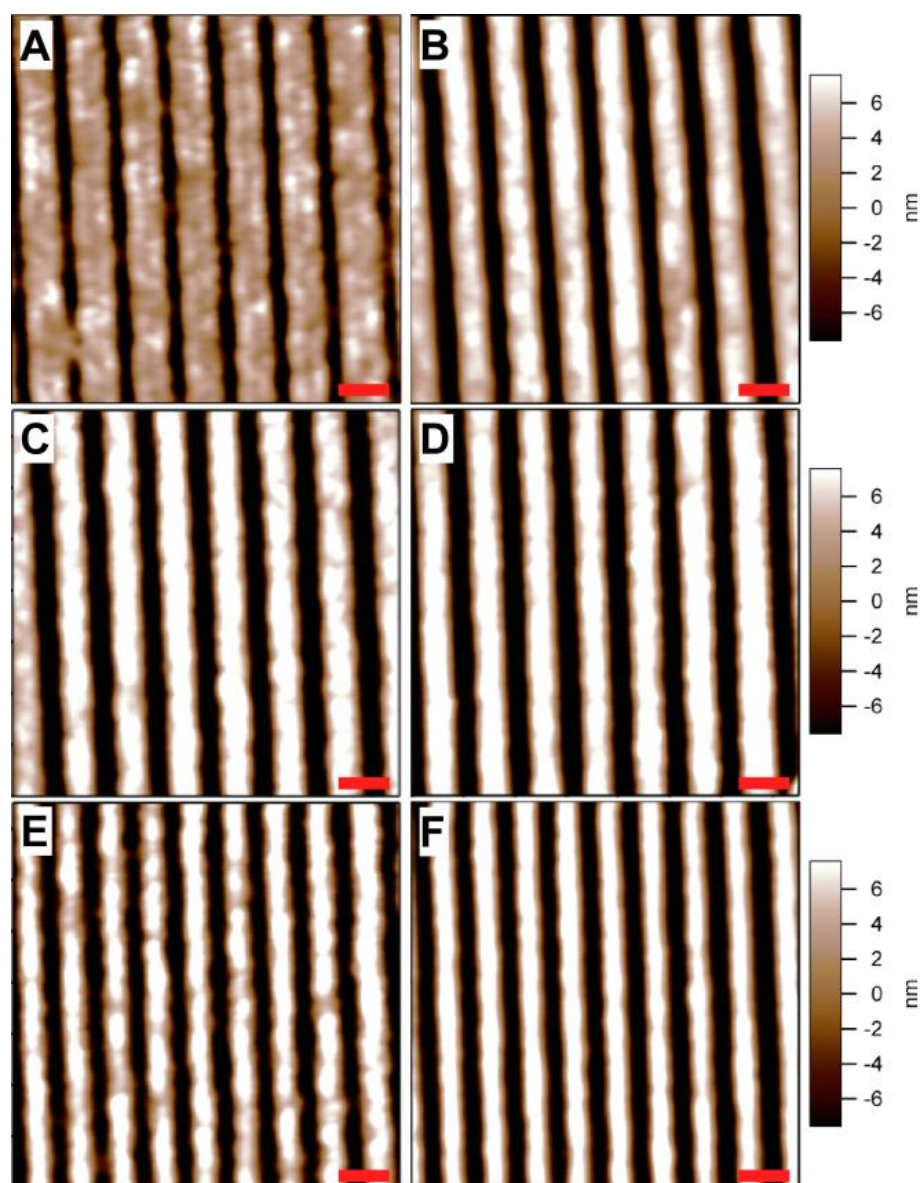


**Figure 4.9.** Tapping-mode AFM images of latent 120/70 nm (a, b), 100/100 nm (c, d), and 60/100 nm (e, f) line/space patterns, respectively, generated from 70/120, 100/100, and 100/60 nm exposure line/space features PEB-EBL of **DBT** CAR at 50 (left column) and 60 (right column)  $\mu\text{C}/\text{cm}^2$  exposure dosages. Scale bars: 200 nm.

### 4.3. Experimental Section

#### 4.3.1. Materials

The modified Grubbs' catalyst,<sup>89</sup> NB-CTA,<sup>103</sup> and macromonomers **3** and **4**,<sup>149</sup> were synthesized as previously reported. The 1-ethylcyclopentyl methacrylate (ECPMA) and  $\gamma$ -butyrolactone-2-yl methacrylate (GBLMA) were provided by the Dow Chemical Company. Other chemicals were purchased from Aldrich, Acros, and VWR and were used without further purification unless otherwise noted. Prior to use, the ECPMA was purified by passing through a neutral alumina column to remove the inhibitor. The 1,4-dioxane, dichloromethane ( $\text{CH}_2\text{Cl}_2$ ), and tetrahydrofuran (THF) were purified by passing them under argon pressure through solvent purification system (JC Meyer Solvent Systems).

#### 4.3.2. Instruments

$^1\text{H}$  and  $^{13}\text{C}$  NMR spectra were recorded on a Varian 500 MHz spectrometer interfaced to a LINUX computer using VNMR-J software. Chemical shifts were referred to the solvent proton resonance.

The polymer molecular weight and molecular weight distribution were determined by gel permeation chromatography (GPC). The GPC was conducted on a Waters 1515 HPLC (Waters Chromatography, Inc.) equipped with a Waters 2414 differential refractometer, a PD2020 dual-angle ( $15^\circ$  and  $90^\circ$ ) light scattering detector (Precision Detectors, Inc.), and a three-column series (PL gel  $5\mu\text{m}$  Mixed C,  $500\text{ \AA}$ , and  $10^4\text{ \AA}$ ,  $300 \times 7.5\text{ mm}$  columns; Polymer Laboratories, Inc.). The system was equilibrated at  $40\text{ }^\circ\text{C}$  in THF, which served as the polymer solvent and eluent with a flow rate of  $1.0\text{ mL/min}$ .

Polymer solutions were prepared at a known concentration (3–5 mg/mL) and an injection volume of 200  $\mu$ L was used. Data collection and analysis were performed with Precision Acquire software and Discovery 32 software (Precision Detectors, Inc.), respectively. Inter-detector delay volume and the light scattering detector calibration constant were determined by calibration using a nearly monodispersed polystyrene standard (Polymer Laboratories,  $M_p = 90$  kDa,  $M_w/M_n < 1.04$ ). The differential refractometer was calibrated with standard polystyrene reference material (SRM 706 NIST), of known specific refractive index increment  $dn/dc$  (0.184 mL/g). The  $dn/dc$  values of the analyzed polymers were then determined from the differential refractometer response.

The glass transition temperatures ( $T_g$ ) were measured by differential scanning calorimetry on a Mettler-Toledo DSC822 (Mettler-Toledo, Inc.), with a heating rate of 10  $^{\circ}$ C/min. The measurements were analyzed by using Mettler-Toledo STARe software. The  $T_g$  was taken as the midpoint of the inflection tangent, upon the first heating scan. Thermogravimetric analysis (TGA) was performed under  $N_2$  atmosphere using a Mettler-Toledo model TGA/SDTA851, with a heating rate of 5  $^{\circ}$ C/min. The measurements were analyzed by using Mettler-Toledo STARe software.

The surface energy of the film was calculated with Owens–Wendt–Rabel–Kaelble (OWRK) method after measuring the contact angle with optical tensiometer (KSV Instruments, Attension Theta). The X-ray photoelectron spectroscopy (XPS) experiments were performed on a Kratos Axis Ultra XPS system with a monochromatic aluminum X-ray source (10 mA, 12 kV). The binding energy scale was calibrated to 285 eV for the main C1s peak.

The secondary ion mass spectrometry (SIMS) measurements were carried out with a custom-built SIMS instrument coupled to a time-of-flight (TOF) mass analyzer.<sup>104</sup> The instrument used in these studies is equipped with a C<sub>60</sub> effusion source capable of producing C<sub>60</sub><sup>2+</sup> projectiles with total impact energy of 50 keV. The SIMS analysis of the polymer samples was conducted in the superstatic regime, where less than 0.1% of the surface is impacted. This restriction ensured that each time the surface was impacted by a primary ion, an unperturbed area of the surface was sampled. The superstatic measurements were conducted in the event-by-event bombardment-detection mode, where a single primary ion impacted on the surface and the secondary ions were collected and analyzed prior to subsequent primary ions impacting the surface. The event-by-event bombardment mode enables quantitative surface analysis without external standardization.<sup>105,106</sup> Coincidence mass spectra, *i.e.*, spectra showing ions co-emitted with a specific secondary ion of interest were extracted from the records of the individual impacts. All secondary ions detected in a single impact originated from a 10 nm radius on the surface.<sup>130</sup>

Each polymer sample was measured three times at different locations on the sample by TOF-SIMS. Each measurement consisted of  $\sim 3 \times 10^6$  projectile impacts on an area  $\sim 100 \mu\text{m}$  in radius. Multiple measurements were performed to ensure sample consistency. A quantitative estimate of surface coverage of fluorine containing molecules was calculated for each sample by using coincidence counting technique by the comparison of the signals at  $m/z = 19$ , corresponding to F<sup>-</sup>,  $m/z = 69$ , corresponding to

$\text{CF}_3^-$ ,  $m/z = 167$ , corresponding to  $\text{C}_2\text{F}_6\text{CHO}^-$ , and  $m/z = 239$ , corresponding to  $\text{C}_2\text{F}_6\text{OC}_5\text{H}_9\text{O}^-$ , with the signal of “coincidentally emitted/detected” anions (Figure S4).<sup>6</sup>

The atomic force microscopy (AFM) imaging was performed on MFP-3D system (Asylum Research) in tapping mode using standard silicon tips (VISTAprobes, T190-25, resonance constant: 190 kHz, tip radius:  $\sim 10$  nm, spring constant: 48 N/m).

The EBL was carried out by using JEOL JSM-6460 scanning electron microscope equipped with DEBEN laser stage. The system was operated at 30 kV accelerating voltage and 10 pA beam current with two exposure dosages of 50 and 60  $\mu\text{C}/\text{cm}^2$  (corresponding to 1.5 to 1.8  $\text{mJ}/\text{cm}^2$ ). Three  $5 \times 5$   $\mu\text{m}$  patterns, having 70/120, 100/100, and 100/60 nm exposure line/space features, respectively, were designed and used to evaluate the lithographic behaviors of polymer resists.

#### 4.3.3. *Synthesis of macromonomer 1 [MI, NB-P(ECPMA<sub>25</sub>-co-GBLMA<sub>32</sub>)]*

To a 25 mL Schlenk flask equipped with a magnetic stirring bar dried with flame under  $\text{N}_2$  atmosphere, was added NB-CTA (244 mg, 0.635 mmol), ECPMA (2.31 g, 12.7 mmol), GBLMA (2.16 g, 12.7 mmol), AIBN (10.3 mg, 63.5  $\mu\text{mol}$ ), and 6 mL of 2-butanone. The mixture was stirred 10 min at rt, deoxygenated through five cycles of freeze-pump-thaw and back-filled with  $\text{N}_2$ . After the last cycle, the reaction mixture was stirred 10 min at rt and immersed into a pre-heated oil bath at 65  $^\circ\text{C}$  to start the polymerization. After 14 h, the polymerization was quenched by cooling the reaction flask with liquid  $\text{N}_2$ . The copolymer was purified by precipitation into 250 mL of diethyl ether twice. The precipitate was collected through centrifugation, washed with 200 mL of diethyl ether and 200 mL of hexane, and kept under vacuum overnight for removing

residual solvents. Yield 3.47 g of product, 88% yield based upon ~ 88% conversion of GBLMA, ~ 80% conversion of ECPMA, and ~ 80% conversion of NB-CTA.  $M_{n, \text{GPC}} = 11,700$  Da (laser detector),  $PDI = 1.10$ .  $M_{n, \text{NMR}} = 10,400$  Da.  $^1\text{H NMR}$  (500 MHz,  $\text{CDCl}_3$ )  $\delta$  7.30–7.90 (m, Ar *Hs* from RAFT functionality), 6.08 (s, NB  $\text{CH}=\text{CH}$ ), 5.18–5.58 (br, GBL  $\text{OCHC}(\text{O})$ ), 3.90–4.60 (m, NB  $\text{CH}_2\text{OC}(\text{O})$  and GBL  $\text{CH}_2\text{OC}(\text{O})$ ), 2.81–2.85 (s, NB allylic *H*), 0.72–2.78 (m, all  $\text{CH}_3\text{s}$ ,  $\text{CH}_2\text{s}$ , and  $\text{CHs}$  from ECPMA units, GBLMA units, and NB-CTA).

#### 4.3.4. Synthesis of macromonomer 2 (**M2**, NB-PECPMA<sub>14</sub>)

To a 25 mL Schlenk flask equipped with a magnetic stirring bar dried with flame under  $\text{N}_2$  atmosphere, was added NB-CTA (308 mg, 0.80 mmol), ECPMA (2.18 g, 12.0 mmol), AIBN (19.4 mg, 0.12 mmol), and 5 mL of 2-butanone. The mixture was stirred 10 min at rt, deoxygenated through four cycles of freeze-pump-thaw and back-filled with  $\text{N}_2$ . After the last cycle, the reaction mixture was stirred 10 min at rt and immersed into a pre-heated oil bath at 63 °C to start the polymerization. After 17 h, the polymerization was quenched by cooling the reaction flask with liquid  $\text{N}_2$ . The polymer was purified by precipitation into 150 mL of cold methanol (~ -10 °C) twice. The precipitate was collected through centrifugation, washed with 100 mL of methanol, and kept under vacuum overnight for removing residual solvents. Yield 1.16 g of product, 65% yield based upon ~ 70% conversion of ECPMA and ~ 82% conversion of NB-CTA.  $M_{n, \text{GPC}} = 3,460$  Da (laser detector),  $PDI = 1.08$ .  $M_{n, \text{NMR}} = 2,940$  Da.  $^1\text{H NMR}$  (500 MHz,  $\text{CD}_2\text{Cl}_2$ )  $\delta$  7.32–7.88 (m, Ar *Hs* from RAFT functionality), 6.08 (br, NB  $\text{CH}=\text{CH}$ ), 3.92–4.18 (m, NB-CTA

$\text{CH}_2\text{OC}(\text{O})$ ), 2.66–2.86 (m, NB allylic  $\text{Hs}$ ), 0.74–2.60 (m, all  $\text{CHs}$ ,  $\text{CH}_2\text{s}$  and  $\text{CH}_3\text{s}$  from NB-CTA and ECPMA units).

#### 4.3.5. Synthesis of **DBT** $[P(\text{NB-g-P}(\text{ECPMA}_{25}\text{-co-GBLMA}_{32})_{35}\text{-b-P}(\text{NB-g-PBTFHMBMA}_{17})_5)]$

To a 10 mL Schlenk flask equipped with a magnetic stirring bar dried with flame under  $\text{N}_2$  atmosphere, was added the modified Grubbs' catalyst (2.66 mg, 3.65  $\mu\text{mol}$ ) and 0.6 mL of anhydrous  $\text{CH}_2\text{Cl}_2$ . The reaction mixture was stirred 1 min at rt to obtain a homogeneous solution and deoxygenated through three cycles of freeze-pump-thaw and back-filled with  $\text{N}_2$ . After the last cycle, the solution of **M1** (1.14 g, 0.11 mmol) in 5.4 mL of anhydrous  $\text{CH}_2\text{Cl}_2$  (deoxygenated through three cycles of freeze-pump-thaw) was quickly added with an airtight syringe. The reaction mixture was allowed to stir for 230 min at rt before adding the solution of **M3** (125 mg, 22.0  $\mu\text{mol}$ ) in 0.6 mL of anhydrous THF (deoxygenated through three cycles of freeze-pump-thaw) with an airtight syringe. The reaction mixture was stirred for 3 h at rt before quenching the polymerization by adding 0.5 mL of EVE, and was further allowed to stir for 15 h at rt. The solution was precipitated into 125 mL of diethyl ether/MeOH (v/v = 4:1). The precipitate was collected through centrifugation and re-dissolved into 15 mL of  $\text{CH}_2\text{Cl}_2$ . The solution was then precipitated into 200 mL of diethyl ether. The precipitate was collected through centrifugation, washed with 100 mL of diethyl ether/MeOH (v/v = 9:1) and 200 mL of hexane, and kept under vacuum overnight for removing residual solvents. Yield 970 mg of product, 81% yield based upon ~ 95% conversion for both **M1** and **M3**, respectively.  $M_{\text{n, GPC}} = 443 \text{ kDa}$  (laser detector),  $PDI = 1.18$ .  $^1\text{H}$  NMR (500 MHz,  $\text{DMSO-}d_6$ )  $\delta$  7.42–



7.92 (m, Ar *H*s from RAFT functionality and  $\text{HOC}(\text{CF}_3)_2$ ), 5.22–5.76 (br, GBL  $\text{OCHC}(\text{O})$ s and brush backbone  $\text{CH}=\text{CH}$ s), 3.80–4.70 (m,  $\text{CH}_2\text{OC}(\text{O})$ s from NB-CTA, GBLMA units, and BTFHMBMA units), 0.76–2.76 (m, all  $\text{CH}$ s,  $\text{CH}_2$ s, and  $\text{CH}_3$ s from NB-CTA, ECPMA units, GBLMA units, and BTFHMBMA units).  $^{13}\text{C}$  NMR (125 MHz,  $\text{DMSO}-d_6$ )  $\delta$  206.9, 175.6, 172.6, 128.7, 126.2, 124.5, 122.3, 120.0, 93.4, 75.7, 68.4, 65.1, 56.0, 52.5, 46.0, 44.7, 35.4, 34.6, 32.8, 30.4, 29.7, 28.0, 24.2, 18.2, 8.6. IR ( $\text{cm}^{-1}$ ): 3720–3220, 2959, 2881, 1792, 1728, 1448, 1382, 1346, 1223, 1140, 1016, 949, 858, 764, 706.  $T_g$ : 105 °C. TGA in  $\text{N}_2$ : 110–170 °C, 5% mass loss, 182–220 °C, 10% mass loss, 220–390 °C, 40% mass loss, 390–460 °C, 26% mass loss, 17% mass remaining above 500 °C.

#### 4.3.6. Synthesis of **CB** [ $P(\text{NB}-g\text{-PECPMA}_{14})_{34}\text{-}b\text{-}P(\text{NB}-g\text{-PBTFHMBMA}_{19})_{10}$ ]

To a 10 mL Schlenk flask equipped with a magnetic stirring bar dried with flame under  $\text{N}_2$  atmosphere, was added the modified Grubbs catalyst (2.77 mg, 3.80  $\mu\text{mol}$ ) and 0.5 mL of anhydrous  $\text{CH}_2\text{Cl}_2$ . The reaction mixture was stirred 1 min at rt to obtain a homogeneous solution and deoxygenated through three cycles of freeze-pump-thaw and back-filled with  $\text{N}_2$ . After the last cycle, the solution of **M2** (336 mg, 114  $\mu\text{mol}$ ) in 2.5 mL of anhydrous  $\text{CH}_2\text{Cl}_2$  (deoxygenated through three cycles of freeze-pump-thaw) was quickly added with an airtight syringe. The reaction mixture was allowed to stir for 2 h at rt before adding the solution of **M4** (142 mg, 22.8  $\mu\text{mol}$ ) in 0.3 mL of anhydrous THF (deoxygenated through three cycles of freeze-pump-thaw) with an airtight syringe. The reaction mixture was stirred for 3 h at rt before quenching the polymerization by adding 0.6 mL of EVE, and was further allowed to stir for 1 h at rt. The solution was precipitated into 90 mL of hexane. The precipitate was collected through centrifugation and re-

dissolved into 7 mL of THF/CH<sub>2</sub>Cl<sub>2</sub> (v/v = 1:1). The solution was then precipitated into 90 mL of hexane. The precipitate was collected through centrifugation, washed with 50 mL of hexane, and kept under vacuum overnight for removing residual solvents. Yield 260 mg of product, 82% yield based upon ~ 95% conversion for both **M2** and **M4**, respectively.  $M_{n, GPC} = 205$  kDa (laser detector),  $PDI = 1.15$ . <sup>1</sup>H NMR (500 MHz, Acetone-*d*<sub>6</sub>)  $\delta$  7.18–8.10 (m, Ar *H*s from RAFT functionality), 6.58–6.90 (*HOC*(CF<sub>3</sub>)<sub>2</sub>S from BTFHMBMA units), 5.02–5.56 (br, brush backbone *CH=CH*s), 3.62–4.24 (m, *CH*<sub>2</sub>OC(O)s from NB-CTA and BTFHMBMA units), 0.56–3.18 (m, all *CH*s, *CH*<sub>2</sub>s, and *CH*<sub>3</sub>s from NB-CTA, ECPMA units, and BTFHMBMA units).

#### 4.3.7. General procedure for the preparation of polymer thin film

The solution of **DBT** or **CB** in cyclohexanone (1.0 wt%) was prepared and passed through a PTFE syringe filter (220 nm pore size) before using. The solution was applied onto UV-O<sub>3</sub> pre-treated silicon wafer (*the amount of applied polymer solution should be sufficient to cover the whole wafer surface*) and spin coated at 500 rpm for 5 seconds, followed by spinning at 3,000 rpm for 30 seconds (*200 rpm/s acceleration rate for each step*) to afford thin film with 25 or 20 nm thickness, respectively.

#### 4.3.8. General procedure for the acetone annealing of polymer thin film

The polymer film-coated silicon wafer was kept in a desiccator filled under vacuum with saturated acetone atmosphere for 24 hours. After the annealing process, the excess solvent was removed by pumping under vacuum and the N<sub>2</sub> gas was slowly backfilled to open the desiccator.

#### 4.3.9. General procedure for priming the UV-O<sub>3</sub> treated wafer with PS-OH

The solution of PS-OH in cyclohexanone was prepared and passed through a PTFE syringe filter (220 nm pore size) before using. The solution was applied onto UV-O<sub>3</sub> pre-treated silicon wafer (*the amount of applied solution should be sufficient to cover the whole wafer surface*) and spin coated at 500 rpm for 5 seconds, followed by spinning at 3,000 rpm for 30 seconds (*200 rpm/s acceleration rate for each step*). The PS-OH treated wafer was then annealed under vacuum (~ 180 mmHg) at 120 °C for 24 h. The wafer was sonicated in toluene for 5 min to remove ungrafted PS-OH, washed with fresh toluene and dried by N<sub>2</sub> flow.

#### 4.3.10. General procedure for preparation of DBT CAR thin film for EBL

The solution of **DBT**:PAG (0.9 wt%:0.1 wt%) in cyclohexanone was prepared and passed through a PTFE syringe filter (220 nm pore size) before using. The solution was applied onto PS-OH primed silicon wafer (*the amount of applied solution should be sufficient to cover the whole wafer surface*) and spin coated at 500 rpm for 5 seconds, followed by spinning at 3,000 rpm for 30 seconds (*200 rpm/s acceleration rate for each step*) and PAB at 90 °C for 2 min to afford thin film with 22 nm thickness.

#### 4.3.11. General procedure for EBL

After electron beam “writing” with predesigned pattern, the exposed wafer was post-baked on a 100 °C hotplate for 2 min and dipped into 0.1 M TMAH<sub>(aq)</sub> solution for 20 sec. The wafers were rinsed with DI water and dried by N<sub>2</sub> flow.

#### 4.4. Conclusion

In summary, we have demonstrated a P(NB-*g*-P(ECPMA-*co*-GBLMA)-*b*-P(NB-*g*-PBTFHMBMA) diblock brush terpolymer capable of performing as an advanced positive-tone photoresist technology. This system relies on a bottom-up strategy of pre-assembly during substrate adhesion, surface-active migration, and chemically-reactive deblocking functional compositions into selective regions within the cylindrical polymer brush architectures. Large-areas of vertical alignment of the polymers within thin films allowed for near-molecular pixel resolution (2-3 molecules) after EBL. The presented system displays proof-of-concept for the translation of previously proven negative-tone photoresist molecular brush assembly strategies to a positive-tone regime; also displays the fundamental advantages of high macromolecular and regiochemical control in simultaneous top-down/bottom-up construction of CAR systems.

## CHAPTER V

### CONCLUSIONS

Nanoscopic cylindrical DBTs that can vertically align on substrates and function as lithographic pixels were synthesized by controlled radical and olefin metathesis polymerizations. RAFT (co)polymerizations of monomers having surface energy reducing, substrate adhesion enhancing, and lithographically functioning moieties provide macromonomers with well-defined sized variations. Sequential ROMPs of the macromonomers via a “grafting-through” strategy enable the high degree of control in both dimension, with concentric and lengthwise manners, and composition at selected positions in the brush polymer structure.

The DBTs within thin films were vertically aligned on substrates with the help of structural and compositional effects. The stretched conformation of the backbone polymer in DBTs, due to the repulsive interaction of grafted side chains, provides facile access to nanoscopic cylindrical objects and facilitates their assembly by reducing chain entanglement. Low surface energy of fluoropolymers on one block of the DBTs drives them to the air/polymer interface, while high polar groups on the other block attract the polar silicon wafer substrate. These combinatorial effects, along with optimization of compositional and dimensional ratios, allow the molecular cylindrical brushes to vertically align on the substrates. In addition, solvent annealing accelerates the assembly by improving mobility of the brushes.

The CARs from the DBT precursors showed high lithographic performance with a few tens of nanometer resolution. In EBL, DBTs with PpHSs gave negative-tone features by crosslinking chemistry, while those with PECPMAs, having acid-labile tertiary esters, gave positive-tone features. In comparison to linear block copolymer precursors, CARs with cylindrical brush precursors showed superior lithographic performance in both resolution and sensitivity by having each vertically aligned molecule act as a molecular pixel. Furthermore, the dimensions of cylindrical brushes effect the lithographic performance; the thinner brushes give better resolution, while the thicker ones provide better sensitivity. As a result, fine tuning of performance in top-down lithography was achieved by the tuning of composition and dimensions using a bottom-up synthetic strategy.

Further optimization of dimensions in the architecture of DBTs and introduction of new chemical functionalities providing better sensitivity and alignment is believed to yield advanced lithographic performance with narrow pattern features and small edge roughness. Covalently-binding PAGs to the brush chains could narrow the pattern size by reducing acid diffusion. Highly efficient chemistry such as ring-opening of epoxides, or thiol-ene click chemistry, is expected to give better sensitivity. Introduction of new chemical functionalities to both ends of the cylindrical brush or the use of chemically pre-functionalized substrates can enhanced the alignment of bottle brush polymers. Also, it is meaningful to apply these DBTs to extreme UV lithography for high throughput pattern generation. The strategy of vertical alignment of cylindrical bottle brush polymers is not limited to lithography technology but can expand to other nanostructure fabrication. In

particular, devices demanding electron or photon transportation in a directional manner such as photovoltaics and light emitting diodes can be good candidates. Also, the facile tuning of concentric and lengthwise dimensions and the selective removal of brush composition are applicable to the preparation of templates with well-defined periodicity and channel size.

## REFERENCES

- (1) Wagner, C.; Harned, N. *Nat. Photon.* **2010**, *4*, 24-26.
- (2) Tseng, A. A.; Kuan, C.; Chen, C. D.; Ma, K. J. *IEEE Trans. Electron. Packag. Manuf.* **2003**, *26*, 141-149.
- (3) Chang, T. H. P. *J. Vac. Sci. Technol.* **1975**, *12*, 1271-1275.
- (4) Proximity Effect in E-beam Lithography;  
<http://nanolithography.gatech.edu/proximity.htm>.
- (5) Reichmanis, E.; Houlihan, F. M.; Nalamasu, O.; Neenan, T. X. *Adv. Mater. Opt. Electron.* **1994**, *4*, 83-93.
- (6) Ito, H.; Willson, C. G. *Polym. Eng. Sci.* **1983**, *23*, 1012-1018.
- (7) Crivello, J. V. *ACS Symp. Ser.* **1984**, *242*, 3-10.
- (8) Ito, H. *Proc. SPIE* **1999**, *3678*, 2-12.
- (9) Schlesinger, S. I. *Polym. Eng. Sci.* **1974**, *14*, 513-515.
- (10) Thackeray, J. W.; Orsula, G. W.; Pavelchek, E. K.; Canistro, D.; Bogan, J. L. E.; Berry, A. K.; Graziano, K. A. *Proc. SPIE* **1989**, *1086*, 34-47.
- (11) Liu, H. y.; deGrandpre, M. P.; Feely, W. E. *J. Vac. Sci. Technol., B* **1988**, *6*, 379-383.
- (12) Reck, B.; Allen, R. D.; Twieg, R. J.; Willson, C. G.; Matuszczak, S.; Stover, H. D. H.; Li, N. H.; Fréchet, J. M. J. *Polym. Eng. Sci.* **1989**, *29*, 960-964.
- (13) Chang, S. W.; Ayothi, R.; Bratton, D.; Yang, D.; Felix, N.; Cao, H. B.; Deng, H.; Ober, C. K. *J. Mater. Chem.* **2006**, *16*, 1470-1474.



- (14) Lawson, R. A.; Cheng, J.; Cheshmehkani, A.; Tolbert, L. M.; Henderson, C. L. *Proc. SPIE* **2013**, 8682, 868221.
- (15) Ross, C. A.; Berggren, K. K.; Cheng, J. Y.; Jung, Y. S.; Chang, J.-B. *Adv. Mater.* **2014**, 26, 4386-4396.
- (16) Hawker, C. J.; Russell, T. P. *MRS Bull.* **2005**, 30, 952-966.
- (17) Fired, J. *Polymer Science and Technology*; 2nd ed.; Prentice Hall: Upper Saddle River, NJ, 2003.
- (18) Flory, P. J. *Principles of Polymer Chemistry*; Cornell University Press: Ithaca, NY, 1953.
- (19) Leibler, L. *Macromolecules* **1980**, 13, 1602-1617.
- (20) Botiz, I.; Darling, S. B. *Mater. Today* **2010**, 13, 42-51.
- (21) Kim, H.-C.; Park, S.-M.; Hinsberg, W. D. *Chem. Rev.* **2010**, 110, 146-177.
- (22) Koo, K.; Ahn, H.; Kim, S.-W.; Ryu, D. Y.; Russell, T. P. *Soft Matter* **2013**, 9, 9059-9071.
- (23) Hu, H.; Gopinadhan, M.; Osuji, C. O. *Soft Matter* **2014**, 10, 3867-3889.
- (24) Stoykovich, M. P.; Kang, H.; Daoulas, K.; Liu, G.; Liu, C. C.; de Pablo, J. J.; Muller, M.; Nealey, P. F. *ACS Nano* **2007**, 1, 168-175.
- (25) Cheng, J. Y.; Ross, C. A.; Smith, H. I.; Thomas, E. L. *Adv. Mater.* **2006**, 18, 2505-2521.
- (26) Ruiz, R.; Ruiz, N.; Zhang, Y.; Sandstrom, R. L.; Black, C. T. *Adv. Mater.* **2007**, 19, 2157-2162.

- (27) Cheng, J. Y.; Rettner, C. T.; Sanders, D. P.; Kim, H.-C.; Hinsberg, W. D. *Adv. Mater.* **2008**, *20*, 3155-3158.
- (28) Tada, Y.; Akasaka, S.; Yoshida, H.; Hasegawa, H.; Dobisz, E.; Kercher, D.; Takenaka, M. *Macromolecules* **2008**, *41*, 9267-9276.
- (29) Xu, J.; Park, S.; Wang, S.; Russell, T. P.; Ocko, B. M.; Checco, A. *Adv. Mater.* **2010**, *22*, 2268-2272.
- (30) Knoll, A.; Horvat, A.; Lyakhova, K. S.; Krausch, G.; Sevink, G. J. A.; Zvelindovsky, A. V.; Magerle, R. *Phys. Rev. Lett.* **2002**, *89*, 035501.
- (31) Turner, M. S. *Phys. Rev. Lett.* **1992**, *69*, 1788-1791.
- (32) Han, E.; Stuen, K. O.; Leolukman, M.; Liu, C.-C.; Nealey, P. F.; Gopalan, P. *Macromolecules* **2009**, *42*, 4896-4901.
- (33) Sinturel, C.; Vayer, M.; Morris, M.; Hillmyer, M. A. *Macromolecules* **2013**, *46*, 5399-5415.
- (34) Nandan, B.; Vyas, M. K.; Böhme, M.; Stamm, M. *Macromolecules* **2010**, *43*, 2463-2473.
- (35) Park, W. I.; Tong, S.; Liu, Y.; Jung, I. W.; Roelofs, A.; Hong, S. *Nanoscale* **2014**, *6*, 15216-15221.
- (36) Xuan, Y.; Peng, J.; Cui, L.; Wang, H.; Li, B.; Han, Y. *Macromolecules* **2004**, *37*, 7301-7307.
- (37) Kim, J. M.; Kim, Y.; Park, W. I.; Hur, Y. H.; Jeong, J. W.; Sim, D. M.; Baek, K. M.; Lee, J. H.; Kim, M.-J.; Jung, Y. S. *Adv. Funct. Mater.* **2015**, *25*, 306-315.

- (38) Kim, S. H.; Misner, M. J.; Xu, T.; Kimura, M.; Russell, T. P. *Adv. Mater.* **2004**, *16*, 226-231.
- (39) Albert, J. N. L.; Young, W.-S.; Lewis, R. L.; Bogart, T. D.; Smith, J. R.; Epps, T. H. *ACS Nano* **2011**, *6*, 459-466.
- (40) Hui, C. Y.; Wu, K. C.; Lasky, R. C.; Kramer, E. J. *J. Appl. Phys.* **1987**, *61*, 5129-5136.
- (41) Hui, C. Y.; Wu, K. C.; Lasky, R. C.; Kramer, E. J. *J. Appl. Phys.* **1987**, *61*, 5137-5149.
- (42) Wintermantel, M.; Gerle, M.; Fischer, K.; Schmidt, M.; Wataoka, I.; Urakawa, H.; Kajiwara, K.; Tsukahara, Y. *Macromolecules* **1996**, *29*, 978-983.
- (43) Gedde, U. W. *Polymer Physics*; Springer: London, 1995.
- (44) Hu, M.; Xia, Y.; McKenna, G. B.; Kornfield, J. A.; Grubbs, R. H. *Macromolecules* **2011**, *44*, 6935-6943.
- (45) Zhang, B.; Gröhn, F.; Pedersen, J. S.; Fischer, K.; Schmidt, M. *Macromolecules* **2006**, *39*, 8440-8450.
- (46) Lecommandoux, S.; Chécot, F.; Borsali, R.; Schappacher, M.; Deffieux, A.; Brûlet, A.; Cotton, J. P. *Macromolecules* **2002**, *35*, 8878-8881.
- (47) Runge, M. B.; Lipscomb, C. E.; Ditzler, L. R.; Mahanthappa, M. K.; Tivanski, A. V.; Bowden, N. B. *Macromolecules* **2008**, *41*, 7687-7694.
- (48) Runge, M. B.; Bowden, N. B. *J. Am. Chem. Soc.* **2007**, *129*, 10551-10560.
- (49) Rzaev, J. *ACS Macro Lett.* **2012**, *1*, 1146-1149.

- (50) Hong, S. W.; Gu, W.; Huh, J.; Sveinbjornsson, B. R.; Jeong, G.; Grubbs, R. H.; Russell, T. P. *ACS Nano* **2013**, 7, 9684-9692.
- (51) Xia, Y.; Olsen, B. D.; Kornfield, J. A.; Grubbs, R. H. *J. Am. Chem. Soc.* **2009**, 131, 18525-18532.
- (52) Rzaev, J. *Macromolecules* **2009**, 42, 2135-2141.
- (53) Bolton, J.; Bailey, T. S.; Rzaev, J. *Nano Lett.* **2011**, 11, 998-1001.
- (54) Bolton, J.; Rzaev, J. *ACS Macro Lett.* **2012**, 1, 15-18.
- (55) Chremos, A.; Theodorakis, P. E. *ACS Macro Lett.* **2014**, 3, 1096-1100.
- (56) Kim, J. C.; Rho, Y.; Kim, G.; Kim, M.; Kim, H.; Kim, I. J.; Kim, J. R.; Ree, M. *Polym. Chem.* **2013**, 4, 2260-2271.
- (57) Gao, H.; Matyjaszewski, K. *J. Am. Chem. Soc.* **2007**, 129, 6633-6639.
- (58) Lahasky, S. H.; Serem, W. K.; Guo, L.; Garino, J. C.; Zhang, D. *Macromolecules* **2011**, 44, 9063-9074.
- (59) Sun, J.; Hu, J.; Liu, G.; Xiao, D.; He, G.; Lu, R. *J. Polym. Sci., Part A: Polym. Chem.* **2011**, 49, 1282-1288.
- (60) Nese, A.; Li, Y.; Averick, S.; Kwak, Y.; Konkolewicz, D.; Sheiko, S. S.; Matyjaszewski, K. *ACS Macro Lett.* **2011**, 1, 227-231.
- (61) Zehm, D.; Laschewsky, A.; Liang, H.; Rabe, J. P. *Macromolecules* **2011**, 44, 9635-9641.
- (62) Bielawski, C. W.; Grubbs, R. H. *Prog. Polym. Sci.* **2007**, 32, 1-29.
- (63) Li, Z.; Zhang, K.; Ma, J.; Cheng, C.; Wooley, K. L. *J. Polym. Sci., Part A: Polym. Chem.* **2009**, 47, 5557-5563.

- (64) Xia, Y.; Kornfield, J. A.; Grubbs, R. H. *Macromolecules* **2009**, *42*, 3761-3766.
- (65) Fréchet, J. M. J.; Ito, H.; Willson, C. G. *Microcircuit Eng. 82 [Proc. Microcircuit Eng. Conf.]* **1982**, 260.
- (66) Fréchet, J. M. J.; Eichler, E.; Ito, H.; Willson, C. G. *Polymer* **1983**, *24*, 995.
- (67) Ito, H. *Adv. Polym. Sci.* **2005**, *172*, 37-245.
- (68) Grigorescu, A. E.; Hagen, C. W. *Nanotechnology* **2009**, *20*, 292001.
- (69) Sanders, D. P. *Chem. Rev.* **2010**, *110*, 321-360.
- (70) Prabhu, V. M.; Kang, S.; VanderHart, D. L.; Satija, S. K.; Lin, E. K.; Wu, W.-I. *Adv. Mater.* **2011**, *23*, 388-408.
- (71) Orski, S. V.; Fries, K. H.; Sontag, S. K.; Locklin, J. J. *Mater. Chem.* **2011**, *21*, 14135-14149.
- (72) International Technology Roadmap for Semiconductors. Overall Roadmap Technology Characteristics (ORTC) Tables, 2011;  
<http://www.itrs.net/reports.html>.
- (73) Bang, J.; Jeong, U.; Ryu, D. Y.; Russell, T. P.; Hawker, C. J. *Adv. Mater.* **2009**, *21*, 4769-4792.
- (74) Chai, J.; Wang, D.; Fan, X.; Buriak, J. M. *Nat. Nanotechnol.* **2007**, *2*, 500-506.
- (75) Bitá, I.; Yang, J. K. W.; Jung, Y. S.; Ross, C. A.; Thomas, E. L.; Berggren, K. K. *Science* **2008**, *321*, 939-943.
- (76) Ruiz, R.; Kang, H.; Detcheverry, F. A.; Dobisz, E.; Kercher, D. S.; Albrecht, T. R.; de Pablo, J. J.; Nealey, P. F. *Science* **2008**, *321*, 936-939.

- (77) Tang, C.; Lennon, E. M.; Fredrickson, G. H.; Kramer, E. J.; Hawker, C. J.  
*Science* **2008**, *322*, 429-432
- (78) Park, S.; Lee, D. H.; Xu, J.; Kim, B.; Hong, S. W.; Jeong, U.; Xu, T.; Russell, T.  
*P. Science* **2009**, *323*, 1030-1033.
- (79) Bates, C. M.; Seshimo, T.; Maher, M. J.; Durand, W. J.; Cushen, J. D.; Dean, L.  
M.; Blachut, G.; Ellison, C. J.; Willson, C. G. *Science* **2012**, *338*, 775-779.
- (80) Bosworth, J. K.; Black, C. T.; Ober, C. K. *ACS Nano* **2009**, *3*, 1761-1766.
- (81) Park, S.-M.; Liang, X.; Harteneck, B. D.; Pick, T. E.; Hiroshiba, N.; Wu, Y.;  
Helms, B. A.; Olynick, D. L. *ACS Nano* **2011**, *5*, 8523-8531.
- (82) Albert, J. N. L.; Bogart, T. D.; Lewis, R. L.; Beers, K. L.; Fasolka, M. J.;  
Hutchison, J. B.; Vogt, B. D.; Epps, T. H. *Nano Lett.* **2011**, *11*, 1351-1357.
- (83) Jung, H.; Hwang, D.; Kim, E.; Kim, B.-J.; Lee, W. B.; Poelma, J. E.; Kim, J.;  
Hawker, C. J.; Huh, J.; Ryu, D. Y.; Bang, J. *ACS Nano* **2011**, *5*, 6164-6173.
- (84) Tang, C.; Wu, W.; Smilgies, D.-M.; Matyjaszewski, K.; Kowalewski, T. *J. Am.*  
*Chem. Soc.* **2011**, *133*, 11802-11809.
- (85) Tully, D. C.; Trimble, A. R.; Fréchet, J. M. J. *Adv. Mater.* **2000**, *12*, 1118-1122.
- (86) Sheiko, S. S.; Sumerlin, B. S.; Matyjaszewski, K. *Prog. Polym. Sci.* **2008**, *33*,  
759-785.
- (87) Hosono, N.; Kajitani, T.; Fukushima, T.; Ito, K.; Sasaki, S.; Takata, M.; Aida, T.  
*Science* **2010**, *330*, 808-811.
- (88) Müllner, M.; Yuan, J.; Weiss, S.; Walther, A.; Förtsch, M.; Drechsler, M.;  
Müller, A. H. E. *J. Am. Chem. Soc.* **2010**, *132*, 16587-16592.

- (89) Li, Z.; Ma, J.; Lee, N. S.; Wooley, K. L. *J. Am. Chem. Soc.* **2011**, *133*, 1228-1231.
- (90) Johnson, J. A.; Lu, Y. Y.; Burts, A. O.; Lim, Y. H.; Finn, M. G.; Koberstein, J. T.; Turro, N. J.; Tirrell, D. A.; Grubbs, R. H. *J. Am. Chem. Soc.* **2011**, *133*, 559-566.
- (91) Voet, V. S. D.; Pick, T. E.; Park, S.-M.; Moritz, M.; Hammack, A. T.; Urban, J. J.; Ogletree, D. F.; Olynick, D. L.; Helms, B. A. *J. Am. Chem. Soc.* **2011**, *133*, 2812-2815.
- (92) Sutthasupa, S.; Shiotsuki, M.; Sanda, F. *Polym. J.* **2010**, *42*, 905-915.
- (93) Boyer, C.; Bulmus, V.; Davis, T. P.; Ladmiral, V.; Liu, J. Q.; Perrier, S. *Chem. Rev.* **2009**, *109*, 5402-5436.
- (94) Gonsalves, K. E.; Wang, M. X.; Lee, C. T.; Yueh, W.; Tapia-Tapia, M.; Batina, N.; Henderson, C. L. *J. Mater. Chem.* **2009**, *19*, 2797-2802.
- (95) Pfeifer, S.; Lutz, J.-F. *J. Am. Chem. Soc.* **2007**, *129*, 9542-9543.
- (96) Satoh, K.; Matsuda, M.; Nagai, K.; Kamigaito, M. *J. Am. Chem. Soc.* **2010**, *132*, 10003-10005.
- (97) Paik, M. Y.; Xu, Y.; Rastogi, A.; Tanaka, M.; Yi, Y.; Ober, C. K. *Nano Lett.* **2010**, *10*, 3873-3879.
- (98) Jeon, H.; Schmidt, R.; Barton, J. E.; Hwang, D. J.; Gamble, L. J.; Castner, D. G.; Grigoropoulos, C. P.; Healy, K. E. *J. Am. Chem. Soc.* **2011**, *133*, 6138-6141.
- (99) These depths were calculated from the full width at half-maximum of the F<sup>-</sup>/CH<sup>2-</sup> intensity ratio.

- (100) Lee, S. M.; Fréchet, J. M. J.; Willson, C. G. *Macromolecules* **1994**, *27*, 5154-5159.
- (101) Amir, R. J.; Zhong, S.; Pochan, D. J.; Hawker, C. J. *J. Am. Chem. Soc.* **2009**, *131*, 13949-13951.
- (102) Pitois, C.; Wiesmann, D.; Lindgren, M.; Hult, A. *Adv. Mater.* **2001**, *13*, 1483-1487.
- (103) Li, A.; Ma, J.; Sun, G.; Li, Z.; Cho, S.; Clark, C.; Wooley, K. L. *J. Polym. Sci., Part A: Polym. Chem.* **2012**, *50*, 1681-1688.
- (104) Verkhoturov, S. V.; Eller, M. J.; Rickman, R. D.; Della-Negra, S.; Schweikert, E. *A. J. Phys. Chem. C* **2009**, *114*, 5637-5644.
- (105) Li, Z.; Verkhoturov, S. V.; Locklear, J. E.; Schweikert, E. A. *Int. J. Mass spectrom.* **2008**, *269*, 112-117.
- (106) Chen, L.-J.; Seo, J. H.; Eller, M. J.; Verkhoturov, S. V.; Shah, S. S.; Revzin, A.; Schweikert, E. A. *Anal. Chem.* **2011**, *83*, 7173-7178.
- (107) Yu, M. L.; Lang, N. D. *Nucl. Instrum. Methods Phys. Res., Sect. B* **1986**, *14*, 403-413.
- (108) Lang, N. D.; Nørskov, J. K. *Phys. Scr.* **1983**, *T6*, 15-18.
- (109) Harton, S. E.; Stevie, F. A.; Ade, H. *J. Vac. Sci. Technol., A* **2006**, *24*, 362-368.
- (110) Herr, D. J. *J. Mater. Res.* **2011**, *26*, 122-139.
- (111) Jeong, S.-J.; Moon, H.-S.; Kim, B. H.; Kim, J. Y.; Yu, J.; Lee, S.; Lee, M. G.; Choi, H.; Kim, S. O. *ACS Nano* **2010**, *4*, 5181-5186.



- (112) Han, E.; Kang, H.; Liu, C.-C.; Nealey, P. F.; Gopalan, P. *Adv. Mater.* **2010**, *22*, 4325-4329.
- (113) Tavakkoli K. G., A.; Gotrik, K. W.; Hannon, A. F.; Alexander-Katz, A.; Ross, C. A.; Berggren, K. K. *Science* **2012**, *336*, 1294-1298.
- (114) Yang, J. K. W.; Jung, Y. S.; Chang, J.-B.; Mickiewicz, R. A.; Alexander Katz, A.; Ross, C. A.; Berggren, K. K. *Nat. Nanotechnol.* **2010**, *5*, 256-260.
- (115) Hong, S. W.; Huh, J.; Gu, X.; Lee, D. H.; Jo, W. H.; Park, S.; Xu, T.; Russell, T. P. *Proc. Natl. Acad. Sci. U.S.A.* **2012**, *109*, 1402-1406.
- (116) Stoykovich, M. P.; Müller, M.; Kim, S. O.; Solak, H. H.; Edwards, E. W.; de Pablo, J. J.; Nealey, P. F. *Science* **2005**, *308*, 1442-1446.
- (117) Xu, J.; Russell, T. P.; Ocko, B. M.; Checco, A. *Soft Matter* **2011**, *7*, 3915-3919.
- (118) Jeong, M. G.; van Hest, J. C. M.; Kim, K. T. *Chem. Commun.* **2012**, *48*, 3590-3592.
- (119) Avgeropoulos, A.; Rangou, S.; Krikorian, V.; Thomas, E. L. *Macromol. Symp.* **2008**, *267*, 16-20.
- (120) He, X.; Zhong, L.; Wu, X.; Cai, X.; Xie, M.; Lin, S.; Yan, D. *J. Polym. Sci., Part A: Polym. Chem.* **2012**, *50*, 2841-2853.
- (121) Rho, Y.; Kim, C.; Higashihara, T.; Jin, S.; Jung, J.; Shin, T. J.; Hirao, A.; Ree, M. *ACS Macro Lett.* **2013**, *2*, 849-855.
- (122) Ungar, G.; Tschierske, C.; Abetz, V.; Holyst, R.; Bates, M. A.; Liu, F.; Prehm, M.; Kieffer, R.; Zeng, X.; Walker, M.; Glettner, B.; Zywockinski, A. *Adv. Funct. Mater.* **2011**, *21*, 1296-1323.

- (123) Zhou, Y.; Huang, W.; Liu, J.; Zhu, X.; Yan, D. *Adv. Mater.* **2010**, *22*, 4567-4590.
- (124) Sveinbjörnsson, B. R.; Weitekamp, R. A.; Miyake, G. M.; Xia, Y.; Atwater, H. A.; Grubbs, R. H. *Proc. Natl. Acad. Sci. U.S.A.* **2012**, *109*, 14332-14336.
- (125) Gu, W.; Huh, J.; Hong, S. W.; Sveinbjörnsson, B. R.; Park, C.; Grubbs, R. H.; Russell, T. P. *ACS Nano* **2013**, *7*, 2551-2558.
- (126) Runge, M. B.; Dutta, S.; Bowden, N. B. *Macromolecules* **2006**, *39*, 498-508.
- (127) Sun, G.; Cho, S.; Clark, C.; Verkhoturov, S. V.; Eller, M. J.; Li, A.; Pavía-Jiménez, A.; Schweikert, E. A.; Thackeray, J. W.; Trefonas, P.; Wooley, K. L. *J. Am. Chem. Soc.* **2013**, *135*, 4203-4206.
- (128) Trefonas, P.; Thackeray, J. W.; Sun, G.; Cho, S.; Clark, C.; Verkhoturov, S. V.; Eller, M. J.; Li, A.; Pavia-Sanders, A.; Schweikert, E. A.; Wooley, K. L. *J. Micro/Nanolith.* **2013**, *12*, 043006.
- (129) Della-Negra, S.; Arianer, J.; Depauw, J.; Verkhoturov, S. V.; Schweikert, E. A. *Surf. Interface Anal.* **2011**, *43*, 66-69.
- (130) Chen, L.-J.; Shah, S. S.; Verkhoturov, S. V.; Revzin, A.; Schweikert, E. A. *Surf. Interface Anal.* **2011**, *43*, 555-558.
- (131) MacDonald, S. A.; Frechet, J. M. J.; Ito, H.; Grant Willson, C. *Microelectron. Eng.* **1985**, *3*, 277-278.
- (132) Thackeray, J. W. *Proc. SPIE* **2011**, 7972, 797204.
- (133) Chochos, C. L.; Ismailova, E.; Brochon, C.; Leclerc, N.; Tiron, R.; Sourd, C.; Bandelier, P.; Foucher, J.; Ridaoui, H.; Dirani, A.; Soppera, O.; Perret, D.; Brault, C.; Serra, C. A.; Hadziioannou, G. *Adv. Mater.* **2009**, *21*, 1121-1125.

- (134) Wieberger, F.; Neuber, C.; Ober, C. K.; Schmidt, H.-W. *Adv. Mater.* **2012**, *24*, 5939-5944.
- (135) Yoshida, M.; Fréchet, J. M. J. *Polymer* **1994**, *35*, 5-13.
- (136) Niu, Q. J.; Fréchet, J. M. J. *Angew. Chem. Int. Ed.* **1998**, *37*, 667-670.
- (137) Tully, D. C.; Wilder, K.; Fréchet, J. M. J.; Trimble, A. R.; Quate, C. F. *Adv. Mater.* **1999**, *11*, 314-318.
- (138) Frechet, J. M. J.; Tessier, T. G.; Willson, C. G.; Ito, H. *Macromolecules* **1985**, *18*, 317-321.
- (139) Frechet, J. M. J.; Matuszczak, S.; Reck, B.; Stover, H. D. H.; Willson, C. G. *Macromolecules* **1991**, *24*, 1746-1754.
- (140) Matuszczak, S.; Cameron, J. F.; Frechet, J. M. J.; Wilson, C. G. *J. Mater. Chem.* **1991**, *1*, 1045-1050.
- (141) Fahey, J. T.; Frechet, J. M. J.; Shacham-Diamand, Y. *J. Mater. Chem.* **1994**, *4*, 1533-1538.
- (142) Lee, S. M.; Frechet, J. M. J. *Chem. Mater.* **1994**, *6*, 1838-1841.
- (143) Cameron, J. F.; Willson, C. G.; Fréchet, J. M. J. *J. Am. Chem. Soc.* **1996**, *118*, 12925-12937.
- (144) Lin, Q.; Steinhäusler, T.; Simpson, L.; Wilder, M.; Medeiros, D. R.; Willson, C. G.; Havard, J.; Fréchet, J. M. J. *Chem. Mater.* **1997**, *9*, 1725-1730.
- (145) Havard, J. M.; Shim, S.-Y.; Fréchet, J. M. J.; Lin, Q.; Medeiros, D. R.; Willson, C. G.; Byers, J. D. *Chem. Mater.* **1999**, *11*, 719-725.
- (146) Rolandi, M.; Suez, I.; Dai, H.; Fréchet, J. M. J. *Nano Lett.* **2004**, *4*, 889-893.

- (147) Frechet, J. M. J. *Pure Appl. Chem.* **1992**, *64*, 1239-1248.
- (148) Ma, J.; Cheng, C.; Sun, G.; Wooley, K. L. *J. Polym. Sci., Part A: Polym. Chem.* **2008**, *46*, 3488-3498.
- (149) Cho, S.; Yang, F.; Sun, G.; Eller, M. J.; Clark, C.; Schweikert, E. A.; Thackeray, J. W.; Trefonas, P.; Wooley, K. L. *Macromol. Rapid Commun.* **2014**, *35*, 437-441.
- (150) Gu, W.; Xu, J.; Kim, J.-K.; Hong, S. W.; Wei, X.; Yang, X.; Lee, K. Y.; Kuo, D. S.; Xiao, S.; Russell, T. P. *Adv. Mater.* **2013**, *25*, 3677-3682.
- (151) Mansky, P.; Liu, Y.; Huang, E.; Russell, T. P.; Hawker, C. *Science* **1997**, *275*, 1458-1460.
- (152) Uetani, Y.; Fujishima, H.; Araki, K.; Endo, K.; Takemoto, I. *Proc. SPIE* **1999**, *3678*, 510-517.
- (153) The line width was measured at 90% of the line height and deducted 10 nm (2\*AFM tip diameter).

## APPENDIX A

### QUANTITATIVE ANALYSIS OF BRUSH FILMS BY X-RAY PHOTOELECTRON MICROSCOPY

The relative elemental ratios of ideally vertical aligned structure of brush films as comparison data for x-ray photoelectron microscopy quantification analysis were calculated in two different methods. In the simple method, the value was calculated based on the information depth (ID) of 10 nm which is known as the maximum depth from which 95% of all photoelectrons are scattered by the time they reach the surface for Al K $\alpha$  radiation. However, each photoelectron has different inelastic mean free path (IMFP) depending on their kinetic energy. In A.2., the differential IMFPs were applied to the calculation of the relative elemental ratios of ideally vertical aligned structure of brush films. By the calculation described below, there is no significant difference of the relative fluorine ratio from the two methods. Therefore, the simple method was used in Chapter II–IV for simplification.

#### **A.1. Simple Method**

The relative elemental ratios of ideally vertical aligned structure of brush films described in Chapter II–IV were calculated with information depth (ID) of 10 nm. Here, the calculation procedure is described with brush I and II as examples.

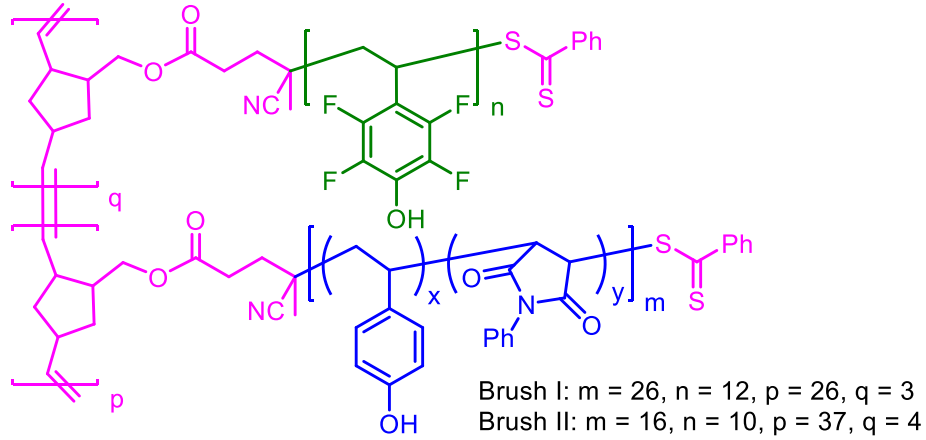


**Figure A.1.** Brush polymers for negative-tone resist, P(NB-g-PTFpHS)-*b*-P(NB-g-(pHS-co-PhMI)).

First, the total numbers of elements in 10 nm from top brush film are calculated. If the brushes are vertically aligned on substrates the fluoropolymer block is located on top. Accounting the length of single norbornene backbone ( $l_{NB}$ ) as 0.598 nm, the backbone length of P(NB-g-PTFpHS) blocks are smaller than ID and all block units are counted within 10 nm ID. For P(NB-g-(pHS-co-PhMI)), number of backbone repeat unit counted within the information depth is

$$RU = \frac{ID - q \times l_{NB}}{l_{NB}} \quad (1)$$

The total numbers of elements,  $F_{tot}$ ,  $O_{tot}$ ,  $C_{tot}$ , in 10 nm ID are:

$$F_{tot} = 4 \times n \times q \quad (2)$$

$$O_{tot} = (2 + n) \times q + (2 + m + 2 \times y) \times RU \quad (3)$$

$$C_{tot} = (21 + 8 \times n) \times q + (21 + 8 \times x + 10 \times y) \times RU \quad (4)$$

The relative quantity of elements in 10 nm ID are:

$$F_R = \frac{F_{tot}}{F_{tot} + O_{tot} + C_{tot}} \times 100 (\%) \quad (5)$$

$$O_R = \frac{O_{tot}}{F_{tot}+O_{tot}+C_{tot}} \times 100 (\%) \quad (6)$$

$$C_R = \frac{C_{tot}}{F_{tot}+O_{tot}+C_{tot}} \times 100 (\%) \quad (7)$$

The resulting value of total numbers and relative quantities of elements are in Table A.1.

**Table A.1.** Total numbers and relative quantity of elements in 10 nm information depth of brush polymer films with ideally vertical aligned structure, expected in XPS measurement with Al K $\alpha$  radiation.

	$C_{tot}$	$O_{tot}$	$F_{tot}$	$C_R$	$O_R$	$F_R$
Brush I	3921	616	144	83.8	13.2	3.1
Brush II	2549	386	160	82.4	12.5	5.2

## A.2. Considering Electron Inelastic Mean Free Path

The relative elemental ratio of ideally vertical aligned structure is described with the consideration of differential IMFPs of photoelectrons of each element. The IMFP of electrons are estimated for organic materials involving the quantitative structure-property relationship by Cumpson method.\*

The zero-order connectivity indices  ${}^0\chi^{(v)}$  is

$${}^0\chi^{(v)} = \sum_{\text{non-H atoms}} \left( \frac{1}{\sqrt{\delta^{(v)}}} \right) \quad (8)$$

${}^0\chi^{(v)}$  for NB-g-PTHpHS is

---

\*Cumpson, P. J. *Surf. Interface Anal.* **2001**, 32, 23-34.

$${}^0\chi^{(v)}_a = \frac{1}{\sqrt{2}} + \frac{1}{\sqrt{3}} + \frac{6}{\sqrt{4}} + \frac{1}{\sqrt{5}} + \frac{4}{\sqrt{7}} = 6.2435 \text{ \AA} \quad (9)$$

${}^0\chi^{(v)}$  for NB-*g*-(*p*HS-*co*-PhMI) is

$${}^0\chi^{(v)}_b \chi^{0,(v)} = \frac{1}{\sqrt{2}} + \frac{12}{\sqrt{3}} + \frac{5}{\sqrt{4}} + \frac{2}{\sqrt{5}} + \frac{2}{\sqrt{7}} = 11.8462 \text{ \AA} \quad (10)$$

The IMFP for electrons is

$$\lambda_i/\text{\AA} = \left[ \frac{31.17(\chi^v) + 4.207N_{\text{ring}}}{N_{\text{non-H}}} + 11.04 \right] \times (E/\text{keV})^{0.79} \quad (11)$$

Where  $E$  is kinetic energy of electron. In vertical aligned structure of brush polymer, photoelectron of fluorine comes from NB-*g*-PTH*p*HS. Therefore, the IMFP for F 1s photoelectron is calculated with  ${}^0\chi^{(v)}_a = 6.2435$  as below:

$$\lambda_i^{\text{F}} = \left( \frac{31.17 \times 6.2435 + 4.207 \times 1}{13} + 11.04 \right) \times 0.80^{0.79} = 22.08 \text{ \AA} \quad (12)$$

where the kinetic energy is XPS measurement with X-ray source of Al K $\alpha$ . On the other hand, photoelectron of C 1s and O 1s come from both NB-*g*-PTH*p*HS and P(NB-*g*-(*p*HS-*co*-PhMI)). The IMFP for carbon and oxygen photoelectron are calculated with  ${}^0\chi^{(v)} = {}^0\chi^{(v)}_a + {}^0\chi^{(v)}_b$  as below:

$$\lambda_i^{\text{O}} = \left( \frac{31.17 \times (6.2435 + 11.8462) + 4.207 \times 3}{35} + 11.04 \right) \times 0.955^{0.79} = 26.53 \text{ \AA} \quad (13)$$

$$\lambda_i^{\text{C}} = \left( \frac{31.17 \times (6.2435 + 11.8462) + 4.207 \times 3}{35} + 11.04 \right) \times 1.203^{0.79} = 31.84 \text{ \AA} \quad (14)$$

The ID with straight-line approximation from which a specific percentage  $P$  of the detected signal is as follow:\*

---

\* Jablonski, A.; Powell, C. J. *J. Vac. Sci. Technol. A* **2009**, 27, 253-261.



$$ID_{SLA} = \lambda_i \cos \alpha \ln \left[ \frac{1}{1-(P/100)} \right] \quad (15)$$

where  $\alpha$  is the electron emission angle. The ID of fluorine, oxygen, and carbon photoelectrons with  $P = 95$  % and  $\alpha = 0^\circ$  are 6.615, 7.947, and 8.241 nm, respectively. Considering ID of each element, total numbers and relative quantities of elements are calculated in equation (1)–(7) (Table A.2). The relative quantities of elements considering IMFP of each photoelectron are corresponding to those from simple method.

**Table A.2.** Total numbers and relative quantity of elements in their calculated information depth of brush polymer films with ideally vertical aligned structure, expected in XPS measurement.

	$C_{\text{tot}}$	$O_{\text{tot}}$	$F_{\text{tot}}$	$C_{\text{R}}$	$O_{\text{R}}$	$F_{\text{R}}$
Brush I	3651	464	144	85.7	10.9	3.4
Brush II	2375	289	160	84.1	10.3	5.7

## APPENDIX B

### HYBRID CORE/SHELL/SATELLITE STRUCTURES FOR PLASMON ENHANCED LUMINESCENCE\*

Recently, fluorescent nanoparticles, mainly semiconducting quantum dots (QDs), have attracted attention for a various range of purposes and applications, such as displays, photovoltaics, bioimaging and sensing. With the inherent luminescent properties, light emitting diodes with QDs show promises in the development of next generation displays, because QDs demonstrate high photoluminescence quantum yields, narrow spectral emission band widths, broad absorption, compatibility with solution processing, controllable band gap through size tuning, and good photostability. The intensity of fluorescence of QDs can be enhanced by coupling with the metallic nanoparticles, which is referred to as metal enhanced fluorescence (MEF). The enhancement effect is related with the size, shape, composition, and organization of metal nanoparticles (MNPs). In addition to the fluorescence enhancement, the interaction of fluorophores with MNPs results in increased photostability and decreased lifetime due to increased rates of system radiative decay.

Meanwhile, core/shell nanoparticles are attracting more and more attention with their distinctive and advanced properties. Core/shell nanoparticles are highly functional

---

\*In collaboration with Yerok Park and Dong Hee Son in the Department of Chemistry at Texas A&M University.

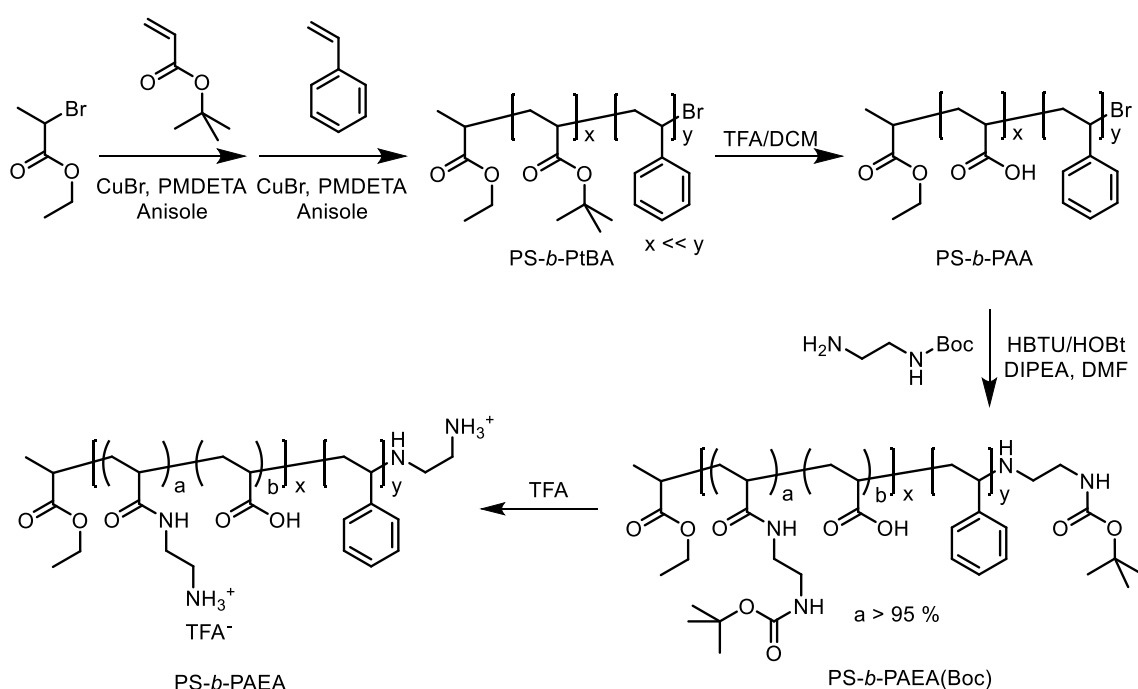
materials with modified properties from the core materials themselves in the points of reactivity, thermal or chemical stability, dispersibility, *etc.* With their unique optical properties entailing localized surface plasmon resonance noble metals such as gold and silver have attracted attention. Among many combinations of core/shell materials, metal/organic core/shell nanoparticles are made of metal core with a shell of polymers or high density organic materials. The coating of organic materials on metal core gives many advantages, for example, the increase of oxidation stability of the metal core, enhanced biocompatibility for bioapplications with the enriched surface functional group for bioconjugation purposes, and enhancement of dispersion in suspension by the electrostatic or steric repulsion forces depending on the shell media, *etc.*

Recently, the preparations of core/shell Au nanoparticles via the block copolymer self-assembly approach were reported by Taton and Chen research groups, separately. Here, amphiphilic block copolymers having hydrophilic and hydrophobic blocks on a linear polymer chain act as surfactant to encapsulate Au nanoparticles with the hydrophobic block inside during solvent exchange or heating/cooling process. The hydrophilic block is exposed to the surface with functional groups which can be modified variously. For example, hydrophilic block having cationic groups can be used to incorporate any nanoparticles having anionic surfaces by electrostatic interaction. The combination of the nanoparticle encapsulation methods and the concept of MEF is promising to fabricate the new hybrid CSSs consisting of noble metals as a core, amphiphilic block copolymers as a shell, and fluorescent nanoparticles such as QDs as satellites. First, MNPs with various range of sizes can be used, which gives a benefit to

match plasmonic wavelength compatible to the absorption wavelength of fluorescent nanoparticles. Second, the shell thickness, which means the distance between MNP and QDs, can be adjustable by varying the constituent blocks. Third, the functionality of the shell can be easily tuned by changing the block copolymer composition, which allows fluorescent nanoparticles to easily approach and attach onto the shell surface without further surface treatments. Fourth, the formed nanostructures are stable in both organic and aqueous solutions, which is beneficial for future applications. For example, once the CSSs have been prepared, they can reduce the cost for device (such as LED) fabrication by using soft lithography, or even roll-to-roll, instead of using expensive patterning processes (such as photolithography) or vacuum required-processes.

To incorporate the negatively-charged QDs on the surface of core/shell structures by electrostatic interaction, the hydrophilic blocks of the amphiphilic block copolymers should have positive charge. Also, the enhancement of fluorescence by plasmonic coupling is known to rely on the distance, corresponding to the shell thickness in the core/shell structures, between metal cores and QDs. With the competition of PL enhancement and quenching, optimum distance is required for the best enhancement. The dimension of the shell can be controlled by the block size of the amphiphilic block copolymers. Therefore, the series of block copolymers having hydrophobic blocks and cationic hydrophilic blocks are prepared *via* controlled radical polymerization and modification of anionic carboxyl groups to cationic amine groups (Scheme B.1). First, poly(*t*-butylacrylic acid)-*block*-polystyrene (PtBA-*b*-PS) is synthesized *via* sequential atom transfer radical polymerization (ATRP) of *t*-butyl acrylate (*t*BA) and styrene. Then,

the *t*-butyl ester protecting groups are removed to produce anionic poly(acrylic acid)-*block*-polystyrene (PAA-*b*-PS). The modification of anionic blocks to cationic blocks is performed by peptide coupling reaction between carboxyl groups of PAA and amine groups of *t*-butyl 2-aminoethylcarbamate, followed by removal of *t*-butyloxycarbonyl groups to produce cationic amphiphilic poly(acrylamidoethylamine)-*block*-polystyrene (PAEA-*b*-PS).



**Scheme B.1.** Synthesis of PAEA-*b*-PS amphiphilic block copolymers.

Ag nanoparticles, block copolymers, and QDs are assembled to CSSs by the encapsulation of Ag nanoparticles with amphiphilic block copolymers, followed by attachment of QDs on the cationic surface of polymeric shells (Scheme B.2). First, the encapsulation of Ag NPs with block copolymers can be processed in solvent exchange



As characterized by TEM, Ag nanoparticles are well encapsulated by cationic amphiphilic block copolymers (Figure B.1). To limit the number of micelles that contained multiple particles, a substantial excess of polymer compared to the Ag nanoparticles is used in the encapsulation process. As a result, successive centrifugations are required to get pure Ag/polymer core/shell structures (Figure B.1b) from free polymeric micelles (Figure B.1a).

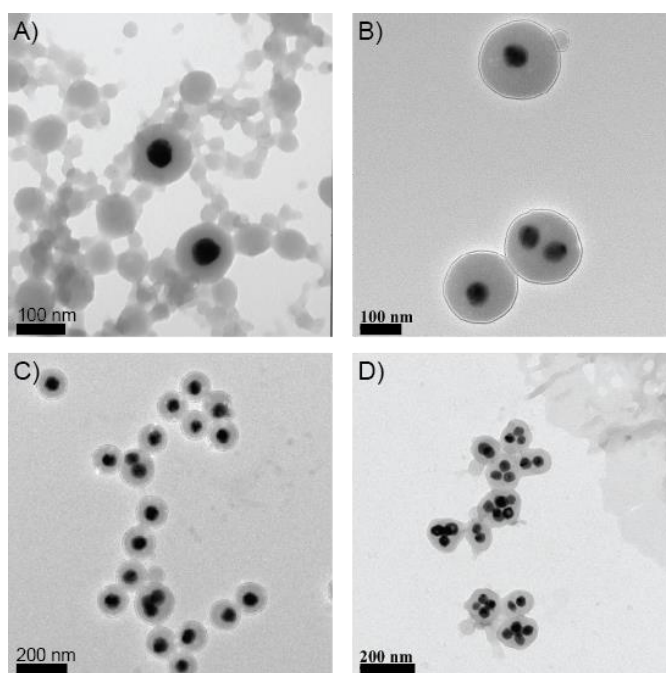


**Figure B.1.** TEM images of Ag nanoparticles encapsulated within PAEA-*b*-PS micelles (a) before and (b–d) after separation of free polymeric micelles by centrifugation. 50 nm Ag nanoparticles are encapsulated within (a, b) PAEA<sub>16</sub>-*b*-PS<sub>260</sub>, shell thickness of 40–70 nm and (c) PAEA<sub>16</sub>-*b*-PS<sub>140</sub>, shell thickness of 25–30 nm. (d) Multiple Ag nanoparticles are encapsulated within polymeric micelles.

With the use different block size of amphiphilic block copolymers, the shell thickness of the core/shell structures is controlled. The longer block size of amphiphilic block copolymers is used, the thicker shell in the core/shell structures is formed. While the shell thickness of Ag nanoparticles encapsulated by PAEA<sub>16</sub>-*b*-PS<sub>260</sub> is bigger than 50 nm, that of the Ag nanoparticles encapsulated by PAEA<sub>16</sub>-*b*-PS<sub>140</sub> is smaller than 30 nm. However, the shell thickness depends not only on the polymer block size. The shell thickness can also be controlled by varying the ratio of MNP vs. polymer concentration in the solution. In general, the higher concentration of polymer results in thicker shell in the core/shell thickness. However, the use of too low concentration of polymers leads to multiple metal nanoparticles in a micelle (Figure B.1d).

The encapsulated nanoparticles are stable in aqueous solution for several months, which is explained by the electrostatic repulsion from the positively-charged amine functional groups. From the zeta-potential analysis, the surface charge of micelles is over 30 mV at pH 7, which explains the stability of the core/shell nanostructures in solution.

After the core/shell nanostructures are prepared, QDs are attached onto the cationic surface of the nanostructures by addition of citrate-stabilized Mn-doped CdS (Figure B.2a). As shown in Figure B.2b and c, the negatively-charged QDs interact well with the positively-charged polymeric surface in the solution of pH 8 to 9 to produce Ag@PAEA-*b*-PS@CdS CSSs. However, the Ag@PAEA-*b*-PS@CdS CSS structure is not stable in aqueous solution and tends to aggregate, which might be due to inter-particle interaction by insufficient surface passivation. Also, the enhanced fluorescence was not observed in this CSS solution. The aggregate might lead to the quenching of fluorescence.



More studies are required for the optimization of shell thickness for maximum fluorescent enhancement by using different size of Ag nanoparticles and amphiphilic block copolymers and QDs density in each CSS structure for stability and enhanced fluorescence properties.

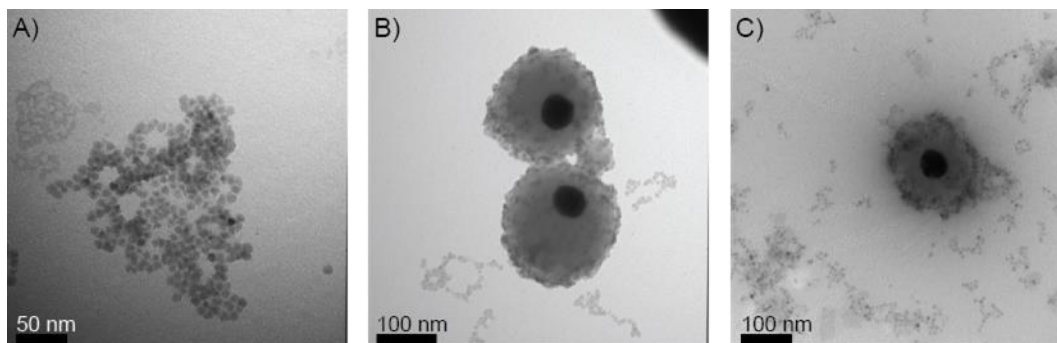


**Figure B.2.** TEM images of (a) QDs, Mn doped CdS/ZnS core/shell nanocrystals and Ag@PAEA-b-PS@QDs core/shell/satellite nanostructures assembled in (b) pH 8 and (c) pH 9.

The amphiphilic polymers play a role as a shell to give stability and dispersibility of the hybrid nanostructures and as a spacer between plasmonic metal nanoparticles and fluorescent nanoparticles to prevent fluorescence from quenching. Instead, control of the space distance can provide switching properties of fluorescence. Responsive polymers perform reversible or irreversible changes in chemical structures or physical properties to external stimuli such as temperature, ionic strength, pH, light irradiation, specific analytes, or external additives. For example, thermo-responsive polymers change their solubility in aqueous media by external temperature change; that is, they swell below low critical solution temperature (LCST) but aggregate above LCST. pH-responsive polymers change

their solubility at the boundary of  $pK_{as}$  of them. Therefore, use of responsive polymers as shell materials can provide sensing properties of external stimuli to the nanostructures by detecting fluorescence variation from volume change of the polymers.

Organic fluorescent dyes can replace QDs as luminescent materials. Small molecular organic fluorophores have several limitations such as low structural stability, poor water solubility, and difficulty of further functionalization. The incorporation of organic fluorophores into responsive polymer matrix can solve the intrinsic problems of small molecule-based chemosensors. Also, multiple fluorescent dyes having different excitation and emission wavelength can be used to build ratiometric sensing based multiple-emission profiles. It is known that when two chromophores are close together, the energy of the donor chromophore in its excited state transfers to the acceptor chromophore through non-radiative dipole-dipole coupling. The energy transfer efficiency is inversely proportional to the sixth power of the distance between donor and acceptor, making Foster resonance energy transfer (FRET) sensitive to small distances. The incorporation of multiple organic fluorophores into stimuli-responsive polymers can provide ratiometric multiple emission profile by the variation of external stimuli. The volume change in responsive polymer matrix controls the distance between donor and acceptor fluorophores, which results in alteration of emission intensity between two fluorophores. Here, unlimited numbers of combination among various responsive polymers and spatial location and distribution of fluorophores in the polymer matrix are prospective to broaden the area of sensing materials.

In conclusion, hierarchical structures of metal nanoparticle/amphiphilic block copolymers/QDs for plasmon enhanced luminescence were prepared with the control of polymeric shell thickness. However, the enhanced luminescent property was not observed due to the aggregation of the resulting hierarchical structure, which prevents its completion for publication. The control of the density of attached quantum dots and polymer surface charge could avoid the aggregation leading the expected enhanced fluorescence. In addition, this concept of hierarchical structures can expand to the preparation of sensing materials by the use of stimuli responsive polymers for polymeric shells or organic fluorescent dyes as alternatives for QDs.